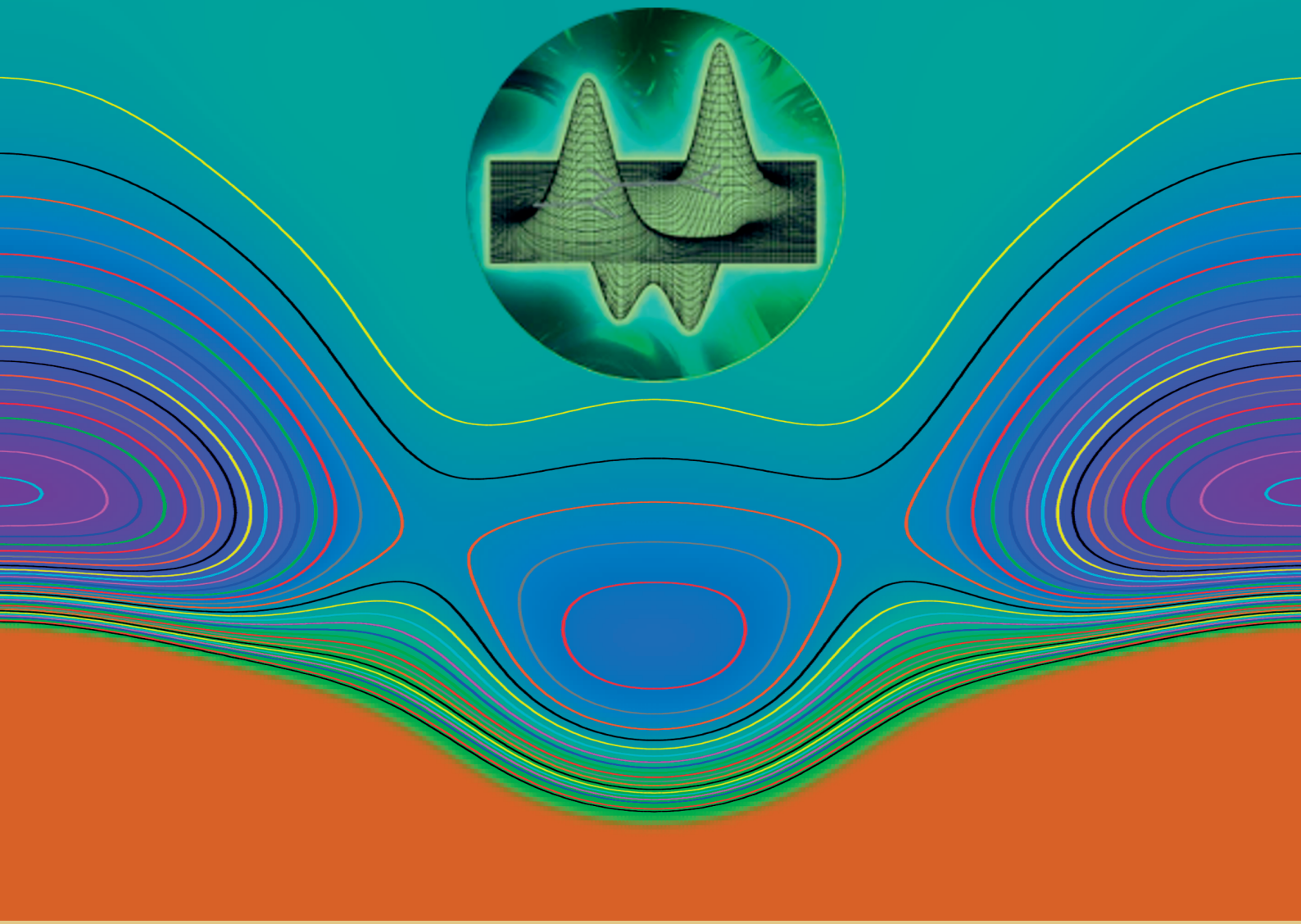

Jing Li

THEORETICAL STUDIES ON THE LOW-LYING ELECTRONIC STATES OF N_2O: FROM STRUCTURAL ASPECTS TO REACTION DYNAMICS

Ph.D. thesis in Chemistry, Theoretical Chemistry, under the supervision of Professor A. J. C. Varandas and presented to the Departamento de Química of Universidade de Coimbra

July, 2014

· U C ·

Universidade de Coimbra

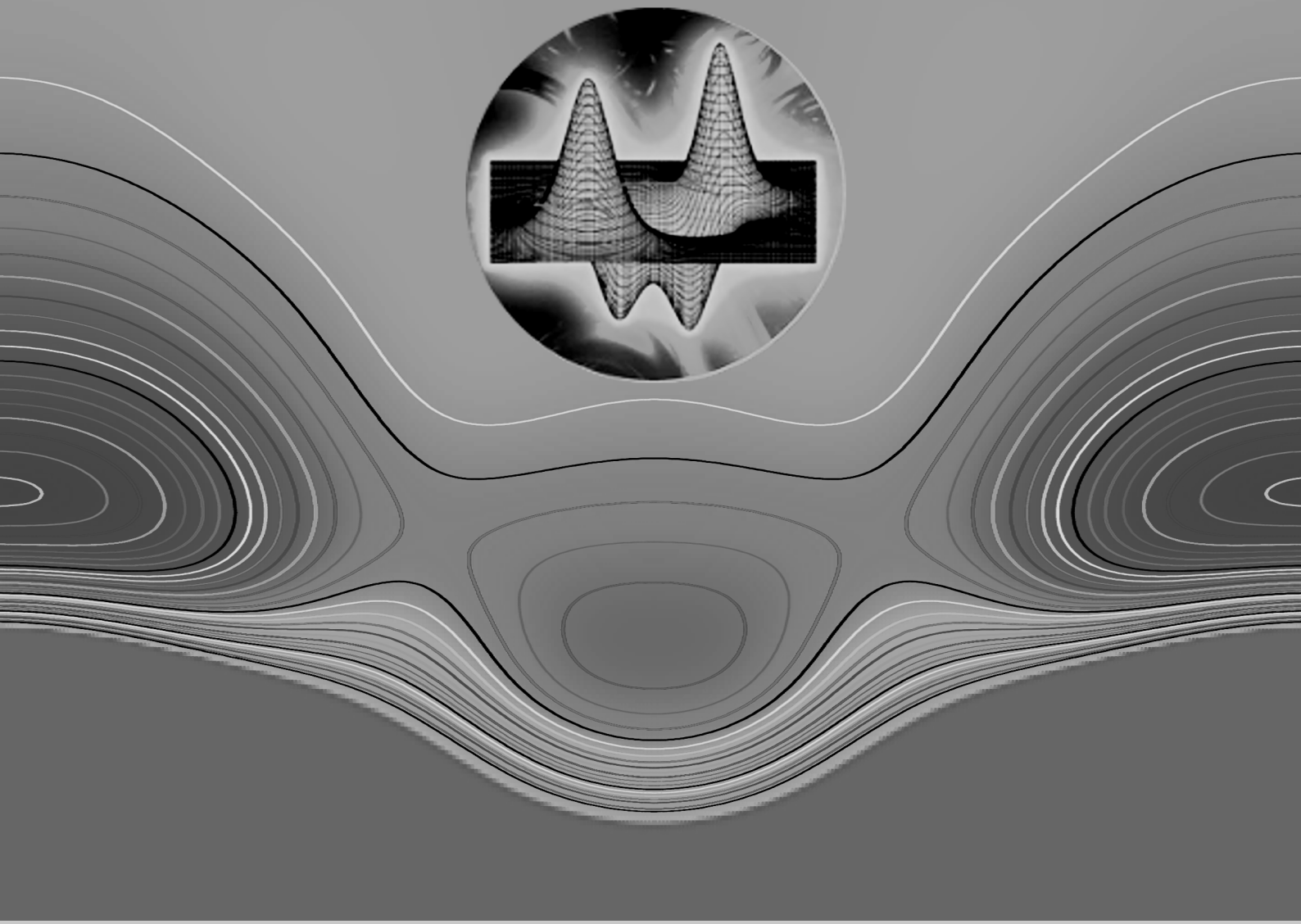

Jing Li

THEORETICAL STUDIES ON THE LOW-LYING ELECTRONIC STATES OF N_2O: FROM STRUCTURAL ASPECTS TO REACTION DYNAMICS

Ph.D. thesis in Chemistry, Theoretical Chemistry, under the supervision of Professor A. J. C. Varandas and presented to the Departamento de Química of Universidade de Coimbra

July, 2014

· U C ·

Universidade de Coimbra

Dedicated to my family

Abstract

A theoretical study on the N_2O molecular system is presented in this Ph.D. thesis: starting from the construction of a global potential energy surface for its ground electronic state, to dynamical studies of collisions taking place on it. The double many-body expansion (DMBE) method is employed in the construction of such potential function. The topology of the new surface is characterized in detail. A comparison between the properties of the stationary points obtained here with those reported in the literature is given, new structures are also characterized. The $N(^2D) + NO(X\,^2\Pi)$ atmospheric relevance reaction is then studied using quasi-classical trajectories method and the novel DMBE PES for the ground state of N_2O. Extensive comparisons with previous experimental and theoretical predictions have also been performed, with the results showing a higher reactivity than others available in the literature. An improved agreement with the experimental results has therefore been obtained, even though there are large experimental uncertainties. The increasing interest in this system led us to also study the first singlet excited state of nitrous oxide, which would be also required for studying fully the dynamics and kinetics of $N(^2D) + NO(X\,^2\Pi)$ reaction. Exploratory trajectories have also been run on this DMBE form with the quasiclassical trajectory method, with the thermal rate constant so determined at room temperature significantly enhancing agreement with the experimental data.

Contents

Acronyms

AO	Atomic orbitals
AVXZ	Augmented correlation consistent basis sets
BO	Born-Oppenheimer
BSSE	Basis set superposition error
CAS	Complete Active Space
CASPT2	Complete Active Space with Second-order Perturbation Theory
CASSCF	Complete Active Space Self Consistent Field
CCSD	Coupled-Cluster with Single and Double excitations
CCSD(T)	Coupled-Cluster with Single and Double and Perturbative Triple excitations
CI	Configuration Interaction or Conical Intersection
CS	Correlation Scaling
D2	Two-Electron Contribution to the Darwin term
DC	Dynamical Correlation
DIM	Diatomics-in-Molecules
DMBE	Double Many-Body Expansion
EHF	Extended Hartree Fock
EHFACE2U	EHF Approximate Correlation Energy including the United-atom limit
ES	Energy Switching
FCI	Full Configuration Interaction
GTO	Gaussian Type Orbital
HF	Hartree Fock
LEPS	London-Eyring-Polanyi-Sato

MBE	Many-Body Expansion
MCSCF	Multi Configuration Self Consistent Field
MGB	Momentum Gaussian Binning
MRCI	Multi-Reference Configuration Interaction
MRCISD	MRCI with singles and doubles excitations
MRCI(Q)	Multi-Reference Configuration Interaction with Davidson correction
PES	Potential Energy Surface
QCT	Quasiclassical Trajectory
QCT-IEQMT	QCT-Internal Energy Quantum Mechanical Threshold
QCT-IVEQMT	QCT-Intermediate Vibrational Energy Quantum Mechanical Threshold
QCT-NVEQMT	QCT-Rotational and Vibrational Energy Quantum Mechanical Threshold
QCT-QMT	QCT-Quantum Mechanical Threshold
QCT-VEQMT	QCT-Vibrational Energy Quantum Mechanical Threshold
RMSD	Root mean square deviation
RRKM	Rice–Ramsperger–Kassel–Marcus
SCF	Self Consistent Field
STO	Slater Type Orbital
TDQD	Time-Dependent Quantum Dynamics
TIDQ	Time-Independent Quantum Dynamics
TS	Transition State
USTE	Uniform Singlet- and Triplet-pair Extrapolation
VQZ	Correlation consistent polarized Valence Quadruple Zeta
ZPE	Zero-Point Energy

Introduction

Nitrous oxide is extremely important in atmospheric chemistry. It gives rise to NO (nitric oxide) on reaction with oxygen atoms, and this NO in turn reacts with ozone. As a result, it is the main naturally occurring regulator of stratospheric ozone. It is also a major greenhouse gas and air pollutant. Considered over a 100-year period, it has 298 times more impact per unit mass (global warming potential) than carbon dioxide. The emission of N_2O is currently the single most important ozone-depleting process and is expected to remain the largest throughout the 21st century[1], having significant potential in contributing to the control of global warming. Nitrous oxide, N_2O has been an important subject for a number of scientific fields such as life science[2], earth science[3], atmospheric science[4], and fuel industry[5]. It is also subject of theoretical[6–11] and experimental studies[12–19]

Specifically, the reaction of $N(^2D)$ with NO is a good prototype in collisional dynamics. There are several energetically accessible processes for the $N(^2D) + NO$ collisional process at room temperature:

$$\begin{aligned} N_a(^2D) + N_bO\,(X\,^2\Pi) &\rightarrow O(^3P) + N_2\,(X\,^1\Sigma_g^+) && (1)\\ &\rightarrow O(^1D) + N_2\,(X\,^1\Sigma_g^+) && (2)\\ &\rightarrow O(^1S) + N_2\,(X\,^1\Sigma_g^+) && (3)\\ &\rightarrow N_a(\,^2D) + N_bO\,(X\,^2\Pi) && (4)\\ &\rightarrow N_b(\,^2D) + N_aO\,(X\,^2\Pi) && (5) \end{aligned}$$

where the subscripts a and b label the two nitrogen atoms. Processes (1), (2) and (3) lead to formation of atomic oxygen in the fundamental or excited states, with the N_2 fragment left in its ground electronic state. Reactions (4) and (5) represent instead inelastic/elastic

processes, and the exchange reaction of atomic nitrogen, respectively. Reaction (2) is important in atmospheric processes and often used as a source of highly reactive oxygen atoms in the first excited state[20]. Correlating with products for reaction (2), there are 5 PESs which adiabatically correlate with reactants in C_s symmetry[6,21]: $1^1A'$, $2^1A'$, $3^1A'$, $1^1A''$ and $2^1A''$. However, theoretical information about all the regions of PES for those states are nonexistent, which would be necessary in a first approximation to the dynamics and kinetics studies of reaction (2). Only a few experimental kinetic studies are available dealing with the thermal rate constant for the total removal of N(^2D) by NO at 300 K[22–27].

It is somewhat unfortunate that such gas-phase chemical reactions of nitrous oxide have not been investigated with thoroughness. However, from both theoretical and experimental point of view, is very complicated to deal with such a processes, mainly due to the overwhelming physical complexity of the systems involved, a complementary description can be achieved by studying, using electronic structure calculation, of elementary gas-phase reaction analogous to those present in the real processes. During the past 20 years, as a result of significant advances in *ab initio* structure theory, an appreciable level of understanding of the properties of theses species and their spectroscopy and electronic structure, as well as their reactions and kinetics, has become available or more generally the features of their potential energy surfaces (PESs). Thus, the modelling of accurate global potential energy surfaces of nitrous oxide systems, combined with nuclear dynamics studies, may enhance the understanding of the gas-phase nitrogen-oxygen chemistry and support further investigations aiming at the improvement of the nitrogen fixation industrial mechanisms and ozone-depleting process.

Within the Born-Oppenheimer framework[28], the PES of a molecule is a function of the relative positions of the nuclei. It is considered as the most fundamental concept in all of structural chemistry and a focal point in chemical reaction dynamics, to elucidate the properties of the transition state, the point on the PES where bonds are broken and reformed. An analytical representation of the PES is achieved using different formalisms, such as the double many-body expansion (DMBE) method[29–31]. The latter consist of expanding the potential energy function of a given molecular system in terms of the

potential energies of its fragments. Information about a PES can be obtained both from the analysis of experimental data and from *ab initio* calculations. At present, robust theoretical frameworks and computational resources make possible to extensively explore the configuration space with the aim of constructing accurate and global *ab initio*-based PESs.

The aim of the present doctoral thesis was first to construct the DMBE PESs for the N_2O ground state and singlet excited state, to study molecular system's structure, energetics, and spectroscopy. The obtained PESs are also used for exploratory quasi-classical trajectory calculations of the thermal rate constants and cross sections of gas-phase reactions. The present PESs for N_2O can be employed as building-blocks of DMBE PESs of larger molecular systems, such as N_3O and N_2O_2, which contain the mentioned triatoms.

This thesis is organized as follows: Part I concerns with the theoretical background, presenting the concept of PES in Chapter 1, and giving a survey of the *ab initio* methods and the formalisms used to construct analytical representations of PES in Chapter 2, while dealing with methods here employed to study dynamics properties using the obtained PESs in Chapter 3. Part II refers to publications, with a global accurate DMBE potential energy surfaces for ground state N_2O presented[32]. Subsequently, the DMBE-PES for ground state N_2O is tested by computing spectroscopic properties and running dynamics calculations for reaction $N(^2D) + NO(X\,^2\Pi) \rightarrow O(^1D) + N_2(X\,^1\Sigma_g^+)$ [33]. Furthermore, we report DMBE potential energy surfaces for $2^1A'$ of N_2O, which is obtained from a least-squares fit to MRCI(Q)/VQZ energies which are semiempirically corrected by the DMBE scaled external correlation (DMBE-SEC) method. Quasiclassical trajectory studies have been carried out on the novel PESs. Finally, the main achievements are summarized and further possible applications are outlined in Part III.

Bibliography

[1] A. R. Ravishankara, J. S. Daniel, and R. W. Portmann, Science **326**, 123 (2009).

[2] L. G. Remsen, M. A. Pagel, C. I. McCormick, S. A. Fiamengo, G. Sexton, and E. A. Neuwelt, Anesth. Analg. (N.Y.) **88**, 559 (1999).

[3] J. Alm, S. Saarnio, H. Nykanen, J. Silvola, and P. J. Martikainen, Biogeochemistry **44**, 163 (1999).

[4] T. Rahn, H. Zhang, M. Wahlen, and G. A. Blake, Res. Lett. **25**, 1189 (1998).

[5] D. Chakraborty and M. C. Lin, J. Phys. Chem. A **103**, 601 (1999).

[6] D. G. Hopper, J. Chem. Phys. **80**, 4290 (1984).

[7] A. Brown, P. Jimeno, and G. G. Balint-Kurti, J. Phys. Chem. A **103**, 11089 (1999).

[8] M. S. Johnson, G. D. Billing, A. Gruodis, and M. H. M. Janssen, J. Phys. Chem. A **105**, 8672 (2001).

[9] S. Nanbu and M. S. Johnson, J. Phys. Chem. A **108**, 8905 (2004).

[10] M. N. Daud, G. G. Balint-Kurti, and A. Brown, J. Chem. Phys. **122**, 054305 (2005).

[11] R. Schinke, J. Chem. Phys **134**, 064313 (2011).

[12] G. S. Selwyn and H. S. Johnston, J. Chem. Phys. **74**, 3791 (1981).

[13] A. G. Maki, J. S. Wells, and M. D. Vanek, J. Mol. Spectrosc. **138**, 84 (1989).

[14] J.-L. Teffo and A. Chendin, J. Mol. Spectrosc. **135**, 389 (1989).

[15] T. F. Hanisco and A. C. Kummel, J. Phys. Chem. **97**, 7242 (1993).

[16] A. Hishikawa, A. Iwamae, K. Hoshina, M. Kono, and K. Yamanouchi, Res. Chem. Intermed. **24**, 765 (1998).

[17] D. W. Neyer, A. J. R. Heck, and D. W. Chandler, J. Chem. Phys. **110**, 3411 (1999).

[18] M. Brouard, P. O'Keeffe, M. D. Joseph, and D. Minayev, Phys. Rev. Lett. **86**, 2249 (2001).

[19] M. Brouard, A. P. Clark, C. Vallance, and O. S. Vasyutinskii, J. Chem. Phys. **114**, 6690 (2001).

[20] S. H. M. Brouard and E. H. Fink, J. Chem. Phys. **97**, 7414 (1992).

[21] R. J. Donovan and D. Husain, Chem. Rev. **70**, 489 (1970).

[22] G. Black, T. G. Slanger, G. A. S. John, and R. A. Young, J. Chem. Phys. **51**, 116 (1969).

[23] C. Lin and F. Kaufman, J. Chem. Phys. **55**, 3760 (1971).

[24] D. Husain, L. J. Kirsch, and J. R. Wiesenfeld, Faraday Discuss. Chem. Soc **53**, 201 (1972).

[25] D. Husain, S. K. Mitra, and A. N. Young, J. Chem. Soc. Faraday Trans. 2 **70**, 1721 (1974).

[26] K. Sugawara, Y. Ishikawa, and S. Sato, Bull. Chem. Soc. Jpn. **53**, 3159 (1980).

[27] H. Umemoto, N. Hachiya, E. Matsunaga, A. Suda, and M. Kawasaki, Chem. Phys. Lett. **296**, 203 (1998).

[28] M. Born and J. R. Oppenheimer, Ann. Phys. **84**, 457 (1927).

[29] A. J. C. Varandas, Mol. Phys. **53**, 1303 (1984).

[30] A. J. C. Varandas, Adv. Chem. Phys. **74**, 255 (1988).

[31] A. J. C. Varandas, in *Lecture Notes in Chemistry*, edited by A. Laganá and A. Riganelli (Springer, Berlin, 2000), vol. 75, pp. 33–56.

[32] J. Li and A. J. C. Varandas, J. Phys. Chem. A **116**, 4646 (2012).

[33] J. Li, P. J. S. B. Caridade, and A. J. C. Varandas, J. Phys. Chem. A **118**, 1277 (2014).

Part I

Theoretical Background

Chapter 1

Concept of potential energy surface

Many aspects of chemistry can be reduced to questions about potential energy surfaces (PESs), which play an important role in the application of electronic structure methods to the study of molecular structures, properties and reactivities[1–5]. Within the Born-Oppenheimer (BO) approximation[6] for the separation of electronic and nuclear motions, the nuclei move on a PES following Newton's equations of motion. In this way, an electronic Schrödinger equation is solved for a set of fixed nuclear arrangements, yielding the potential energy surface for the nuclei motion through a specific electronic state, to obtained the resolution of the molecular problem within the so-called *adiabatic approximation*. In general, for a N atoms molecular system, the PES is a function of the $3N$ nuclear Cartesian coordinates, $\mathbf{x} = (x_1, y_1, z_1, ..., x_N, y_N, z_N)$, which is fully specified by $3N - 6$ linearly independent coordinates ($3N - 5$ for a linear molecule), since the Hamiltonian is invariant to a translation and rotation of the whole system. More detailed discussion on PES can be found elsewhere [2–4,7–9]. In the following, we review the main ideas related to molecular PES.

1.1 Molecular Schrödinger equation

The Schrödinger equation is the fundamental equation of non-relativistic quantum mechanics. It describes the temporal evolution of a state of a physical system. In principle,

the solution for the molecular problem of N nuclei and n electrons can be found in the time-independent non-relativistic Schrödinger equation,

$$\hat{H}_{\text{tot}}(\mathbf{R},\mathbf{r})\Psi_{\text{tot}}(\mathbf{R},\mathbf{r}) = E_{\text{tot}}\Psi_{\text{tot}}(\mathbf{R},\mathbf{r}), \tag{1.1}$$

where $\mathbf{r} = (r_i) = (x_i, y_i, z_i)$ and $\mathbf{R} = (R_i) = (X_i, Y_i, Z_i)$ are collective variables of the electronic and nuclear coordinates, respectively. E_{tot} is the total energy of the molecular system and Ψ_{tot} is the wave function of the $3n$ electronic coordinates, $\mathbf{r}$, and the $3N$ coordinates of the nuclei, $\mathbf{R}$. Here $\hat{H}_{\text{tot}}$ is many-body Hamiltonian operator, which can be represented as:

$$\hat{H}_{\text{tot}}(\mathbf{R},\mathbf{r}) = \hat{T}_{\text{N}}(\mathbf{R}) + \hat{T}_{\text{e}}(\mathbf{r}) + \hat{V}_{\text{NN}}(\mathbf{R}) + \hat{V}_{\text{ee}}(\mathbf{r}) + \hat{V}_{\text{Ne}}(\mathbf{R},\mathbf{r}) \tag{1.2}$$

where $\hat{T}_{\text{n}}$ and $\hat{T}_{\text{e}}$ represent nuclear and electronic kinetic operator, respectively:

$$\hat{T}_{\text{N}} = -\sum_{I}^{N}\left(\frac{1}{2M_I}\right)\nabla_I^2 \tag{1.3}$$

$$\hat{T}_{\text{e}} = -\frac{1}{2}\sum_{i}^{n}\nabla_i^2 \tag{1.4}$$

The symbol ∇_I^2 and ∇_i^2 are Laplacian operator involve differentiation with respect to the I-th nuclei coordinates, at position $\mathbf{R}_I$ and the i-th electron coordinates, at position $\mathbf{r}_i$, while M_I and m_i denote the nuclei and electronic masses. V_{NN} is the repulsive Coulomb interactions between the nuclei, while V_{ee} and V_{Ne} represent the electrostatic potential energy due to the repulsion between electrons and the interactions between electrons and nuclei, can be written as:

$$\hat{V}_{\text{NN}} = \frac{1}{2}\sum_{I=1}^{N-1}\sum_{J=I+1}^{N}\frac{Z_I Z_J}{|\mathbf{R_I} - \mathbf{R_J}|} \tag{1.5}$$

$$\hat{V}_{\text{ee}} = \frac{1}{2}\sum_{i=1}^{n-1}\sum_{j=i+1}^{n}\frac{1}{|\mathbf{r_i} - \mathbf{r_j}|} \tag{1.6}$$

$$\hat{V}_{\text{Ne}} = -\sum_{I=1}^{N}\sum_{i=1}^{n}\frac{Z_I}{|\mathbf{R}_I - \mathbf{r}_i|} \tag{1.7}$$

where Z_I and Z_J are the atomic number of nuclei I and J. Atomic units have been used here and throughout this work unless indicated otherwise.

Unfortunately, a closed form solution of the Schrödinger equation is only for the simplest systems which contain no more than two interacting particles, typical example is H atom, but it is not possible for more than two particles owing to the correlation of all particles with each other. In order to simplify the eigenvalue problem a number of approximations like the Born-Oppenheimer (BO) approximation, the introduction of one-electron equations, the concept of orbitals, and the basis sets used to construct them are common to most *ab initio* methods. For more than half century, quantum chemists have been working within these approximations, as it is thought necessary to build up an adequate representation of the given surface.

1.2 Born-Oppenheimer approximation

It is difficult to solve the Schrödinger equation (1.1), because it arises from the large number of variables the many-body wave function, Ψ, depends on. For a system consisting of n electrons and N nuclei, there are $3n+3N$ degrees of freedom, three spatial coordinates for each electron and for each nucleus. Born and Oppenheimer showed in 1927[6] that to a very good approximation the nuclei in a molecule are stationary with respect to electrons. Since the nuclei are much heavier than the electrons (nuclei are approximately 10^3 to 10^5 times heavier than electrons), their motion will be much slower, the characteristic time scales of processes involving the electrons are much smaller. Hence, it is assumed that when a nuclei moves the electrons immediately recorder themselves around it. In other words, the electronic wave functions can be found by assuming that the nuclei are fixed in space. The nuclei coordinates are just parameters in the electronic Schrödinger equation and the nuclear and electronic motions are thus said to be decoupled. Therefore, the total wave function of a given electronic state can split into two components: one which describes the nuclear motion, $\chi(\mathbf{R})$, and one which describes the electronic motion, $\psi(\mathbf{R}, \mathbf{r})$, for a fixed nuclear coordinates, $\mathbf{R}$, can be written as:

$$\Psi_{\text{tot}}(\mathbf{R}, \mathbf{r}) = \chi(\mathbf{R})\psi(\mathbf{R}, \mathbf{r}) \tag{1.8}$$

first, it is assumed that we could solve the electronic problems for a fixed nuclei configuration. The electronic wave function $\psi(\mathbf{R}, \mathbf{r})$ is obtained as the solution to

$$\left(-\frac{1}{2} \sum_{i}^{n} \nabla_i^2 + \hat{V}_{ee}(\mathbf{r}) + \hat{\mathbf{V}}_{\mathbf{Ne}}(\mathbf{R}, \mathbf{r}) \right) \psi(\mathbf{R}, \mathbf{r}) = E_e(\mathbf{R}) \psi(\mathbf{R}, \mathbf{r}) \tag{1.9}$$

describing the motion of the n electrons in the electrostatic field generated by the N nuclei. This equation must be soled for each set of fixed nuclear positions $\mathbf{R}$, and consequently the electronic eigenvalue E_e depends explicitly on $\mathbf{R}$. The nuclei, in turn, are assumed to move according to the atomic Schrödinger equation:

$$\left(-\sum_{I}^{N} \left(\frac{1}{2M_I} \right) \nabla_I^2 + \hat{V}_{NN}(\mathbf{R}) + \mathbf{E_e}(\mathbf{R}) \right) \chi(\mathbf{R}) = E_n \chi(\mathbf{R}) \tag{1.10}$$

With this approximation, the molecular problem is reduced to the solution of the nuclear motion on a single potential energy surface where the electronic energy $E_e(\mathbf{R})$ plays the part of the potential energy of nuclei

$$V(\mathbf{R}) = \mathbf{\frac{1}{2}} \sum_{\mathbf{I=1}}^{\mathbf{N-1}} \sum_{\mathbf{J=I+1}}^{\mathbf{N}} \frac{\mathbf{Z_I Z_J}}{|\mathbf{R_I} - \mathbf{R_J}|} + \mathbf{E_e}(\mathbf{R}) \tag{1.11}$$

That we will call it *potential energy surface* (PES), and it is also called *potential* because it is the potential energy in the dynamical equation of nuclear motion, being one of the most important concept in physical chemistry. within the BO approximation first the electronic eigenvalue equation Eq.(1.9), has to be solved, and then Eq.(1.11) is applied to obtain the PES. It is noted the electronic Schrödinger equation, Eq.(1.9), has an infinite number of solutions. In many cases one is just interested in the solution with the lowest energy, which corresponding to the ground state of the electronic system.

As we here just want to show how the concept of potential energy surface arises, our discussion of BO approximation is essentially qualitative. In turn, many detailed description of this approximation, such as, its validity, its generalization, the problem of deriving corrections to it and many other aspects are thoroughly discussed in the literature.[3,10–16]

1.3 Choice of coordinates

There is no one set of coordinates for defining the geometry of a polyatomic system which is convenient for all types of dynamical calculations. One must be prepared to change potential functions from one coordinate to another, which is straightforward but sometimes tedious procedure. For molecules with $N > 2$, the representation of $V(\mathbf{R})$ requires the specification of $3N - 6$ independent internal coordinates. The reason why we try to express the PES in terms of internal coordinates, rather than the $3N$ atomic Cartesian coordinates, is that the PES will automatically be unchanged by the operation of rotation and inversion of the molecule as a whole. The energy is actually only a function of the relative positions of the atoms, not depend on the three coordinates that specify the position of the molecule as a whole or on the three coordinates needed to specify the orientation of the molecule. The most convenient coordinates consist of internuclear distances or bond angles for small polyatomic molecules $N < 4$. In dynamics calculations employing a global PES, the intermolecule distance offer a good choice as they treat all parts of the nuclear configurational space on equal footing, allowing also to set up functions with the correct permutational symmetry for systems containing. One should notice that the number of independent vibrational normal modes for a linear molecule is $3N - 5$, but two of these are degenerate and therefore distinguishable as far as the potential energy is concerned. In general, $V(\mathbf{R})$ is obtained as a potential energy hypersurface in a $3N - 5$-dimensional space. Hence, in the case of a triatomic molecule one has a total of four coordinates: three configurational (e.g., three internuclear distances or two distances and an angle) and the potential energy. It should be noted that for $N > 4$ system, the number of internal coordinates $N(N-1)/2$ exceeds $3N-6$, which leads to some ambiguity in the selection of a set of internuclear coordinates.

It is also convenient to use the symmetry coordinate that from the irreducible basis of the molecular symmetry group. This is because the potential energy surface, being a consequence of the Born-Oppenheimer approximation and as such independent of the atomic masses, must be invariant with respect to the interchange of equivalent atoms inside the molecule. The symmetry coordinates show themselves to be particular useful

fro the functional representation of the molecular potential.

Traditional types of coordinate include also the valence internal coordinates. Then, the potential energy surface can be written as a sum of simple terms containing empirically determined parameters, describing the energies associated with displacement of individual bond lengths, bond angles, wag angles and dihedral angles from the corresponding equilibrium values; such surface are good at describing dynamical processes that do not involve the making or breaking of bonds, such as conformational transitions that occur in protein folding. The potential energy surfaces used in this thesis work are all expressed in the internuclear distances.

1.4 Features of potential energy surfaces

Potential energy surfaces are important because they aid us in visualizing and understanding the relationship between potential energy and molecular geometry. The most important features of PESs for discussing the chemical reactions are its stationary points, those on a PESs are points at which surfaces are flat, i.e. parallel to horizontal line corresponding to one geometric parameter (or to the plane corresponding to two geometric geometric parameters, or to the hyperplane corresponding to more than two geometric parameters). A marble placed on a stationary point will remain balanced, i.e. stationary. At any other point on a potential surface the marble will roll toward a region of lower potential energy. Mathematically, a stationary point is one at which the first derivative of the potential energy with respect to each geometric parameter is zero:

$$\frac{\partial V}{\partial q_1} = \frac{\partial V}{\partial q_2} = ... = 0 \tag{1.12}$$

These stationary points can be distinguished by the second derivatives of the potential energy in terms of the internal coordinate, according to the number of positive, negatives and zero eigenvalues of the $(3N-6) \times (3N-6)$ with elements, we can get:

For a minimum, along all the reaction coordinate q

$$\frac{\partial^2 V}{\partial q^2} > 0 \tag{1.13}$$

For a transition state, for all q

$$\frac{\partial^2 V}{\partial q^2} > 0 \tag{1.14}$$

but except along the reaction coordinate

$$\frac{\partial^2 V}{\partial q^2} < 0 \tag{1.15}$$

Thus, if all of the eigenvalue of the Hessian matrix are positive, the stationary point is a minimum with all real frequencies, which occupies the lowest-energy point in the region of the PES, may corresponding to reactants, products or intermediates. If the minimum is the lowest-energy minimum on the whole PES, we called it is a global minimum.

The transition state linking the two minima represents a maximum along the direction of the intrinsic reaction coordinate, but along all other directions it is a minimum. This is a characteristic of a saddle-shaped surface, and the transition state is called a saddle point. Transition state is a first order saddle point, with only one negative eigenvalue, are of particular interest in chemical kinetics because they lie on the paths between points on the surface identified with reactant and points on the surface identified with product species, offering a practical way of tracing those paths in a steepest descent manner. Some PESs have points where the second derivative of energy with respect to more than one coordinate is negative; these are higher-order saddle point; for example, a second-order saddle point is a point on the PES which is a maximum along two paths connecting stationary points, thence of little relevance in kinetics.

The location of stationary point on the PES could be achieved by many different methods [17–22], and the literature cited therein.

1.5 Crossing of adiabatic potentials

The adiabatic potentials $E_j(\mathbf{R})$ can sometimes cross or come near each other at some nuclear configurations. This corresponds to the case of degeneracy or quasi degeneracy of electronic states. In order for adiabatic potentials to cross, certain conditions must be satisfied. Usually, the crossing of adiabatic potentials that belong to the same electronic

symmetry can only occur at nuclear configurations that correspond to certain symmetries of the molecular configuration. This does not apply to adiabatic states that have different symmetries[4]. The following is a simple heuristic derivation of the condition for the crossing of two adiabatic potential curves which are of the same symmetry.

For a coupled two state problem, let ψ_1 and ψ_2 be the wavefunctions of two electronic states which have the same symmetry and spin. We assume that these two wave functions can be written as a linear combination of two orthonormal basis functions ψ_a and ψ_b. In that case, the energies of the two states are the eigenvalues of the 2×2 hermitian matrix

$$\begin{pmatrix} H_{\mathrm{aa}} & H_{\mathrm{ab}} \\ H_{\mathrm{ab}} & H_{\mathrm{bb}} \end{pmatrix} \tag{1.16}$$

By diagonalizing the matrix operator H, we obtain the adiabatic potentials

$$V_{\pm} = \frac{H_{\mathrm{aa}} + H_{\mathrm{bb}}}{2} \pm \frac{1}{2}\sqrt{(H_{\mathrm{aa}} - H_{\mathrm{bb}})^2 + 4|H_{\mathrm{ab}}|^2} \tag{1.17}$$

and the gap between the two adiabatic potentials is given by

$$\Delta V = V_+ - V_- = \sqrt{(H_{\mathrm{aa}} - H_{\mathrm{bb}})^2 + 4|H_{\mathrm{ab}}|^2} \tag{1.18}$$

For two adiabatic potentials to cross, the two positive terms in (1.18) must satisfy the following equations simultaneously

$$\begin{cases} H_{\mathrm{aa}}(R) = H_{\mathrm{bb}}(R) \\ H_{\mathrm{ab}}(R) = 0 \end{cases} \tag{1.19}$$

If ψ_a and ψ_b have different symmetries then H_{ab} will be zero for all values of R. In that case there may be a point or points at which (1.19) is satisfied, i.e. the energies of two states are equal. These points will then be crossing points of the potential energy curves[2,23,24].

Bibliography

[1] A. J. C. Varandas, *Conical Intersections Electronic Structure, Dynamics and Spectroscopy* (World Scientific, 2004), chap. Modeling and interpolation of global multi-sheeted potential energy surfaces, p. 205.

[2] J. N. Murrell, S. Carter, S. C. Farantos, P. Huxley, and A. J. C. Varandas, *Molecular Potential Energy Functions* (Wiley, Chichester, 1984).

[3] A. J. C. Varandas, in *Lecture Notes in Chemistry*, edited by A. Laganá and A. Riganelli (Springer, Berlin, 2000), vol. 75, pp. 33–56.

[4] J. Z. H. Zhang, *Theory and Applications of Quantum Molecular Dynamics* (World Scientific, Singapore, 1999).

[5] A. J. C. Varandas, Int. Rev. Phys. Chem. **19**, 199 (2000).

[6] M. Born and J. R. Oppenheimer, Ann. Phys. **84**, 457 (1927).

[7] A. S. Davidov, *Quantum Mechanics* (Pergamon, Oxford, 1965).

[8] H. Eyring and S. H. Lin, in *Physical Chemistry, An Advanced Treatise, Vol. VIA, Kinetics of Gas Reactions*, edited by H. Eyring, D. Henderson, and W. Jost (Academic, New York, 1974), p. 121.

[9] R. Jaquet, *Potential Energy Surfaces* (Springer, 1999), chap. Interpolation and fitting of potential energy surfaces, Lecture Notes in Chemistry.

[10] C. A. Mead and D. G. Truhlar, J. Chem. Phys. **70**, 2284 (1979).

[11] C. A. Mead, J. Chem. Phys. **72**, 3839 (1980).

[12] D. R. Yarkoni, Rev. Mod. Phys. **68**, 985 (1996).

[13] W. Kutzelnigg, Molecular Physics **90**, 909 (1996).

[14] J. Hinze, A. Alijah, and L. Wolniewicz, Polish J. Chem. **72**, 1293 (1998).

[15] M. Baer, prp **358**, 75 (2002).

[16] B. Kendrick, C. A. Mead, and D. G. Truhlar, Chem. Phys. Lett. **277**, 31 (2002).

[17] H. B. Schlegel, Ab Initio Meth. Quant. Chem. **I**, 249 (1987).

[18] J. D. Head, B. Weiner, and M. C. Zerner, Int. J. Quantum Chem. **33**, 177 (1988).

[19] H. B. Schlegel, Rev. Comput. Chem **3**, 1 (1992).

[20] M. L. McKee and M. Page, Rev. Comput. Chem **4**, 35 (1993).

[21] H. B. Schlegel, *in Modern Electronic Structure Theory*, vol. I (World Scientific, Singapore, 1995).

[22] K. Bondensgard and F. Jensen, J. Chem. Phys. **104**, 8025 (1996).

[23] C. A. Mead, J. Chem. Phys. **70**, 2276 (1982).

[24] H. C. Longuet-Higgins, Proc. R. Soc. Ser. A **344**, 147 (1975).

Chapter 2

Calculation and modeling of potential energy surfaces

The potential energy surface (PES), which is indeed a function obtained by fitting to the *ab initio* energies, should describe the molecular energy as the internuclear distance is changing continuously. *Ab initio* energies used to map a PES can be gathered by solving the electronic problem represented in (1.9). Methods aimed at solving (1.9) are broadly referred to the electronic structure calculation[1] and significant advances have been made over many years[2] in the accurate *ab initio* evaluation of the molecular energy within the Born-Oppenheimer approximation (BOA)[3,4]. The most common type of *ab initio* calculation is the Hartree-Fock (HF) calculation[5,6]. At higher levels of approximation, the quality of the wave function is improved, so as to yield more and more elaborate solutions.

A large number of *ab initio* methods are available in many package program to perform high level electronic structure calculations, such as Gaussian03[7], GAMESS[8] and Molpro[9]. In the following sections, a brief discussion of *ab initio* methods, adopted for the calculation of PESs is presented.

2.1 Variational principle and molecular orbitals

2.1.1 The variational principle

Given a system with a Hamiltonian $\hat{H}$, the variation theorem[3] states that, if any normalised electronic wavefunction $\psi(\mathbf{r})$ satisfies the boundary conditions of the Hamiltonian, which need not be the true solution of the Schrödinger equation (1.9), the expectation value of the $\hat{H}$ corresponding to $\psi(\mathbf{r})$ will be always greater than or equal to the ground state E_0 of the electronic Schrödinger equation (1.9):

$$\langle\psi|\hat{H}|\psi\rangle \geq E_0 \tag{2.1}$$

Hence, finding the ground state energy and wave function of a many-body system can be formulated as a variational minimization problem:

$$\delta\langle\psi_0|\hat{H}|\psi_0\rangle = 0 \tag{2.2}$$

In the electronic problem (1.9), the wavefunction depends on the coordinates of all electrons. As a next approximation the trial molecular wave functions are chosen as combinations of single electron functions, so called *Slater determinants*[10]. Therefore, a general method is needed to construct electron wavefunctions which are completely antisymmetric in all cases. For this purpose, we can use the complete antisymmetry property of determinants. Since interchanging any two rows (or columns) of a determinant changes the sign of the determinant, completely antisymmetric wavefunctions can be expressed in the form of a determinant.

Let us consider the case of n electrons. Let ψ_1 , . . . , ψ_n be some arbitrary "one-particle states" of electrons. By a "one-particle state" we mean the spin and space part of a wave function of single electron. So, for the state where these n electrons are in these

n one-particle states, the wave function of the whole system can be written as:

$$\Psi(1,2,...n) = \frac{1}{\sqrt{n!}} \begin{vmatrix} \psi_1(1) & \psi_1(2) & \cdot & \cdot & \cdot & \psi_1(n) \\ \psi_2(1) & \psi_2(2) & \cdot & \cdot & \cdot & \psi_2(n) \\ \cdot & \cdot & \cdot & & & \cdot \\ \cdot & \cdot & & \cdot & & \cdot \\ \cdot & \cdot & & & \cdot & \cdot \\ \psi_n(1) & \psi_n(2) & \cdot & \cdot & \cdot & \psi_n(n) \end{vmatrix} \tag{2.3}$$

This expression is called as the Slater determinant of n states ψ_1 , . . . , ψ_n. As can be seen, exchanging the coordinates of ith and jth particles' coordinates is equivalent to interchanging ith and jth columns of the determinant. As a result, exchange of any two particles' coordinates changes the sign of the wave function of the system Ψ. We have managed to obtain a totally antisymmetric wave function. We should also note that, since the determinant is also totally antisymmetric rowwise, interchanging the places of any two one-particle states will change the sign of Ψ. One implication of this property is that when you have chosen a set ψ_1 , . . . , ψ_n such that two states are the same, e.g., $\psi_i = \psi_j$, then the wave function of the system is identically zero. This is because, when you interchange the positions of ith and jth states, Ψ should remain the same since the one-particle-state set is unchanged. On the other hand, it should change sign because of the antisymmetry of the determinant. Last two sentences are consistent only if Ψ is identically zero. Since an identically zero wave function is not possible in quantum mechanics, we should have distinct one-particle states in the set ψ_1 , . . . , ψ_n. This is the famous *Pauli exclusion principle* formulated by the Austrian physicist Wolfgang Pauli in 1925: Two electrons in a system can never be in the same one-particle state.

2.1.2 Molecular orbitals

A molecular orbital (MO) can specify the electron configuration of a molecule: the spatial distribution and energy of one (or one pair of) electron(s). Each MO is built up from a

linear combination of atomic orbitals (LCAO):

$$\Psi_{MO} = \sum_{i=1}^{I} C_i \chi_i \tag{2.4}$$

where χ_i are atomic orbitals, the variational principle justifies minimization of the energy by adjustment of the coefficients C_i.

2.2 Hartree-Fock theory

A full quantum solution of the complicated many-electron problem (**??**) is very difficult, because these problems involve a number of electrons around a number of atomic nuclei. However, approximations can be made, the real skill you need to master is solving the wave function for the electrons given the positions of the nuclei. But even given the positions of the nuclei, a brute force approach for any many-electron problem turns out to be too laborious. The Hartree-Fock (HF) approximation is one of the most important ways to tackle that problem, and has been so since the early days of quantum mechanics. The HF method seeks to approximately solve the electronic Schrödinger equation and it assumes that the full many-body wave function can be approximated by a single Slater determinate, whose elements are one electron orbitals with orbital and spin part. Since the energy expression is symmetric, the variational theorem holds, and so we know that the Slater determinant with the lowest energy is as close as we can get to the true wave function for the assumed functional form of a single Slater determinant. The Hartree-Fock method determines the set of spin orbitals which minimize the energy and give us this *best single determinant.* This section explains some of the ideas.

2.2.1 Simplified the Hamiltonian

The full Hamiltonian (in atomic units) for a system of n electrons in the presence of N nuclei with charge Z_A is:

$$\hat{H} = \sum_{i}^{n} \hat{h}(i) + \frac{1}{2} \sum_{i}^{n} \sum_{j>i}^{n} \frac{1}{r_{ij}} \tag{2.5}$$

where the one-electron operator $\hat{h}(i)$ are the sum of kinetic energy operator and the operator corresponding to the attraction of the electrons to the nuclei, can be written as:

$$\hat{h}(i) = -\frac{1}{2}\nabla_i^2 + \sum_A^N \frac{Z_A}{r_{iA}} \tag{2.6}$$

and the two-electron operator $\hat{v}(i,j)$ corresponding to the electron-electron repulsion

$$\hat{v}(i,j) = \frac{1}{r_{ij}} \tag{2.7}$$

2.2.2 Energy expression

We state that the Hartree-Fock wavefunction will have the form of a Slater determinant, and that the energy will be given by the usual quantum mechanical expression:

$$E_0 = \langle \Psi_0 | \hat{H}_e | \Psi_0 \rangle \tag{2.8}$$

For symmetric energy expressions, we can employ the variational theorem, which states that the energy is always an upper bound to the true energy. Hence, we can obtain better approximate wavefunctions Ψ by varying their parameters until we minimize the energy within the given functional space. Hence, the correct molecular orbitals are those which minimize the electronic energy E_n! The molecular orbitals can be obtained numerically using integration over a grid, or much more commonly as a linear combination of a set of given basis functions. Then, we can re-write the Hartree-Fock energy E_n in terms of integrals of the one- and two-electron operators:

$$E_0 = \sum_i^N \langle i|h|i\rangle + \frac{1}{2}\sum_i^N \sum_j^N \langle ii|jj\rangle - \langle ij|ji\rangle \tag{2.9}$$

The summation indices i and j range over all occupied spin-orbitals. where the one-electron integral is

$$\langle i|h|j\rangle = \int dx_1 \chi_i^*(\mathbf{x_1}) h(\mathbf{r_1}) \chi_j(\mathbf{x_1}) \tag{2.10}$$

and two-electron integral is

$$\langle ij|kl\rangle = \int dx_1 dx_2 \chi_i^*(\mathbf{x_1}) \chi_j(\mathbf{x_1}) \frac{1}{r_{12}} \chi_k^*(\mathbf{x_2}) \chi_l(\mathbf{x_2}) \tag{2.11}$$

2.2.3 The Hartree-Fock equations

For the purpose of deriving the variation of the expectation value E_0, it is convenient to express the energy in terms of Coulomb (J) and exchange (K) operators.

$$J_i(1)|\chi_j(1)\rangle = \langle i|\frac{1}{r_{12}}|i\rangle|\chi_j(1)\rangle = \left[\int \chi_i^*(2)\frac{1}{r_{12}}\chi_i(2)d\tau_2\right]\chi_j(1) \tag{2.12}$$

$$K_i(1)|\chi_j(1)\rangle = \langle i|\frac{\hat{P}_{12}}{r_{12}}|j\rangle|\chi_j(1)\rangle = \left[\int \chi_i^*(2)\frac{1}{r_{12}}\chi_j(2)d\tau_2\right]\chi_i(1) \tag{2.13}$$

Substituting (2.12) and (2.13), the expectation value in (2.9) becomes

$$E_0 = \sum_i^N \langle\chi_i|\hat{h}_i|\chi_i\rangle + \frac{1}{2}\sum_{ij}\left(\langle\chi_j|J_i|\chi_j\rangle - \langle\chi_j|K_i|\chi_j\rangle\right) \tag{2.14}$$

For searching the optimal wavefunction, we must impose the constraint that all the spin-orbitals remain orthonormal, i.e.

$$\langle i|j\rangle - \delta_{ij} = 0 \tag{2.15}$$

for i=1,2,...,N and j=1,2,...,N, a total of N^2 constrains.

The standard method for finding an minimum or maximum subject to a constraint is Lagrange's method of undetermined multipliers: The constraint equations are each multiplied by some constant and added to the expression to be optimized. Thus, we define a new quantity L:

$$L = E_0 - \sum_i^N\sum_j^N \lambda_{ij}(\langle i|j\rangle - \delta_{ij}) \tag{2.16}$$

The Lagrange function is stationary with respect to an orbital variation

$$\delta L = \delta E_0 - \sum_{i=1}^N\sum_{j=1}^N \lambda_{ij}\delta\langle i|j\rangle = 0 \tag{2.17}$$

We now evaluate the terms on the right hand side of this expression. Inserting the new spin-orbitals $\chi_i + \delta\chi_i$, etc. into the expression for E_0, the variation energy of the

energy is given by

$$\begin{aligned}\delta E_0 &= \sum_i^N (\langle \delta\chi_i|\hat{h}_i|\chi_i\rangle + \langle\chi_i|\hat{h}_i|\delta\chi_i\rangle) + \\ &\quad \sum_{ij} (\langle\delta\chi_j|J_i - K_i|\chi_j\rangle + \langle\chi_i|J_j - K_j|\delta\chi_i\rangle) \\ &= \sum_i^N (\langle\delta\chi_i|\hat{F}_i|\delta\chi_i\rangle + \langle\chi_i|\hat{F}_i|\delta\chi_i\rangle) \end{aligned} \tag{2.18}$$

where $\hat{F}_i$ is the Fock operator written as

$$\hat{F}_i = \hat{h}_i + \sum_i^N (J_i - K_i) \tag{2.19}$$

Making use of (2.17) to (2.19) and $\langle\chi|\delta\chi\rangle = \langle\delta\chi|\chi\rangle^*$ and $\langle\chi|\hat{F}|\delta\chi\rangle = \langle\delta\chi|\hat{F}|\chi\rangle^*$, And now the Hartree-Fock equations are just

$$\hat{F}_i\chi_i = \lambda_i\chi_i \tag{2.20}$$

Introducing a basis set transforms the Hartree-Fock equations into the Roothaan equations. Denoting the atomic orbital basis functions as $\tilde{\chi}$, we have the expansion

$$\chi_i = \sum_{\mu=1}^N C_{\mu i}\tilde{\chi}_\mu \tag{2.21}$$

for each spin orbital. This leads to

$$\hat{F}_i \sum_{\nu=1}^N C_{\nu i}\tilde{\chi}_\nu = \lambda_i \sum_{\nu=1}^N C_{\nu i}\tilde{\chi}_\nu \tag{2.22}$$

Left multiplying by $\tilde{\chi}^*_{mu}$ and integrating yields a matrix equation

$$\sum_\nu C_{\nu i} \int dx_1 \tilde{\chi}^*_\mu(x_1)\hat{F}_i(x_1)\tilde{\chi}^*_\nu(x_1) = \lambda_i \sum_\nu C_{\nu i} \int dx_1 \tilde{\chi}^*_\mu(x_1)\tilde{\chi}^*_\nu(x_1) \tag{2.23}$$

Introducing the matrix element notation, then it can be simplified

$$S_{\mu\nu} = \int dx_1 \tilde{\chi}^*_\mu(x_1)\tilde{\chi}^*_\nu(x_1) \tag{2.24}$$

$$F_{\mu\nu} = \int dx_1 \tilde{\chi}^*_\mu(x_1) \hat{F}_i(x_1) \tilde{\chi}^*_\nu(x_1) \tag{2.25}$$

Now we can get the Hartree-Fock-Roothaan equations in matrix form as

$$\sum_\nu F_{\mu\nu} C_{\nu i} = \lambda_i \sum_\nu S_{\mu\nu} C_{\nu i} \tag{2.26}$$

or more simply form

$$\mathbf{FC} = \lambda \mathbf{SC} \tag{2.27}$$

where λ is a diagonal matrix of the orbital energies λ_i. Except for the overlap matrix S, it is like an eigenvalue equation. We can make a transformation of basis to an orthogonal basis to vanish S. Then it is just a matter of solving an eigenvalue equation. Since F depends on its own solution through the orbitals, the process must be done iteratively. This is why the solution of the Hartree-Fock-Roothaan equations are often called the self-consistent-field procedure.

2.3 CI method

The Hartree-Fock method produces an energy that is higher than the actual value, due to the approximation of the Schrödinger equation is not actually separable, so in this respect the molecular orbital approximation introduces inaccuracy. Also, it only treats coulombic repulsion between electrons in an average way, discarding the the instantaneous interaction between electrons. The difference between the exact non-relativistic energy and the non-relativistic Hartree-Fock energy, that is referred to as electron correlation, can be noted as the correlation energy:

$$E_{corr} = E_{exact} - E_{HF} \tag{2.28}$$

Configuration interaction[11] (CI) is a method that includes instantaneous electron correlation. The exact wavefunction is represented as a linear combination[12] of N-electron configurations, and optimise the coefficients of the different configurations, using the linear variational method.

$$\Phi = \sum_k c_k \Phi_k \tag{2.29}$$

We often write the ground-state HF wave function as Φ_0, the Slater determinant with an electron "excited" from the ith occupied orbital to the ath unoccupied orbital as Φ_i^a, the "doubly-excited" Slater determinants as Φ_{ij}^{ab}, etc.. With this notation, we can rewrite the wave function in (2.29) as

$$\Phi = c_0\Phi_0 + \sum_{i=1}^{N}\sum_{a=N+1}^{M} c_i^a\Phi_i^a + \sum_{i>j=1}^{N}\sum_{a>b=N+1}^{M} c_{ij}^{ab}\Phi_{ij}^{ab} + \cdots \tag{2.30}$$

where N is the number of electrons, so M is the total number of the HF orbitals. In principle, the basis set of N-electron wavefunctions used could be complete, in which case an exact energy would be obtained. This is called full configuration interaction (FCI), which has the following expression[13]

$$N_{\text{tot}} = \binom{M}{N} = \frac{M!}{N!(M-N)!} \tag{2.31}$$

For sufficiently large M, the FCI calculation will give an essentially exact result. However, FCI calculations are extremely expensive, and so generally the basis set is limited to a finite size. When we truncate at zeroth-order, we have the HF approximation[5,6]. At first order, only one electron has been moved for each determinant, it is called a Configuration Interaction with Single excitation (CIS)[1]. CIS calculations give an approximation to the molecular excited states, but not change the ground state energy. At second order, we have Configuration Interaction with Single and Double excitation (CISD)[1,14] yielding a ground-state energy that has been corrected for correlation. Triple-excitation (CISDT)[1] and quadruple-excitation(CISDTQ)[1] calculations are done only when very high accuracy results are desired. For most applications, the CIS and CISD can give good description of the electronic correlation energy.

2.4 MCSCF method

The wavefunction in HF theory is defined as a single Slater determinant, while such a wavefunction could provide an efficient reference state for more extensive calculations. However, single determinantal wave functions are inherently incapable of describing the

correlation associated with the mutual repulsion of electrons. HF determinate does not dominate the wave function, or sometimes may be just one of a number of important electronic configuration, wherever bonds are being broken or formed (where the occupied and unoccupied orbitals converge in energy as the bond is stretched). For these situation, one must seek from the outset to have a first description of the system that is better than HF method. Although in principle, the CI scheme offers a method of refining the wave function to any degree of accuracy, progress along this path has been unsatisfactory due to the notoriously slow convergence of the CI expansion.

Multi-configurational self-consistent field (MCSCF)[15–17] is a method in quantum chemistry used to generate qualitatively correct reference states of molecules in cases where HF theory is not adequate. In the MCSCF method, one use M one-particle functions ($M > N$) to approximate the total wave function of an N-particle system:

$$\Psi_M = \{\psi_1 \psi_2 \cdots \psi_M\} \tag{2.32}$$

This allows us to construct $\binom{M}{N}$ Slater determinate ϕ_k corresponding to ordered configuration $k = (k_1 k_2 \cdots k_N)$. The total wavefunction is an engenfunction of the Hamitonian $\hat{H}$, which can be expressed in eq.(2.30). The optimum coefficients C_k are obtained using variational principle $\delta\langle\hat{H}\rangle = 0$ with fixed Ψ_M:

$$\sum_k (\langle k|\hat{H}|l\rangle - \lambda\delta_{kl})C_l = 0 \tag{2.33}$$

for fixed M, if one simultaneously varies the set Ψ_M and the coefficients C, the better and better energies will be obtained until finally a certain minimum is achieved. This formalism leads to the MCSCF method and was first suggested by Frenkel[18]. The MCSCF calculation can five the most rapidly convergent configuration expansion functions, which accomplished by minimizing the energy not only with respect to the configuration mixing coefficients but also with respect to the orbital expansion coefficients.

A successful approach, which is known as the complete active space self-consistent field (CASSCF) method[16,17], to select the MCSCF configurations is to partition the molecular orbital space into three subspaces, containing inactive, active and virtual (or unoccupied) orbitals respectively. Typically, the core orbitals of the system are treated as inactive and

the valence orbitals as active. Thus, keeping the core orbitals doubled occupied in all configurations, the complete active space (CAS) consists in all configurations obtained by distributing the valence electrons in all possible ways in the active orbitals, which is usually called full valence complete active space (FVCAS)[17]. The configuration so obtained is often referred to as reference configuration and the corresponding space spanned is called the reference space.

In a CASSCF wave function, a part of the electronic correlation called static or nondynamical correlation is recovered, which arise from the strong interaction between configurations nearly degenerated and is unrelated to the instantaneous repulsion between the electrons. This last energy contribution constitutes the dynamical correlation energy. For high accuracy treatment of dynamical correlation, additional calculations must be carried out based on the initial MCSCF method, such as multiferncе CI (MRCI) method[19–23], employed in this thesis will be described in next section.

2.5 MRCI method

The multireference configuration interaction (MRCI) method consists in a CI expansion of the eigenstates of the electronic molecular Hamiltonian in a set of Slater determinants which correspond to excitations of the ground state electronic configuration but also of some excited states. The MRCI wavefunction and its general form, including only all the single and double excitations (MRCISD), can be written as[24]

$$|\Psi\rangle = \sum_I C^I |\Psi_I\rangle + \sum_S \sum_a C_a^S |\Psi_S^a\rangle + \sum_P \sum_{ab} C_{ab}^P |\Psi_P^{ab}\rangle \tag{2.34}$$

where a and b refer to external orbitals, *i.e.*, those not occupied in the reference configurations, I denotes an orbital configuration with N electrons in the internal orbital space while S and P denote internal $N-1$ and $N-2$ electronic hole states[24–26]. $|\Psi_I\rangle$, $|\Psi_S^a\rangle$ and $|\Psi_P^{ab}\rangle$ are internal, singly external and doubly external configurations containing 0, 1, 2 occupied external orbitals, respectively.

It is difficult to perform uncontracted MRCI calculations with large reference configuration spaces (and large basis sets) which is generated by two electron excitations from

each individual reference configuration, because usually there are many more external orbitals than internal ones, the double external CSF's $|\Psi_P^{ab}\rangle$ are the most numerous in (2.34). If this number is denoted as N_P and the number of external orbitals denoted as N, then the number of operations per iteration is proportional to $N_P N^4 + N_p^x N^3$ [24], where $1 < x < 2$. Different contraction schemes have been proposed [24,27–30] to reduce the computational effort. In the hybrid internally contracted MRCI (ICMRCI) [22,24?] , the internal configurations Ψ_{ij}^{kl} and singly external configurations Ψ_{ij}^{ka} are not contracted, while the doubly external configurations Ψ_{ij}^{ab} are contracted.

In the "externally" contracted CI [25,31] the singly and doubly external configurations are contracted as

$$|\Psi^{\mathrm{S}}\rangle = \sum_a \alpha_a^S |\Psi_S^a\rangle \tag{2.35}$$

$$|\Psi^{\mathrm{P}}\rangle = \sum_{ab} \alpha_{ab}^P |\Psi_P^{ab}\rangle \tag{2.36}$$

where the contraction coefficients α are obtained by first order perturbation theory.

In another contraction scheme the configurations are generated by applying pair excitation operators[2] to the reference wave function as a whole. This effectively generates linear combinations of the configurations Ψ_{ab} with different P internal states P and is therefore called *internally contracted CI* [22,32]. In the Werner and Knowles proposal [19], the internally contracted doubly external configurations are defined as

$$|\Psi_{kl,\omega}^{ab}\rangle = \frac{1}{2}\left(\hat{E}_{ak,bl} + \omega \hat{E}_{bk,al}\right)|\Psi_0\rangle \tag{2.37}$$

where $\omega = 1$ for external singlet pairs and $\omega = -1$ for external triplet pairs, and $|\Psi_0\rangle$ is a reference wavefunction, which may be composed of many configurations

$$|\Psi_0\rangle = \sum_R \alpha^R |\Psi_R\rangle \tag{2.38}$$

The internally contracted configurations $|\Psi_{kl,w}^{ab}\rangle$ can be expanded in terms of the set of standard uncontracted doubly external CSFs $|\Psi_p^{ab}\rangle$ according to

$$|\Psi_{kl,\omega}^{ab}\rangle = \sum_P \langle \Psi_P^{ab} | \Psi_{kl,\omega}^{ab}\rangle |\Psi_P^{ab}\rangle \tag{2.39}$$

where the contraction coefficients are given by

$$\langle \Psi_P^{ab} | \Psi_{kl,\omega}^{ab} \rangle = \frac{1}{2} \sum_R \alpha^R \langle \Psi_P^{ab} | \hat{E}_{ak,bl} + \omega \hat{E}_{bk,al} | \Psi_R \rangle \tag{2.40}$$

showing that these configurations are obtained by contracting different internal states.

The configurations in (2.37) can be orthogonalized using the overlap matrix $\mathbf{S}^{(\omega)}$ with its elements given by

$$S_{kl,ij}^{(\omega)} = \langle \Psi_0 | \hat{E}_{ki,lj} + \omega \hat{E}_{kj,li} | \Psi_0 \rangle \tag{2.41}$$

Using the popular procedure of Davidson[3,33–35], the Hamiltonian matrix can be diagonalized, which relies upon the formation of residual vectors that can then be used to generate an updated vector of CI expansion coefficients. The residual vectors are written as

$$\langle \Psi_{D,\omega}^{ab} | \hat{H} - E | \Psi \rangle = \left\{ \frac{1}{2} \left[\mathbf{G}^{D,\omega} + \omega (\mathbf{G}^{D,\omega})^\dagger \right] - E \mathbf{C}^{D,\omega} \right\}_{ab} \tag{2.42}$$

$$\langle \Psi_s^a | \hat{H} - E | \Psi \rangle = \left(\mathbf{g}^s - E \mathbf{C}^s \right)_a \tag{2.43}$$

$$\langle \Psi_s^a | \hat{H} - E | \Psi \rangle = g^I - E C^I \tag{2.44}$$

The explicit formulas for the quantities $\mathbf{G}^{D,\omega}$, $\mathbf{g}^s$ and g^I can be found in Refs.[22,33,36], which are calculated using an efficient direct CI method[33,37].

2.6 Coupled cluster theory

Since its introduction into quantum chemistry in the late 1960s by Cízek and Paldus[38–40], coupled cluster (CC) theory has been widely used for the approximate solution of the electronic Schrödinger equation and the prediction of molecular properties. The basic ansatz of CC theory is that the exact many-electron wavefunction may be generated by the operation of an exponential operator on a single determinant.

$$\Psi = e^{\hat{\mathbf{T}}} \Phi_0 \tag{2.45}$$

$\hat{}$ where Ψ is the exact wavefunction, $\hat{T}$ is an excitation operator, and Φ_0 is a single determinant wavefunction, usually the Hartree-Fock determinant. The excitation operator

can be written as a linear combination of single, double, triple, etc excitations, up to N fold excitations for an N electron system.

$$\hat{T} = \hat{T}_1 + \hat{T}_2 + \hat{T}_3 + \cdots + \hat{T}_N \tag{2.46}$$

where

$$\begin{aligned}
\hat{T}_1\Phi_0 &= \sum_{i}^{\text{occ}} \sum_{a}^{\text{vir}} t_i^a \Phi_i^a \\
\hat{T}_2\Phi_0 &= \sum_{i>j}^{\text{occ}} \sum_{a>b}^{\text{vir}} t_{ij}^{ab} \Phi_{ij}^{ab} \\
\hat{T}_3\Phi_0 &= \sum_{i>j>k}^{\text{occ}} \sum_{a>b>c}^{\text{vir}} t_{ijk}^{abc} \Phi_{ijk}^{abc}
\end{aligned} \tag{2.47}$$

etc. The coefficients, t_i^a, t_{ij}^{ab}, t_{ijk}^{abc},...of the various determinants are called the amplitudes. The exponential operator is defined by the usual expansion

$$e^{\hat{\mathbf{T}}} = \sum_{N=0}^{\infty} \frac{\hat{T}^N}{N!} = 1 + \hat{T} + \frac{1}{2}\hat{T}^2 + \frac{1}{6}\hat{T}^3 + \cdots \tag{2.48}$$

and $e^{\hat{T}}$ is expanded as in (2.45), we obtain

$$\begin{aligned}
\Psi \;=\; & \Phi_0 + \hat{T}_1\Phi_0 + \hat{T}_2\Phi_0 + \cdots \\
& + \frac{1}{2}\hat{T}_1^2\Phi_0 + \hat{T}_1\hat{T}_2\Phi_0 + \frac{1}{2}\hat{T}_2^2\Phi_0 + \cdots \\
& + \frac{1}{3!}\hat{T}_1^3\Phi_0 + \frac{1}{2}\hat{T}_1^2\hat{T}_2\Phi_0 + \frac{1}{2}\hat{T}_1\hat{T}_2^2\Phi_0 \frac{1}{3!}\hat{T}_3^3\Phi_0 + \cdots \\
& + \cdots
\end{aligned} \tag{2.49}$$

Note that the different $\hat{T}_N$ operators commute. Contributions to the wave function of the form $\hat{T}_N\Phi_0$ are called connected-cluster contributions while those involving products of cluster operators, such as $\frac{1}{2}\hat{T}_1^2\Phi_0$ or $\hat{T}_1\hat{T}_2\Phi_0$, are disconnected-cluster contributions. These disconnected-cluster terms, which are a direct consequence of the exponential form of the wave operator, are responsible for the extensivity of the CC wave function.

The most important disconnected-cluster contribution, at least in the Hartree-Fock case, is $\frac{1}{2}\hat{T}_1^2\Phi_0$ (though higher powers of $\hat{T}_2$ can become more important as the size of the

system increases). The connected $\hat{T}_3\Phi_0$ con- tribution is important particularly in systems with high electron densities, including molecules containing multiple bonds. Higher-order connected con- tributions ($\hat{T}_4\Phi_0$, $\hat{T}_5\Phi_0$, $\hat{T}_6\Phi_0$etc.) are of much less importance in general, though they can be important in special situations.

The simplest CC approach is that of coupled-cluster doubles (CCD)[41,42], in which $\hat{T}$ is truncated to

$$\hat{T}_{\mathrm{CCD}} = \hat{T}_2 \tag{2.50}$$

The CCD wave function includes all connected and disconnected clusters involving $\hat{T}_2$ only,

$$\Psi_{\mathrm{CCD}} = e^{\hat{T}_2}\Phi_0 = \Phi_0 + \hat{T}_2\Phi_0 + \frac{1}{2}\hat{T}_2^2\Phi_0 + \frac{1}{3!}\hat{T}_2^3\Phi_0 + \cdots \tag{2.51}$$

The most common extension of this model is coupled-cluster singles and doubles (CCSD)[41,43], defined by

$$\hat{T}_{\mathrm{CCSD}} = \hat{T}_1 + \hat{T}_2 \tag{2.52}$$

An excellent approximation to the exact wave function is usually provided by the (CCSDT)[44] model, which adds the triple-excitation clusters:

$$\hat{T}_{\mathrm{CCSDT}} = \hat{T}_1 + \hat{T}_2 + \hat{T}_3 \tag{2.53}$$

Owing to the high computational cost of including $\hat{T}_3$, however, this model is often approximated in a number of ways. Higher order hybrid methods such as CCSD(TQ)[45–47], where the connected quadruples contribution is estimated by fifth-order perturbation theory, are also possible, but they are again so demanding that they can only be used for small systems[45,46].

It is well known that the standard single reference CC methods, such as CCSD(T), fail when applied to biradicals, bond breaking, and other situations involving large nondynamic correlation effects[48–52]. A few attempts have been made in recent years to address this question. One of them are the methods belong to a family of completely renormalized (CR) CC approaches developed at Michigan State University[53–56] and incorporated in the GAMESS package[8]. In analogy to CCSD(T), all renormalized CC methods, including the CR-CCSD(T)[57–59], CR-CC(2,3)[54–56,60], CR-CCSD(TQ)[57–59], CR-CC(2,3)+Q[61–64]

approaches, are based on an idea of adding non-iterative a posteriori corrections due to higher-than-doubly excited cluster to CCSD energy [triples in the CR-CCSD(T) and CR-CC(2,3) cases, and triples and quadruples in the CR-CCSD(TQ) and CR-CC(2,3)+Q cases]. One of the advantages of the renormalized CC approaches is their ability to improve the poor CCSD(T) results in multi-reference situations involving bond breaking and biradicals, without making the calculations considerably more expensive and without using the multideterminantal reference wave functions[53,54,65–77]. Indeed, the most expensive steps of the CR-CCSD(T) and CR-CC(2,3) approaches, in which one corrects the CCSD energy for the effects of triply excited clusters, scale as $n_o^2 n_u^4$ in the iterative CCSD part and $2n_o^3 n_u^4$ in the non-iterative part related to the calculations of the relevant triples corrections. For comparison, the computer costs of determining the triples correction of CCSD(T) scale as $n_o^3 n_u^4$. The CR-CCSD(TQ) and CR-CC(2,3)+Q methods are more expensive, since, in addition to the $n_o^2 n_u^4$ steps of CCSD and $2n_o^3 n_u^4$ steps of the triples corrections, one needs the $2n_o^2 n_u^5$ steps to calculate the corrections due to quadruples, but even the most demanding $2n_o^2 n_u^5$ steps of CR-CCSD(TQ) and CR-CC(2,3)+Q are much less expensive than the iterative steps related to the full inclusion of triples and quadruples($n_o^3 n_u^5$and $n_o^4 n_u^6$, respectively).

2.7 Basis sets

As discussed earlier, linear combinations of atomic orbitals (LCAO-MO) were introduced as basis functions for the spatial part of the molecular orbitals in Slater determinats.

$$\psi_i = \sum_{\mu=1}^{n} c_{\mu i} \chi_\mu \tag{2.54}$$

where the ψ_i is the ith molecular orbital, $c_{\mu i}$ are the coefficients of the linear combination, χ_μ is the μth atomic basis set orbital, and n is the total number of the atomic orbitals. One of the approximations inherent in all ab initio methods is the introduction of a basis set for the atomic orbitals. If the basis is complete, it is not an approximation to expand an unknown function (such as an atomic orbital) in a set of known functions. However, a complete basis means that we must use an infinite number of functions. When a finite

basis is used, only the components of the atomic orbital along those coordinate axes corresponding to the selected basis can be represented. Therefore, a smaller basis corresponds to a poorer representation of the molecular orbitals. The type of basis functions used also influences the accuracy. The better a single basis function is able to reproduce the unknown function, the fewer basis functions are necessary for achieving a given level of accuracy. Initially, these atomic orbitals were typically Slater orbitals, which corresponded to a set of functions which decayed exponentially with distance from the nuclei. Later, it was realized that these Slater-type orbitals (STOs)[78] could in turn be approximated as linear combinations of Gaussian orbitals instead. Today, there are hundreds of basis sets composed of Gaussian-type orbitals (GTOs)[79,80].

In order to speed up molecular integral evaluation, GTOs were first proposed by Boys[79] in 1950, which can be written in terms of polar or Cartesian coordinates as

$$\begin{aligned} \chi^{\zeta}_{nlm}(r,\theta,\phi) &= N r^{2n-2-l} e^{-\zeta r^2} Y^m_l(\theta,\phi) \\ \chi^{\zeta}_{l_x l_y l_z}(r,\theta,\phi) &= N x^{l_x} y^{l_y} z^{l_z} e^{-\zeta r^2} \end{aligned} \tag{2.55}$$

The sum of the exponents of the Cartesian coordinates, $l = l_x + l_y + l_z$, is used to mark functions as s-type (l=0), p-type (l=1), d-type (l=2), and so on. The main difference to the STOs is that the variable r in the exponential function is squared. A number of Gaussian primitives are usually contracted to a so called contracted Gaussian type orbital (CGTO)[81,82], which take the following formation

$$\chi_\nu = \sum_{\nu=1}^{M} d_{\mu\nu} g_\nu(\alpha_\nu) \tag{2.56}$$

where M is the length of the contraction, the g_ν's are primitive Gaussians functions, $d_{\mu\nu}$ and is contraction coefficients which can be determined by least-square fits to accurate atomic orbital or by minimization of the total HF energy. A CGTO is a linear combination of Gaussian primitives. The number of CGTOs used to represent a single Slater type orbital is a measure of the quality of the basis.

2.7.1 Classification of basis sets

Having decide on the type of function (STO or GTO), the most important factor is the number of functions to be used. To contain all the electrons in a neutral atom, the smallest number of functions possible is called *minimum basis set*. This means a single For hydrogen (and helium). For the first row elements of the periodic table, it requires two s-functions ($1s, 2s$) and one set of p-functions ($2p_x, 2p_y, 2p_z$). Lithium and beryllium only require two s-functions, but usually also added a set of p-functions. For the second row elements, three s-functions ($1s, 2s$ and $3s$) and two sets of p-functions ($2p$ and $3p$) are employed.

The next improvement of the basis set is a doubling of all basis function to produce a *Double zeta* (DZ) type basis. The term zeta stems from the fact that the exponent of STO basis functions is often denoted by the Greek letter ξ. For the elements on the first row, a DZ basis set employs two s-functions for hydrogen ($1s$ and $1s'$), four s and two p-functions, and so on. Doubling the number of basis functions thus allows for a much better description of the fact that the electrons distribution is different in different directions.

One can also go further to *Triple Zeta* (TZ), which contains three times as many functions as the minimum basis, also *Quadruple Zeta* (QZ), *Quintuple Zeta* (5Z) and so on. However, large basis sets are often given explicitly in terms of the number of basis functions of each type. So far, only the number of s-functions and p-functions for each atom has been discussed. In most cases, higher angular momentum functions are also important, and theses are denoted as *polarization functions*. If methods including electron correlation are used, higher angular momentum functions are essential. Polarization functions are added to the chosen *sp*-basis. Adding a single set of polarization functions (p-functions on hydrogens and d-functions on heavy atoms) to the DZ basis forms a *Double Zeta plus Polarization (DZP)* type basis. Similar, to the *sp*-basis sets, multiple sets of polarization functions with different exponents maybe added. If two sets of polarization functions are added to a TZ *sp*-basis, a *Triple Zeta plus Polarization (TZ2P)* type basis is obtained. For larger basis sets with many polarization functions the explicit composition in terms

of number and types of functions is usually given.

Usually, it takes too much effort to calculate a DZ for every orbital. Instead, many scientists simplify matters by calculating a DZ only for the valence orbital. Since the inner-shell electrons are not as vital to the calculation, they are described with a single Slater Orbital. This method is called a *split-valence basis set*. The $n-ij$G or $n-ijk$G split-valence basis sets are due to Pople and co-workers[83–85], where n is the number of primitives summed to describe the inner shells, ij or ijk is the number of primitives for contractions in the valence shell. In the $6-31$G basis, for example, the core orbitals are described by a contraction of six GTOs, whereas the inner part of the valence orbitals is a contraction of three GTOs and the outer part of the valence is represented by one GTOs. Including *polarization functions* give more angular freedom so that the basis is able to represent bond angles more accurately, especially in strained ring molecules. For example, $6-31$G** basis set, the first asterisk indicate the addition of d functions on the non-hydrogen atoms and the second asterisk a p function on hydrogen atom[86]. Another type of functions can be added to the basis for a good description of the wavefunction far from the nucleus are the *diffuse functions*, which are additional GTOs with small exponents. The diffuse functions are usually indicated with a notation "+". For example, in the 6-31++G basis set, the "++" means the addition of a set of s and p function to the heavy atoms, while an additional s diffuse GTO for hydrogen.

For correlated calculations, the basis set requirements are different and more demanding since we must then describe the polarizations of the charge distribution and also provide an orbital space suitable for recovering correlation effects. For this purpose, the *correlation consistent basis sets* are very suited, which is usually denoted as cc-pVXZ[87,88]. The "cc" denotes that this is a correlation-consistent basis, meaning that the functions were optimized for best performance with correlated calculations. The "p" denotes that polarization functions are included on all atoms. The"VXZ" stands for valence with the cardinal number $X = D, T, Q, \ldots$ indicate double-, triple- or quadruple-zeta respectively. The inclusion of diffuse functions, which can improve the flexibility in the outer valence region, leads to the augmented correlation-consistent basis sets aug-cc-pVXZ[87,88], where one set of diffuse functions is added in cc-pVXZ basis.

2.7.2 Basis set superposition error

In quantum chemistry, One problem associated with all finite basis set calculations, which may lead to an important phenomenon referred as the basis-set superposition error (BSSE)[89,90]. The interaction energy of a complex AB can be defined as the difference

$$\Delta E_{int}(r_{AB}) = E_{AB}^{AB}(r_{AB}) - E_A^A - E_B^B \tag{2.57}$$

where, $\Delta E_{int}(r_{AB})$ denotes the interaction energy of the system. $E_{AB}^{AB}(r_{AB})$ represents the energy of the bimolecular complex AB evaluated in the dimer basis (the union of the basis sets on A and B), computed at the geometry of the dimer. Likewise, monomers A and B are each evaluated at their own geometries in their own basis sets. The energy of the separate atoms does not depend on the interatomic distance, while the basis set superposition error varies with the interatomic distance. The interaction energy in Eq.(2.57) is in need for a correction on the BSSE.

Boys and Bernardi[91] introduced the counterpoise correction to correct for the BSSE. In the counterpoise correction, the artificial stabilization is countered by letting the separate atoms improve their basis sets by borrowing functions of an empty basis set. To realize such an empty basis set, a ghost atom is used. The ghost atom has the basis set of the according atom, but no electrons to fill it. Performing this procedure for both atoms on the grid will correct for the BSSE. Hence, the interaction energy with counterpoise correction is

$$\Delta E_{int}^{CP}(r_{AB}) = E_{AB}^{AB}(r_{AB}) - E_A^{AB}(r_{AB}) - E_B^{AB}(r_{AB}) \tag{2.58}$$

Note that in Eq.(2.58) the energy of the separate atoms depend on a internuclear distance (the distance between the atom and the ghost atom).

On the other hand, the BSSE can be corrected by scaling[92] or extrapolating[93–96] the *ab initio* energies to the complete basis set limit as discussed in the next section.

2.8 Semiempirical correction of *ab initio* energies

By truncating the atomic basis set we introduce some errors like the BSSE previously discussed, however, the truncate CI wave function lacks of size-extensivity due to does

not include as much of the *dynamical* or *external* electron correlation effects. A method was proposed by Brown and Truhlar[97], said to be size extensive if the energy calculated thereby scales linearly with the number of electrons, so called Scaling external correlation (SEC) method. The SEC method applies to the MRCI energy. In such approach the *non-dynamical* (*static*) or *internal* correlation energy is obtained by an MCSCF calculation and the part of external valence correlation energy by an MRCISD calculation based on the MCSCF wave functions as references. Then, it is given by it is assumed that the MRCISD includes a constant (*geometry independent*) fraction F of the external valence correlation energy, which can be extrapolated with the formula

$$E_{\mathrm{SEC}}(\mathbf{R}) = E_{\mathrm{MCSCF}}(\mathbf{R}) + \frac{E_{\mathrm{MRCISD}}(\mathbf{R}) - E_{\mathrm{MCSCF}}(\mathbf{R})}{F} \tag{2.59}$$

where $E_{\mathrm{SEC}}(\mathbf{R})$ denotes the SEC energy, and F is assumed to be independent of geometry, can be chosen to reproduce a bond energy for diatomics, and to reproduce more than one bond energy in an average sense[97] for systems with more atoms. Hence, F can be estimated by calculating the energy to break a bond and comparing it to experiment

$$F = \frac{E_{\mathrm{MRCISD}} - E_{\mathrm{MCSCF}}}{E_{\mathrm{exp}} - E_{\mathrm{MCSCF}}} \tag{2.60}$$

This method has been reformulated by Varandas[98], who suggested a generalization of the SEC method by noticing the conceptual relationship between it and the double many-body expansion (DMBE) method[99], then denoted as DMBE-SEC[98]. In the DMBE scheme each n-body potential energy term is partitioned into extended-Hartree-Fock (internal correlation) and dynamic correlation (external correlation) parts. The total interaction energy, relative to infinitely separated atoms in the appropriate electronic states, was written in the form

$$V(\mathbf{R}) = V_{\mathrm{MCSCF}}(\mathbf{R}) + V_{\mathrm{SEC}}(\mathbf{R}) \tag{2.61}$$

where

$$V_{\mathrm{MCSCF}}(\mathbf{R}) = \sum V^{(2)}_{\mathrm{AB,MCSCF}}(R_{\mathrm{AB}}) + \sum V^{(3)}_{\mathrm{ABC,MCSCF}}(R_{\mathrm{AB}}, R_{\mathrm{BC}}, R_{\mathrm{AC}}) + \ldots \tag{2.62}$$

$$V_{\mathrm{SEC}}(\mathbf{R}) = \sum V^{(2)}_{\mathrm{AB,SEC}}(R_{\mathrm{AB}}) + \sum V^{(3)}_{\mathrm{ABC,SEC}}(R_{\mathrm{AB}}, R_{\mathrm{BC}}, R_{\mathrm{AC}}) + \ldots \tag{2.63}$$

and the summations run over the subcluster of atoms (dimers, trimers, ...) which compose the molecule.

The scaled external correlation energy component for the n-th terms is given by

$$V^{(n)}_{\mathrm{AB...,SEC}} = \frac{V^{(n)}_{\mathrm{AB...,MRCISD}} - V^{(n)}_{\mathrm{AB...,MCSCF}}}{\mathcal{F}^{(n)}_{\mathrm{AB}}} \tag{2.64}$$

where $\mathcal{F}^{(n)}_{\mathrm{AB...}}$ is the n-body geometry independent scaling factor.

As in the original SEC method, optimal values for two-body factors $\mathcal{F}^{(2)}_{\mathrm{AB}}$ are chosen to reproduce experimental dissociation energies, a criterion which may be adopted for higher-order terms if accurate dissociation energies exist for the relevance subsystems[98]. For the triatomic case a good guess for $\mathcal{F}^{(3)}_{\mathrm{ABC}}$ can be the average of the two-body factors

$$\mathcal{F}^{(3)}_{\mathrm{ABC}} = \frac{1}{3}\left[\mathcal{F}^{(2)}_{\mathrm{AB}} + \mathcal{F}^{(2)}_{\mathrm{BC}} + \mathcal{F}^{(2)}_{\mathrm{AC}}\right] \tag{2.65}$$

Improved agreement with experiment and best theoretical estimates, is obtained when *ab initio* energies are corrected with the DMBE–SEC method. Particularly important, for dynamics calculations, are the correct exothermicities for all arrangement channels, exhibited by the DMBE–SEC potential surfaces[98].

2.9 Analytical representation of potential energy surface

Once enough information has been gathered to map the potential energy surface, the major problem is represent it in a realistic global analytical form. A function that match the ab initio data within the chemical accuracy provide a visualization of topographical surface features, that may not be evident from a coarse-grained ab initio study. Moreover, as theoretical counterpart of experimental reaction dynamics, smooth and well behaved potential function can be used in dynamical studies. It is not a easy task choosing the suitable function to fit PESs. Any suitable function must gather several important characteristics: smoothly connect the asymptotic and interaction regions of the configuration space; have the correct symmetry properties of the molecule; represent the true potential

energy accurately in regions of the configuration space for which experimental or theoretical data are available and it even must predict those parts of the interaction region for which no experimental or theoretical data are available. Many other criteria, that a successful representation of a PES must satisfy, can be found in the literature [100–102].

For more than half a century, many methods have been developed to construct analytical potential energy surfaces. Among the most popular approaches can be mentioned the semiempirical London-Eyring-Polanyi-Sato (LEPS) [103–105] and diatom-in-molecules (DIM) [106–108] methods, which use theoretical and experimental information to fit a functional form derived from simple molecular orbital theory. A more general approach is the many-body expansion (MBE) method developed by Murrel and co-workers [109–111], which proposed to describe the total interaction of the polyatomic system by adding all the many-body interactions of each fragment. The PESs discussed in the present thesis are represented using an improved version of MBE due to Varandas [92,99,112,113]: the double many-body expansion (DMBE) method, which consists in partitioning each n-body contribution in short-range and long-rang parts. The more detailed discussion of MBE and DMBE methods is given in the following sections.

2.9.1 The many-body expansion method

For an N-atomic system, a single-valued PES in the many-body expansion (MBE) method, can be represented as a many-body expansion

$$V(\mathbf{R}^N) = \sum_{n=1}^{N} \sum_{i=1}^{K} V_i^{(n)}(\mathbf{R}^n) \tag{2.66}$$

where $\mathbf{R}^N$ is a collective variable which represents the $N(N-1)/2$ internuclear distances, $\mathbf{R}^n$ is a subset $\mathbf{R}^N$ containing only $n(n-1)/2$ distances and $V_i^{(n)}(\mathbf{R}^n)$ represents an n-body term. There are $N!/n!(N-n)!$ n-body terms in an N-atom system.

To the expansion (2.67) is imposed the boundary condition that each n-body term vanish when one of the atoms, involved in the corresponding molecular cluster, is adiabatically removed to infinity. A simple form which satisfy such requirement is written

as

$$V^{(n)}(\mathbf{R}) = P(\mathbf{R}^n)T(\mathbf{R}^n) \tag{2.67}$$

where $P(\mathbf{R}^n)$ is a polynomial in the internuclear distances and $T(\mathbf{R}^n)$ is a range function which tend to zero when one of the internuclear coordinates in the n-body species tends to infinity[111].

The potential written in this form is guaranteed to satisfy all dissociation limits, which is an essential requirement for molecular dynamics studies. Moreover, in order to study the potentials of all the fragments, the MBE suggests an strategy for building up a polyatomic potential. So that, even when the many-body expansion is not rapidly convergent, nor are the terms functionally simple, the last two mentioned built-in properties have advantages first of all if the intended use of the potential is reactional dynamic studies.

2.9.2 The double many-body expansion method

Varandas[92,99,112,113] extended the many-body expansion to the double many-body expansion (DMBE) in which each many-body term is splitted into two parts: one accounting for the long range or dynamical correlation (dc) energy and the other describing the short range or extended-Hartree-Fock (EHF) energies.

$$V(R^N) = \sum_{n=1}^{N} \sum_{R^n \subset R^N} \left[V_{\mathrm{EHF}}^{(n)}(R^n) + V_{\mathrm{dc}}^{n}(R^n) \right] \tag{2.68}$$

where, R^n denotes any set of $n(n-1)/2$ coordinates of the fragment containing n atoms, which is a subset of $R^N \equiv [R_1, R_2, \ldots R_{N(N-1)/2}]$, and last sum is carried out over all such subsets. This DMBE method advocate for a reliable description of the potential surface from short to large interatomic separations, by including, through a semiempirical potential, V_{dc}^n, the dynamical correlation energy, in principle discarded in an uncorrelated electronic structure calculation[99].

Varandas and coworkers[99,112,114–117], to reproduce the proper anisotropy and asymptotic behavior of the PES for the entire configuration space, proposed general expressions for the n-body dynamic correlation energy term. The three-body dc energy assumes the

usual form of a summation in inverse powers of the fragment separation distances[118]

$$V_{dc}^{(3)} = -\sum_i \sum_n f_i(\mathbf{R}) \chi_n(r_i) C_n^{(i)}(R_i, \theta_i) r_i^{-n} \tag{2.69}$$

where i labels the I-JK channel associated with the center of mass separation and (r_i,θ_i,R_i) are the Jacobi coordinates corresponding to the specific $\mathbf{R} = (R_1, R_2, R_3)$ geometry of the triatomic system (see Figure 1 of Ref. 92). Moreover $f_i(\mathbf{R}) = \frac{1}{2}\{1 - \tanh[\xi(\eta R_i - R_j - R_k)]\}$ is a convenient switching function. Following recent work on NH_2[119], we have fixed $\eta = 6$ and $\xi = 1.0\, a_0^{-1}$. $\chi_n(r_i)$ is the damping function, which takes the form employed elsewhere[118,119]. In additional the value of ρ has been optimized by a trial-and-error to get a good asymptotic behaviour of the dynamical correlation term, leading to $\rho = 16.125 a_0$ The atom-diatom dispersion coefficients in Eq. (2.69), which are given by

$$C_n^{(i)}(R_i) = \sum_L C_n^L(R) P_L(cos\theta_i) \tag{2.70}$$

Where $P_L(cos\theta_i)$ denotes the Lth Legendre polynomial. The expansion in Eq. (2.70) has been truncated by considering of only the coefficients C_6^0, C_6^2, C_8^0, C_8^2, C_8^4 and C_{10}^0; all other coefficients we have employed the generalized Slater-Kirkwood formula[120] and bipolar polarizabilities calculated in the present work at MRCI/V$\mathcal{Q}$Z level. As usual, the atom-diatom dispersion coefficients so calculated for a set of internuclear distance have then been fitted to the form

$$C_n^{L,A-BC}(R) = C_n^{L,AB} + C_n^{L,AC} + D_M \left(1 + \sum_{i=1}^{3} a_i r^i\right) \exp\left(-\sum_{i=1}^{3} b_i r^i\right) \tag{2.71}$$

where $C_n^{L,AB}$, for $L = 0$, are the corresponding diatom dispersion coefficients. All parameters and coefficients in Eq. (2.71) have been explained elsewhere[121]. An important result refers to the introduction of an universal charge-overlap damping function to account for the damping of the dispersion coefficients for intermediate and small interatomic separations[114].

Within the DMBE framework, the extended Hartree-Fock approximate correlation energy for two- and three-body interactions (EHFACE2 and EHFACE3) models have been proposed[115], from simple, yet reliable, physical motivated forms. For two-body

potentials, a screened extended-Rydberg form (with an extra R^{-1} term) can be adapted to represent the global short-range energy, which reproduces the exact $Z_A Z_B/R$ behavior at the united atom limit (EHFACE2U model[117]). In turn, the three-body EHF potential is represented by the following three-body distributed-polynomial form[122]

$$V_{\mathrm{EHF}}^{(3)}(\mathbf{R}) = \sum_{i=1}^{m} P^{(i)}(Q_1, Q_2, Q_3) \prod_{j=1}^{3} \left\{ 1 - \tanh\left[\gamma_j^{(i)} \left(R_j - R_j^{i,ref} \right) \right] \right\} \tag{2.72}$$

where $P^{(i)}(Q_1, Q_2, Q_3)$ are polynomials in the symmetric coordinates $\{Q_k\}$, expressed as combinations of the internuclear coordinates $\{R_j\}$, which transform as irreducible representations of the permutation group of the molecule[111]. In turn, $R_j^{i,ref}$ represents a convenient reference geometry to which the i-th component of (2.72) is referred to[122]. If extensive *ab initio* data is available, the optimized coefficients for the two-body and three-body terms can be obtained using linear or non-linear least-square fits[123].

The DMBE method has given some of the most accurate currently available potential energy surface for well known prototype systems $H_3(^2A')$[124], $Li_3(^2A')$[125], $FH_2(^2A')$[126], $HO_2(^2A'')$[127,128]. Examples of the DMBE method applied to such cases can be also found in Refs.119, 129–131.

2.9.3 Approximate single-sheeted representation

Chemical reaction are often visualized as proceeding on a single-sheeted potential energy surface (PES) or within a particular electronic state. This view of chemical reaction arises from the Born-Oppenheimer (BO) approximation, in which the motion of the electrons and the nuclei are assumed to be decoupled because of the great difference in the masses of the electrons and the nuclei. Using this assumption it is then possible to undertake dynamic calculations to study the chemical reactions[132–134]. The BO approximation breaks down when the eigenfunctions of the electronic Hamiltonian become degenerate or nearly degenerate, or in the case of a reaction can be thought of as taking place two or more PESs which are coupled. An exact treatment demands a multi-sheeted representation of the PES, while two or more potential energy surfaces crossing. Such representation of the potential can be expressed as the lowest eigenvalues of a square matrix of order equal

to the number of states involved[135]. Thus, the elements of the diabatic potential matrix can be written as many-body expansions or double-many body expansions involving the appropriate electronic states of the fragments.

However, for dynamical purposes an approximated single-sheeted representation can provide a good analytical form for many situations. For example, if a crossing between states is present, it can be avoided in such a way that the potential function smooths the region around the intersection point. If the crossing is located well above the dissociation channels or the stationary points of the molecule, it is expected to have a minor influence in the dynamics of the system. In the present work, the DMBE potential energy surfaces for the systems $N_2O\,(^1A')$ was calibrated following this procedure. The obtained DMBE-PES for N_2O was employed to further dynamics calculations for the reaction $N\,(^2D) + NO\,(X\,^2\Pi) \rightarrow N_2\left(X\,^1\Sigma_g^+\right) + O\,(^1D)$ showing the reliability of the approximated single-sheeted form.

It is unavoidable to use switching functions, in order to obtain an approximate representation of a multi-sheeted PES by a single-sheeted form. Such a procedure has been first proposed by Murrell and Carter[136], who applied it in the construction of an approximate PES for the ground-state H_2O. These authors introduced a switching one-body term for oxygen, allowing that in the PES the atomic state $O\,(^1D)$ is connected for the channel $H_2\left(X^1\Sigma_g^+\right) + O\,(^1D)$ and disconnected for the other dissociation limits. A smooth description of the PES which accounted for such a behavior of the oxygen atomic state, is warrant employing a switching function in the form

$$f\,(x) = \frac{1}{2}\left[1 - \tanh\left(\alpha x\right)\right] \tag{2.73}$$

which has the limits unity as $x \rightarrow -\infty$ and zero as $x \rightarrow +\infty$.

By choosing the variable x as

$$x = n\rho_3 - \rho_1 - \rho_2 \tag{2.74}$$

where $\rho_i = R_i - R_i^0$ are the displacements of the internuclear distances from a reference structure (R_3 the H–H distance, and R_1, R_2 the OH distance), then it is easy to see that x takes the limit $-\infty$ for dissociation into $H_2 + O$ and $+\infty$ for dissociation to $OH + H$ provided $n \geq 2$.

Although the Murrell-Carter switching function forms can ensure the correct asymptotic limit, they failed to warrant a unique value for the energy at the geometries of the system where three atoms are far away from each other. In fact, even for large H–H separation, the function (2.73) switches from 0 to 1 when oxygen moves far away from the diatomic. To correct such unphysical behavior, Varandas and Poveda[119] have suggested an improved switching function in their work on DMBE PES of $NH_2(^2A'')$. The same functional form is employed in the construction of an approximated single-valued DMBE PES for $N_2O\,(X\,^1A')$, which can be written as

$$V(\mathbf{R}) = V^{(1)}_{\mathrm{O}(^1D)} f_1(\mathbf{R}) + V^{(1)}_{\mathrm{N}_A(^2D)} f_2(\mathbf{R}) + V^{(1)}_{\mathrm{N}_B(^2D)} f_3(\mathbf{R}) + \sum_{i=1}^{3} \left[V^{(2)}_{\mathrm{EHF}}(R_i) + V^{(2)}_{\mathrm{dc}}(R_i) \right] + V^{(3)}_{\mathrm{EHF}}(\mathbf{R}) + V^{(3)}_{\mathrm{dc}}(\mathbf{R}) \tag{2.75}$$

In the one body term $V^{(1)}_{\mathrm{O}(^1D)}$ represents the energy difference between the ^1D and ^3P states of atomic oxygen, $f_1(\mathbf{R})$ is the switching function used to warrant the correct behaviour at the $N_2(X\,^1\Sigma_g^+) + O(^1D)$ dissociation limits, while $V^{(1)}_{\mathrm{N}_A(^2D)}$ and $V^{(1)}_{\mathrm{N}_B(^2D)}$ represent the energy difference between the $N(^2D)$ and $N(^4S)$ states: $V^{(1)}_{\mathrm{N}_A(^2D)}$. $f_2(\mathbf{R})$ and $f_3(\mathbf{R})$ are the switching functions used to warrant the correct behaviour at the $NO(X\,^2\Pi) + N(^2D)$ dissociation limits. The two-body and three-body energy terms are split into two contributions: the extended Hartree-Fock (EHF) and dynamical correlation (dc) energies.

2.10 Properties of potential energy functions

Once a potential energy function (PES) has been properly represented, it must be analyzed to determine information about the chemical system. The PES is the most complete description of all the conformers, isomers, and energetically accessible motions of a system[13,111]. Minima on this surface correspond to optimized geometries, any movement away from a minimum gives a configuration with higher energy. The lowest-energy minimum is called the global minimum. There can be many local minima, such as higher-energy conformers or isomers. The transition structure between the reactants and products of a reaction, or the highest energy configuration between them, is a saddle point on

this surface. A PES can be used to find both saddle points and reaction coordinates, and, as done in this work, to subsequently study reaction dynamics. The vibrational properties of the molecular system can also be obtained from the PES[13].

Let us represent the potential energy function as $f(x))$ depending on a set of variables $x = (x_1, x_2, ..., x_N)$. Optimization is a general term for finding stationary points of a function i.e. points where all the first derivatives are zero. Stationary points condition can be written in terms of the gradient g, a vector formed by the first order derivatives of f , and the Hessian H, a symmetric matrix with the second derivatives as elements. By means of orthogonal transformations[137] the matrix H can be diagonalized, becoming in H' . When all the diagonal elements of H' are positive, the stationary point correspond to a minimum configuration, i.e. if:

$$g(x_0) = 0,\ H'_{ii}(x_0) > 0 \tag{2.76}$$

at given x_0 the function will reach a local minimum. If the function value at this point is the smallest one of all the minima, then x_0 stands for the global minimum configuration. When one of diagonal elements of H' is negative, then the configuration x_0 correspond to a saddle point.

Hessian, once diagonalized gives not only a condition to define whether a configuration is a minimum or a saddle point, but also the normal modes frequencies, whose values are proportional to the square root of the diagonal elements. Therefore, a saddle point will be an stationary point with an imaginary frequency. Such an imaginary frequency will characterize the coordinate connecting the two minima. Stationary points also exist which have more than one imaginary frequency. However, in general these do not have any special meaning.

To find those configurations corresponding to minima and saddle points, optimization techniques are required[138]. In the optimization of the PES presented in this thesis a package[139] available at the Coimbra Theoretical & Computational Chemistry group was used. This code uses a mixture of optimization methods, and it has been specifically designed for potential energy functions of molecular systems, once the function has been given.

The dissociation products of a polyatomic system correspond to regions at infinity where the potential energy surface is flat in one or more dimensions. Thus, gradient of the PES is zero. The asymptotic regions can be referred as valleys. The slope of the valley gradually changes when the atoms approach each other. If they moves towards a saddle point the slope will be positive while a negative value indicate the approximation towards a minimum.

The term path is used to name the curve (hyper-curve, to denote its multidimensional character) defined by the energy function where the coordinates change from one configuration to another. Thus a reaction path is a path leading from the reactants valley the to products configuration. A minimum-energy reaction path follows the optimum way, it means, of all the possible paths, that corresponding to the steepest descent from saddle point to both products and reactants limits[140]. The saddle point is the maximum energy configuration in the minimum-energy reaction path.

Due to the current level of constantly increasing computing power, construction of potential energy surfaces might produce a feeling of an obsolete idea. An strong temptation comes from the desire to carry direct or on the fly dynamics i.e. obtain *ab initio* energies, gradients and force constants once required for a given configuration of the trajectory[141,142], therefore, with no need of a function representation. Besides, by using large computational facilities to think in a very dense grid of *ab initio* points instead of a continuous function could be the trend[143]. However, it should be kept in mind that *ab initio* calculations are not the exact solution of the Schrödringer equation neither within the Born-Oppenheimer approximation. Actually, as was mentioned in previous sections, a large number of approximations was used for such a goal. Thus, even at the state of the art level of theory one might eventually get inappropriate solutions for the real problem. On the other hand, representations of PESs through functions provides a global view[29]; besides, once the selected method to represent the interaction comes with real physical meaning, it is possible to guarantee appropriate behavior in the range or regions were *ab initio* calculations could fail[112]. Furthermore, and as final words on this topic, a function representing a PES can be further corrected with experimental evidences[144] and, as in DMBE method, such a function may be used in the representation of larger

systems. While, for example, in one on-the-fly-trajectory, once it is finished the calculated electronic energies can hardly be used for other studies.

Bibliography

[1] T. Helgaker, P. Jørgensen, and J. Olsen, *Molecular Electronic-Structure Theory* (Wiley, Chichester, 2000).

[2] J. Almlöf, *in Modern Electronic Structure Theory* (World Scientific, Singapore, 1995).

[3] A. C. Hurley, *Introduction to the Electron Theory of Small Molecules* (Academic Press: London, 1976).

[4] M. Born and J. R. Oppenheimer, Ann. Phys. **84**, 457 (1927).

[5] C. C. J. Roothaan, Rev. Mod. Phys. **23**, 69 (1951).

[6] J. A. Pople and D. L. Beveridge, *Approximate Molecular Orbital Theory* (McGraw-Hill, New York, 1970).

[7] M. J. Frisch, G. W. Trucks, H. B. Schlegel, G. E. Scuseria, M. A. Robb, J. R. Cheeseman, J. A. Montgomery, Jr., T. Vreven, K. N. Kudin, J. C. Burant, J. M. Millam, S. S. Iyengar, J. Tomasi, V. Barone, B. Mennucci, M. Cossi, G. Scalmani, N. Rega, G. A. Petersson, H. Nakatsuji, M. Hada, M. Ehara, K. Toyota, R. Fukuda, J. Hasegawa, M. Ishida, T. Nakajima, Y. Honda, O. Kitao, H. Nakai, M. Klene, X. Li, J. E. Knox, H. P. Hratchian, J. B. Cross, V. Bakken, C. Adamo, J. Jaramillo, R. Gomperts, R. E. Stratmann, O. Yazyev, A. J. Austin, R. Cammi, C. Pomelli, J. W. Ochterski, P. Y. Ayala, K. Morokuma, G. A. Voth, P. Salvador, J. J. Dannenberg, V. G. Zakrzewski, S. Dapprich, A. D. Daniels, M. C. Strain, O. Farkas, D. K. Malick, A. D. Rabuck, K. Raghavachari, J. B. Foresman, J. V. Ortiz, Q. Cui, A. G.

Baboul, S. Clifford, J. Cioslowski, B. B. Stefanov, G. Liu, A. Liashenko, P. Piskorz, I. Komaromi, R. L. Martin, D. J. Fox, T. Keith, M. A. Al-Laham, C. Y. Peng, A. Nanayakkara, M. Challacombe, P. M. W. Gill, B. Johnson, W. Chen, M. W. Wong, C. Gonzalez, and J. A. Pople, Gaussian 03, Revision C.02, Gaussian, Inc., Wallingford, CT, 2004.

[8] M. W. Schmidt, K. K. Baldridge, J. A. Boats, S. T. Elbert, M. S. Gorgon, J. H. Jensen, S. Koseki, N. Matsunaga, K. A. Nguyen, S. Su, T. L. Windus, M. Dupuis, and J. Montgomery, Jr., J. Comput. Chem. **14**, 1347 (1993).

[9] H.-J. Werner and P. J. Knowles, MOLPRO is a package of *ab initio* programs written by H.-J. Werner, P. J. Knowles, with contributions from R. D. Amos, A. Bernhardsson, A. Berning, P. Celani, D. L. Cooper, M. J. O. Deegan, A. J. Dobbyn, F. Eckert, C. Hampel, G. Hetzer, T. Korona, R. Lindh, W. Lloyd, S. J. McNicholas, F. R. Manby, W. Meyer, M. E. Mura, A. Nicklass, P. Palmieri, R. Pitzer, G. Rauhut, M. Schtz, H. Stoll, A. J. Stone, R. Tarroni, and T. Thorsteinsson, (2000).

[10] J. C. Slater, Phys. Rev. **34**, 1293 (1929).

[11] C. D. Sherrill and H. F. Schaefer, Adv. Quant. Chem. **34**, 143 (1999).

[12] J. L. Jackon and R. E. Wyatt, Chem. Phys. Lett **4**, 643 (1970).

[13] F. Jensen, *Introduction to Computational Chemistry* (John Wiley & Sons, 2007).

[14] G. Jolicard, C. Leforestier, and E. J. Austin, J. Chem. Phys. **88**, 1026 (1987).

[15] A. C. Wahl and G. Das, *Methods of Electronic Structure Theory* (Plenum Press, New York, 1977).

[16] B. O. Roos, in *Ab Initio Methods in Quantum Chemistry*, edited by K. Lawley (Wiley, New York, 1987), p. 399.

[17] B. O. Roos, P. R. Taylor, and P. E. M. Siegbahn, Chem. Phys. **48**, 157 (1980).

[18] J. Frenkel, *"Wave Mechanics" vol II, Advanced General Theory* (Dover, 1950).

[19] H.-J. Werner and P. J. Knowles, J. Chem. Phys. **89**, 5803 (1988).

[20] H.-J. Werner, in *Ab Initio Methods in Quantum Chemistry*, edited by K. Lawley (Wiley, New York, 1987), p. 1.

[21] P. E. M. Siegbahn, Int. J. Quantum Chem. **23**, 1869 (1983).

[22] P. E. M. Siegbahn, Int. J. Quantum. Chem. **18**, 1229 (1980).

[23] J. H. van Lenthe, J. G. C. M. van Duijneveldt-van de Rijdt, and F. B. van Duijneveldt, in *Ab Initio Methods in Quantum Chemistry*, edited by K. Lawley (Wiley, New York, 1987), p. 521.

[24] H. Szichman and M. Baer, Chem. Phys. Lett. **242**, 285 (1995).

[25] N. Moiseyev and P. R. Certain, Mol. Phys. **37**, 1621 (1979).

[26] O. Atabek and R. Lefebvre, Phys. Rev. **22**, 1817 (1980).

[27] H. Szichman, M. Baer, and A. J. C. Varandas, J. Phys. Chem. **102**, 8909 (1998).

[28] H. Szichman, A. J. C. Varandas, and M. Baer, J. Chem. Phys. **102**, 3474 (1995).

[29] A. J. C. Varandas, Int. Rev. Phys. Chem. **19**, 199 (2000).

[30] H. Szichman, M. Baer, and A. J. C. Varandas, J. Phys. Chem. A **101**, 8817 (1997).

[31] O. Atabek and R. Lefebvre, Phys. Rev. **22**, 1817 (1980).

[32] H.-J. Werner and E. A. Reinsch, J. Chem. Phys. **76**, 3144 (1982).

[33] H.-J. Werner and P. J. Knowles, J. Chem. Phys. **89**, 5803 (1989).

[34] E. R. Davidson, J. Comput. Phys. **17**, 87 (1975).

[35] E. R. Davidson, Comput. Phys. Commun **53**, 49 (1989).

[36] P. E. M. Siegbahn, Chem. Phys. **25**, 197 (1977).

[37] B. O. Roos, Adv. Chem. Phys. **15**, 153 (1972).

[38] J. Cízek, J. Chem. Phys. **45**, 4256 (1966).

[39] J. Cízek, Adv. Chem. Phys. **14**, 35 (1969).

[40] J. Cízek and J. Paldus, Int. J. Quantum Chem. **5**, 359 (1971).

[41] G. D. Purvis III and R. J. Bartlett, J. Chem. Phys **76**, 1910 (1982).

[42] G. E. Scuseria and H. F. Schaefer, Chem. Phys. Lett. **142**, 354 (1987).

[43] P. Piecuch and J. Paldus, J. Quantum Chem. **36**, 429 (1998).

[44] J. Noga and R. J. Bartlett, J. Chem. Phys. **86**, 7041 (1987).

[45] K. Raghavachari, J. A. Pople, E. S. Replogle, and M. Head-Gordon, J. Phys. Chem. **94**, 5579 (1990).

[46] R. J. Bartlett, J. D. Watts, S. A. Kucharski, and J. Noga, Chem. Phys. Lett. **165**, 513 (1990).

[47] Z. He and D. Cremer, Theor Chim Acta **85**, 305 (1993).

[48] J. Paldus and X. Li, Adv. Chem. Phys. **110**, 1 (1999).

[49] P. Piecuch, K. Kowalski, I. S. O. Pimienta, and M. J. McGuire, Int.Rev. Phys. Chem. **21**, 527 (2002).

[50] P. Piecuch, K. Kowalski, P. D. Fan, and I. S. O. Pimienta, *Progress in Theoretical Chemistry and Physics* (Kluwer, Dordrecht, 2003), vol. 12, chap. Advanced Topics in Theoretical Chemical Physics, pp. 119–206.

[51] P. Piecuch, M. Włoch, M. Lodriguito, and J. R. Gour, *Progress in Theoretical Chemistry and Physics* (Springer, 2006), vol. 15, chap. Recent Advances in the Theory of Chemical and Physical Systems, pp. 45–106.

[52] P. Piecuch, K. Kowalski, I. S. O. Pimienta, and M. J. McGuire, Int. Rev. Phys. Chem. **112**, 349 (2004).

[53] P. Piecuch, S. A. Kucharski, K. Kowalski, and M. Musiał, Comp. Phys. Comm. **149**, 71 (2002).

[54] P. Piecuch and M. Włoch, J. Chem. Phys. **123**, 224105 (2005).

[55] P. Piecuch, M. Włoch, J. R. Gour, and A. Kinal, Chem. Phys. Lett. **418**, 467 (2006).

[56] M. Włoch, J. R. Gour, and P. Piecuch, J. Phys. Chem. A **111**, 11359 (2007).

[57] K. Kowalski and P. Piecuch, J. Chem. Phys **113**, 5644 (2000).

[58] K. Kowalski and P. Piecuch, J. Chem. Phys **113**, 18 (2000).

[59] P. Piecuch and K. Kowalsk, *Computational Chemistry: Reviews of Current Trends*, vol. 5 (World Scientific, Singapore, 2000).

[60] M. Włoch, M. D. Lodriguito, P. Piecuch, and J. R. Gour, Mol. Phys. **104**, 2149 (2006).

[61] P. Piecuch, M. Włoch, and A. J. C. Varandas, *Progress in Theoretical Chemistry and Physics* (Springer, Berlin, 2007), vol. 16, p. 65.

[62] P. Piecuch, M. Włoch, and A. J. C. Varandas, Theoretical Chemistry Accounts: Theory, Computation, and Modeling (Theoretica Chimica Acta) **120**, 59 (2008), 10.1007/s00214-007-0297-3.

[63] C. J. Cramer, M. Włoch, P. Piecuch, C. Puzzarini, and L. Gagliardi, J. Phys. Chem. A **110**, 1991 (2006).

[64] C. J. Cramer, P. P. A. Kinal, M. Włoch, and L. Gagliardi, J. Phys. Chem. A **110**, 11557 (2006).

[65] Y. Ge, M. S. Gordon, and P. Piecuch, J. Chem. Phys. **127**, 174106 (2007).

[66] A. Kinal and P. Piecuch, J. Phys. Chem. A **110**, 367 (2006).

[67] A. Kinal and P. Piecuch, J. Phys. Chem. A **111**, 734 (2007).

[68] M. J. McGuire and P. Piecuch, J. Am. Chem. Soc. **127**, 2608 (2005).

[69] P. Piecuch, S. Hirata, K. Kowalski, P. D. Fan, and T. Windus, J. Am. Chem. Soc. **106**, 79 (2006).

[70] K. Kowalski and P. Piecuch, J. Chem. Phys. **122**, 074107 (2005).

[71] S. Hirata, P.-D. Fan, A. A. Auer, M. Nooijen, and P. Piecuch, J. Chem. Phys. **121**, 12197 (2004).

[72] M. J. McGuire, K. Kowalski, S. A. K. P. Piecuch, and M. Musiał, J. Phys. Chem. A **108**, 8878 (2004).

[73] M. J. McGuire, K. Kowalski, and P. Piecuch, J. Chem. Phys. **117**, 3617 (2002).

[74] C. D. Sherrill and P. Piecuch, J. Chem. Phys. **122**, 124104 (2005).

[75] K. Kowalski and P. Piecuch, Chem. Phys. Lett. **344**, 165 (2001).

[76] P. Piecuch, S. A. Kucharski, V. Špirko, and K. Kowalski, J. Chem. Phys. **115**, 5796 (2001).

[77] P. Piecuch, K. Kowalski, I. S. O. Pimienta, and S. A. Kucharski, *Low-Lying Potential Energy Surfaces*, vol. 828 of *ACS Symposium* (American Chemican Society, Washington, D.C., 2002).

[78] J. C. Slater, Phys. Rev. **36**, 57 (1930).

[79] S. F. Boys, Proc. R. Soc., London **A200**, 542 (1950).

[80] J. Almlöf, T. Helgaker, and P. R. Taylor, J. Phys. Chem. **92**, 3029 (1988).

[81] J. Almlöf and P. Taylor, J. Chem. Phys. **86**, 4070 (1987).

[82] A. D. McLean and G. S. Chandler, J. Chem. Phys. **72**, 5639 (1980).

[83] M. S. Gordon, J. S. Binkley, J. A. Pople, W. J. Pietro, and W. J. Hehre, J. Am. Chem. Soc. **104**, 2797 (1982).

[84] J. S. Binkley, J. A. Pople, and W. J. Hehre, J. Am. Chem. Soc. **102**, 939 (1980).

[85] M. J. Frish, J. A. Pople, and J. S. Binkley, J. Chem. Phys. **50**, 3265 (1984).

[86] P. C. Hariharan and J. A. Popel, Theor. Chim. Acta. **28**, 213 (1973).

[87] T. H. Dunning Jr., J. Chem. Phys. **90**, 1007 (1989).

[88] R. A. Kendall, T. H. Dunning Jr., and R. J. Harrison, J. Chem. Phys. **96**, 6769 (1992).

[89] H. B. Jansen and P. Ross, Chem. Phys. Lett. **3**, 140 (1969).

[90] B. Liu and A. D. McLean, J. Chem. Phys. **59**, 4557 (1973).

[91] F. Boys and F. Bernardi, Mol. Phys. **19**, 553 (1970).

[92] A. J. C. Varandas, Chem. Phys. Lett. **194**, 333 (1992).

[93] A. J. C. Varandas, Theo. Chem. Acc. **119**, 511 (2008).

[94] A. J. C. Varandas, J. Comput. Chem. **30**, 379 (2009).

[95] A. J. C. Varandas, J. Phys. Chem. A **114**, 8505 (2010).

[96] A. J. C. Varandas, Int. J. Quantum. Chem. **111**, 416 (2011).

[97] F. B. Brown and D. G. Truhlar, Chem. Phys. Lett. **117**, 307 (1985).

[98] A. J. C. Varandas, J. Chem. Phys. **90**, 4379 (1989).

[99] A. J. C. Varandas, Mol. Phys. **53**, 1303 (1984).

[100] J. S. Wright and S. K. Gray, J. Chem. Phys. **69**, 67 (1978).

[101] J. N. L. Connor, Comp. Phys. Comm. **17**, 117 (1979).

[102] G. C. Schatz, Rev. Mod. Phys. **61**, 669 (1989).

[103] F. London, Z. Electrochem. **35**, 552 (1929).

[104] S. Sato, J. Chem. Phys. **23**, 2465 (1955).

[105] H. Eyring and M. Polanyi, Z. Phys. Chem. B **12**, 279 (1931).

[106] F. O. Ellison, J. Am. Chem. Soc. **85**, 3540 (1963).

[107] J. C. Tully, in *Potential Energy Surfaces*, edited by K. Lawley (Wiley, New York, 1980), p. 63.

[108] P. J. Kuntz, in *Atom-Molecule Collision Theory*, edited by R. Bernstein (Plenum, New York, 1979), pp. 79–110.

[109] K. S. Sorbie and J. N. Murrell, Mol. Phys. **29**, 1387 (1975).

[110] A. J. C. Varandas and J. N. Murrell, Faraday Discuss. Chem. Soc. **62**, 92 (1977).

[111] J. N. Murrell, S. Carter, S. C. Farantos, P. Huxley, and A. J. C. Varandas, *Molecular Potential Energy Functions* (Wiley, Chichester, 1984).

[112] A. J. C. Varandas, Adv. Chem. Phys. **74**, 255 (1988).

[113] A. J. C. Varandas, in *Lecture Notes in Chemistry*, edited by A. Laganá and A. Riganelli (Springer, Berlin, 2000), vol. 75, pp. 33–56.

[114] A. J. C. Varandas and J. Brandão, Mol. Phys. **45**, 857 (1982).

[115] A. J. C. Varandas, J. Mol. Struct. Theochem. **120**, 401 (1985).

[116] A. J. C. Varandas and J. Brandão, Mol. Phys. **57**, 387 (1986).

[117] A. J. C. Varandas and J. D. Silva, J. Chem. Soc., Faraday Trans. 2 **82**, 593 (1986).

[118] A. J. C. Varandas, J. Chem. Phys. **105**, 3524 (1996).

[119] A. J. C. Varandas and L. A. Poveda, Theor. Chem. Acc. **116**, 404 (2006).

[120] M. A. Matías and A. J. C. Varandas, Mol. Phys. **70**, 623 (1990).

[121] A. J. C. Varandas and S. P. J. Rodrigues, J. Phys. Chem A **110**, 485 (2006).

[122] E. Martínez-Núñez and A. J. C. Varandas, J. Phys. Chem. A **105**, 5923 (2001).

[123] W. H. Press, S. A. Teukolski, W. T. Vetterling, and B. P. Flannery, *Numerical Recipes in Fortran: the Art of Scientific Computing* (Cambridge University Press, New York, 1992).

[124] A. J. C. Varandas, F. B. Brown, C. A. Mead, D. G. Truhlar, and N. C. Blais, J. Chem. Phys. **86**, 6258 (1987).

[125] A. J. C. Varandas and A. A. C. C. Pais, J. Chem. Soc., Faraday Trans. 2 **89**, 1511 (1993).

[126] G. Lynch, R. Steckler, D. W. Schwenke, A. J. C. Varandas, D. G. Truhlar, and B. C. Garrett, J. Chem. Phys. **94**, 7136 (1991).

[127] M. R. Pastrana, L. A. M. Quintales, J. Brandão, and A. J. C. Varandas, J. Phys. Chem. **94**, 8073 (1990).

[128] A. J. C. Varandas and A. I. Voronin, J. Phys. Chem. **99**, 15846 (1995).

[129] Y. Z. Song and A. J. C. Varandas, J. Chem. Phys. **130**, 134317 (2009).

[130] S. Joseph and A. J. C. Varandas, J. Phys. Chem. A **113**, 4175 (2009).

[131] B. R. L. G. ao and A. J. C. Varandas, J. Phys. Chem. A **113**, 14424 (2009).

[132] V. Mohan and N. Sathyamurthy, Comp. Phys. Rep. **7**, 213 (1988).

[133] D. C. Clary, J. Phys. Chem. **91**, 1718 (1987).

[134] J. Z. H. Zhang and W. H. Miller, J. Chem. Phys. **91**, 1528 (1989).

[135] J. N. Murrell and A. J. C. Varandas, Mol. Phys. **57**, 415 (1986).

[136] J. N. Murrell and S. Carter, J. Phys. Chem. **88**, 4887 (1984).

[137] H. Goldstein, *Classical Mechanics* (Addison-Wesley, Reading, 1980).

[138] R. Fletcher, *Practical Methods of Optimization* (Wiley, Chichester, 1987).

[139] S. P. J. Rodrigues, *A Monte Carlo based program for optimization of potential energy surfaces* (Developed at the Theoretical and Computational Chemistry group, Coimbra).

[140] IUPAC, *Compendium of chemical terminology (IUPAC, 1997)* (2nd edn., 1997).

[141] M. A. Collins, Adv. Chem. Phys. **93**, 389 (1996).

[142] M. A. Collins, Theor. Chem. Acc. **108**, 313 (2002).

[143] T. Hollebeek, T.-S. Ho, and H. Rabitz, Annu. Rev. Phys. Chem. **46**, 169 (1999).

[144] A. J. C. Varandas and L. Zhang, Chem. Phys. Lett. **385**, 409 (2004).

Chapter 3

Exploring PESs via dynamics calculations

The study of molecular reaction dynamic deals with the rearrangement of atoms during a reaction and it is very important to understand the fundamental physical and chemical processes occurring in a chemical reaction. If the process under study can be assumed as an adiabatic one, a more simple and useful treatment involves the use of a potential energy surface as an interparticle interaction potential in classical equations of motion. Indeed, when dealing with slow molecular collisions, a potential energy surface, as discussed in the present work, provide the interaction energy as a function of the configuration of the system throughout the rearrangement from reactants to products. A common approach to study the dynamics of chemical reactions is the quasiclassical trajectory (QCT) method [1–4] For the study of reactions presented in this thesis, a QCT method was used. The basis of QCT as well as some features of molecular reaction dynamics are briefly reviewed in this chapter.

ing amplitude as a function of energy.

3.1 The QCT method

Classical and semiclassical approaches are justified by the known agreement with exact quantum-mechanical results and are extremely handy. In this thesis we have used only the quasiclassical trajectory (QCT) method of approaching molecular collisions. The QCT method assumes that each of the nuclei comprising a chemical system moves according to the laws of classical mechanics in the force field arising from the adiabatic electronic energy of the system. The method may also extended to cases where the Born-Oppenheimer (BO) separation of electronic and nuclear motion breaks down provided that such breakdown is confined to localized regions of configuration space. The term "quasiclassical" is used to denote the manner in which molecules are prepared before collision, such as the initial conditions. In the QCT method, molecules are prepared in discrete internal energy states corresponding to the quantum states of the molecule. Once the trajectory is begun, this quantum restriction is relaxed so that the time evolution of the system is governed solely by classical mechanics.

In the QCT method the time evolution of the classical degrees of freedom of individual atoms are simulated by solving Hamilton's or Newton's equations of motion expressed in term of the coordinates $\mathbf{q}$ and momentum $\mathbf{p}$ of the system. In the Hamilton formulation[5], propagation is done by numerical integration of the first-order differential

$$\frac{dq_i}{dt} = \frac{\partial H\left(\mathbf{q},\mathbf{p}\right)}{\partial p_i}, \qquad \frac{dp_i}{dt} = -\frac{\partial H\left(\mathbf{q},\mathbf{p}\right)}{\partial q_i} \tag{3.1}$$

where the Hamiltonian function of the system (H) is the sum of the kinetic $T(\mathbf{p},\mathbf{q})$ and potential $V(\mathbf{q})$ energies:

$$H\left(\mathbf{q},\mathbf{p}\right) = T\left(\mathbf{q},\mathbf{p}\right) + V\left(\mathbf{q}\right) \tag{3.2}$$

There are several components to a classical trajectory simulations[3,6–8] $V(\mathbf{q})$ is the already mentioned PES, which has been represented by an empirical function with adjustable parameters or an analytical fit to electronic structure theory calculations. For this task, Hamilton's equations (3.1) are solved numerically and numerous algorithms have been developed in an efficient and accurate manner. When a set of trajectories is completed, the final values of momenta and coordinates are transformed into quantities, that maybe

compared with experiment, such as reaction rate constants, product vibrational, rotational, and relative translational energies. The remaining problem of a quasiclassical trajectory simulation is choosing the initial conditions so that the results from an ensemble of trajectories may be compared with experiment and/or theory, and used to make predictions about the chemical system's molecular dynamics. Monte Carlo methods are commonly used[1,2,4] for sampling appropriate distributions of initial values of coordinates and momenta.

In the molecular collisions studied in this thesis, the VENUS[9] code was utilized. Such a package uses Monte Carlo method for selecting initial conditions of the reactants. Integration of the classical equations of motions is carried out in a combination of fourth-order Runge-Kutta and sixth-order Adams Multon algorithms[3]. Some details are presented in the following.

3.1.1 Unimolecular decomposition

Unimolecular reaction occur as suggested by lindemann by successive excitation of the unimolecular reactant molecule A through collisions with bath to an energized state A^* with a vibrational-rotational excitation above the unimolecular threshold E_0 from which the molecule has probability to dissociate to products different from zero. A question of fundamental interest here is whether this dissociation is at random during the complete decomposition[13–15]. If so, the lifetime distribution $P(yt)$, and the probability of decomposition of the initial number of reactant molecules $N(0)$ in the ensemble per unit time, is given by[13]

$$P\left(t\right) = -\frac{1}{N(0)}\frac{dN(t)}{dt} = k\left(E\right)\exp\left[-k\left(E\right)t\right] \tag{3.3}$$

given equal probability during any time interval for reaction to occur. $k(E)$ is the classical microcanonical unimolecular rate constant, which is expressed as[15]

$$k(E) = \frac{N(E)}{h\rho(E)} \tag{3.4}$$

where $N(e)$ is the sum of states at the transition state for the decomposition and $\rho(E)$ is the density of states for A*. According to the classical/quantum correspondence princi-

ple[16,17], the classical and quantum $k(E)$ become equivalent at high energies. However, for E near the unimolecular threshold E_0, the classical $k(E)$ may be significantly larger than the quantum $k(E)$, since classical mechanics allows the transition state to be crossed and products to be performed without the presence of zero-point energy[17].

3.1.2 QCT method for Bimolecular reactions

As was mentioned in preceding paragraphs, a dynamical study of a molecular collision can be carried out by means of classical equations. However, once configurations of the separated reagents are described by their vibrational and rotational (ro-vibrational) quantum states, initial conditions of the collision should be generated accounting for them. This is the idea of QCT method[18]: to solve classical equations of motion considering the initial conditions of the reactants according to their quantum states. Similarly, the states of the product molecules can be assigned by determining the quantum numbers describing the best their ro-vibrational motion.

Classical trajectory simulations are widely used to study the dynamics of gas-phase bimolecular reactions. The quantities of interest in such studies commonly include the reaction cross-section and the thermal bimolecular rate constant. In principle, the cross-section for the reaction between a collision partner A and a collision partner B to form products,

$$A + B \rightarrow \text{products} \tag{3.5}$$

For the simple case of an atom B plus a symmetric top polyatomic molecule A, the reactive cross-section may be expressed as

$$\sigma_r = \sigma_r(\upsilon_{vel}, \nu_A, J_A, K_A) \tag{3.6}$$

where υ_{vel} is the A + B relative velocity and ν_A , J_A and K_A are the vibrational and rotational quantum numbers of polyatomic.

Assuming the polyatomic reactant have Boltzmann distributions of vibrational-rotational levels specified by temperature T_A, special values ν_A, (J_A,K_A) are not selected, and the

reactive cross-section can be obtained as

$$\sigma_r(\upsilon_{\text{rel}}, T_A) = \sum_{\nu_A} \sum_{J_A,K_A} \sigma_r(\upsilon_{rel}, \nu_A, J_A, K_A)\mathcal{P}(\nu_A, T_A)\mathcal{P}(J_A, K_A, T_A) \tag{3.7}$$

where $\mathcal{P}(\nu_A, T_A)$ and $\mathcal{P}(J_A, K_A, T_A)$ are the normalized Boltzmann distributions for ν_A and (J_A,K_A) at temperature T_A

Multiplying Eq.(3.7) by the relative velocity υ_{rel} and integrating over the Boltzmann distribution one gets the bimolecular thermal rates constant:

$$k\left(T\right) = \int_0^\infty \upsilon_{rel}\sigma_r\left(\upsilon_{rel}; T\right)\mathcal{P}\left(\upsilon_{rel}; T\right)d\upsilon_{rel} \tag{3.8}$$

or if it is written in terms of relative translational energy:

$$k\left(T\right) = \left(\frac{8k_BT}{\pi\mu}\right)^{1/2} \int_0^\infty \sigma_r\left(E_{tr}\right)\frac{E_{tr}}{\left(k_BT\right)^2}e^{-E_{tr}/kT}dE_{tr} \tag{3.9}$$

where μ is the reduced mass of the system, and K_B the Boltzmann constant.

When a batch of N trajectories are calculated and N_r of them were reactive, the reaction cross section (whether for specific ro-vibrational levels or not) may be calculated as[2]:

$$\sigma_r = \frac{N_r}{N}\pi b_{max}^2 \tag{3.10}$$

being b_{max} the largest impact parameter that leads to reaction.

In the same way, as the translational energies are randomly sampled, the bimolecular rate constant in (3.9) may be expressed as[4]

$$k\left(T\right) = \left(\frac{8k_BT}{\pi\mu}\right)^{1/2}\frac{N_r}{N}\pi b_{max}^2 \tag{3.11}$$

3.2 Products properties from QCT runs

The end of a trajectory is ascertained by periodically examining the inter-atomic distances during the integration procedure[6,8]. Once the product molecules have been determined by testing interatomic distances using geometric and energetic criteria, it can be determined whether the molecules are in bound, quasi-bound or dissociative states. In the

present thesis, we have used the proximity-type algorithms developed by Varandas and co-workers[19] to identify the different reaction channels.

In the chemical reaction:

$$\mathrm{A} + \mathrm{B} \rightarrow \mathrm{C} + \mathrm{D} \tag{3.12}$$

Among the properties of the products of a collision that are of interest in the case of bimolecular reactions are the relative translational energy of C + D, C and D vibrational and rotational energies, and the scattering angle between the initial A + B and the final C + D relative velocity vectors. It is almost straightforward to calculate these properties from the coordinate and velocities of each atom in the product into the vibrational and rotational components. The procedures here described are incorporated in the general chemical dynamics program VENUS[9] used to calculate the trajectories for the reactions studied in this thesis.

3.2.1 Relative velocity and translational energy

The product relative velocity is the difference between the velocities of the centers of mass of C and D. For example for the x component of the center of mass position and velocity of product D is given by:

$$X_{\mathrm{D}} = \sum_{i=1}^{n_{\mathrm{D}}} m_i x_i / M_{\mathrm{D}} \,, \;\; \dot{X}_{\mathrm{D}} = \sum_{i=1}^{n_{\mathrm{D}}} m_i \dot{x}_i / M_{\mathrm{D}} \tag{3.13}$$

where the sum is over n_{D}, the number of atoms in D, m_i are the masses and x_i are the x coordinates of the atoms. M_{D} is the mas of D, upper case variables identify the center of mass position and velocity. The product relative velocity is the time derivative of the relative coordinate:

$$\begin{aligned} \mathbf{R} &= \mathbf{R}_{\mathrm{D}} - \mathbf{R}_{\mathrm{C}} \\ &= (X_{\mathrm{D}} - X_{\mathrm{C}})\mathbf{i} + (Y_{\mathrm{D}} - Y_{\mathrm{C}})\mathbf{j} + (Z_{\mathrm{D}} - Z_{\mathrm{C}})\mathbf{k} \\ &= R_x\mathbf{i} + R_y\mathbf{j} + R_z\mathbf{k} \\ \dot{\mathbf{R}} &= \dot{R}_x\mathbf{i} + \dot{R}_y\mathbf{j} + \dot{R}_z\mathbf{k} \end{aligned} \tag{3.14}$$

where $\mathbf{i}, \mathbf{j}, \mathbf{k}$ are the unitary vectors in the *x,y,z* directions respectively. The pro-duct translational energy is:

$$E_{rel} = \frac{\mu_{\mathrm{CD}} \dot{\mathbf{R}} \cdot \dot{\mathbf{R}}}{2} \tag{3.15}$$

where $\mu_{\mathrm{CD}} = M_{\mathrm{C}} M_{\mathrm{D}} / (M_{\mathrm{C}} + M_{\mathrm{D}})$ is the CD reduced mass. E_{rel} may also be written as the sum of the relative translational energy along the line of centers $\mathrm{C-D}$ and the energy of the orbital (angular) motion:

$$E_{rel} = \frac{\mu_{\mathrm{CD}} \dot{R}^2}{2} + \frac{l^2}{2\mu_{\mathrm{CD}} R^2} \tag{3.16}$$

being $\dot{R}$ the module of the velocity along line of centers (radial velocity), and R the distance between them:

$$R = (\mathbf{R} \cdot \mathbf{R})^{1/2}\,, \;\; \dot{R} = \frac{R_x \dot{R}_x + R_y \dot{R}_y + R_z \dot{R}_z}{R} \tag{3.17}$$

$\mathbf{l}$ is the orbital angular momentum (and l its module):

$$\mathbf{l} = \mu_{\mathrm{CD}} \mathbf{R} \times \dot{\mathbf{R}} = l_x \mathbf{i} + l_y \mathbf{j} + l_z \mathbf{k} \tag{3.18}$$

3.2.2 Velocity scattering angle

The velocity scattering angle θ_v is the angle between the relative velocity vector for the reactants $\dot{\mathbf{R}}^0$ and the product's relative velocity vector $\dot{\mathbf{R}}$, given by:

$$\theta_v = \cos^{-1}\left(\frac{\dot{\mathbf{R}} \cdot \dot{\mathbf{R}}^0}{\dot{R}\dot{R}^0}\right) \tag{3.19}$$

3.2.3 Internal energy

To calculate the internal rotational and vibrational energy of the products requires the coordinates and velocities of each atom of the molecule in the center of mass frame of the molecule:

$$x_i' = x_i - X_{\mathrm{D}}\,, \;\; \dot{x}_i' = \dot{x}_i - \dot{X}_{\mathrm{D}}\,, \;\; i = \overline{1, n_{\mathrm{D}}} \tag{3.20}$$

the internal energy of D is:

$$E_{\mathrm{D}} = T_{\mathrm{D}} + V_{\mathrm{D}} \tag{3.21}$$

where T_{D} and V_{D} are the kinetic and vibrational energies of D respectively. V_{D} is determined from the potential energy function and T_{D} is given by:

$$T_{\mathrm{D}} = \sum_{i=1}^{n_{\mathrm{D}}} \frac{m_i(\dot{x}_i^2 + \dot{y}_i^2 + \dot{z}_i^2)}{2} \tag{3.22}$$

3.2.4 Rotational angular momentum

The rotational angular momentum $\mathbf{j}$ of the product molecule D is the sum of the angular momentum $\mathbf{j}_i$ of the individual atoms of D relative to its center of mass:

$$\mathbf{j}_{\mathrm{D}} = \sum_{i=1}^{n_{\mathrm{D}}} \mathbf{j}_i = j_x\mathbf{i} + j_y\mathbf{j} + j_z\mathbf{k} \tag{3.23}$$

the atomic angular momentum is given by:

$$\mathbf{j}_i = m_i\mathbf{r}'_i \times \dot{\mathbf{r}}'_i \tag{3.24}$$

The total angular momentum of the C + D products is the vector sum:

$$\boldsymbol{\mathcal{L}} = \mathbf{l} + \mathbf{j}_{\mathrm{C}} + \mathbf{j}_{\mathrm{D}} \tag{3.25}$$

3.2.5 Rotational and vibrational energies

If the product correspond to a diatomic species, same procedure as previously described in equations (3.15-3.18) can be used. The internal energy T_{D} of a diatomic molecule 1-2, can be written:

$$T_{\mathrm{D}} = \frac{\mu_{12}\dot{r}^2}{2} + \frac{j^2}{2\mu_{12}r^2} \tag{3.26}$$

where μ_{12} is the reduced mass of D, r is the 1-2 bond length. Similar expressions than (3.15-3.18) are used for r and $\dot{r}$. The rotational quantum number J for D is found from the expression:

$$j = \sqrt{J(J+1)}\hbar \tag{3.27}$$

Since calculation is classical, non-integer values are obtained for J; then, rounding is often used.

The vibrational quantum number is obtained with help of semi-classical quantization condition[20] p71:

$$\oint p_r \mathrm{d}r = (n + \frac{1}{2})2\pi\hbar \tag{3.28}$$

where the momentum $p_r = \mu\dot{r}$ and the cyclic integral denotes integration over one orbit. From the equations (3.21) and (3.26) p_r is given by:

$$p_r = \left[2\mu_{12}\left(E_\mathrm{D} - \frac{j^2}{2\mu_{12}r^2} - V_\mathrm{D}(r)\right)\right]^{1/2} \tag{3.29}$$

as for J, non-integer values of n are often obtained.

If D is a polyatomic species it is not a simple to calculate rotational and vibrational quantum numbers[4]. Semi-classical quantization can be used as in case of diatomic molecules, presented above. However, mostly because of the multidimensional character, such a task is tedious. As a result most of the semi-classical quantization has been limited to triatomics. So far, there is not a general form to calculate both rotational and vibrational quantum numbers from its Cartesian coordinates[4].

It is always possible to calculate the average vibrational and rotational energies of a polyatomic product:

$$E_\mathrm{D} = \langle E_\mathrm{D}^{vib}\rangle + \langle E_\mathrm{D}^{rot}\rangle \tag{3.30}$$

Because of the ro-vibrational coupling the vibrational and rotational energies of D, E_D^{vib} and E_D^{rot}, will fluctuate as the molecule vibrates. An instantaneous rotational energy for D may be calculated from:

$$E_\mathrm{D}^{rot} = \frac{1}{2}\boldsymbol{\omega}_\mathrm{D} \cdot \mathbf{j}_\mathrm{D} \tag{3.31}$$

$\mathbf{j}_\mathrm{D}$ has been defined in (3.23) and $\boldsymbol{\omega}_\mathrm{D}$ is the angular velocity of D.

The average rotational energy is computed by averaging over the longest vibrational period of the product. Then, by means of equation (3.31), the average vibrational energy can also be obtained.

3.3 Excitation function and rate constant

Molecular beam experiments provide high initial collision energy resolution[21]. That is why they are often employed to measure the translational energy dependence of the reaction

cross section (excitation function). Much of the interesting information about an elementary chemical reaction can be summarized in such a function [22]. Besides, it is also needed to calculate the rate constant for specific ro-vibrational states of the reactants. Once its value is obtained for a given translational energy, some models are used to represent it.

3.3.1 Reaction with barrier

Based on the fitting of available data, LeRoy [22] proposed some particular models:

Class I reactions

$$\sigma(E_{\rm tr}) = \begin{cases} C(E_{\rm tr} - E_{\rm tr}^{\rm th})^n e^{-m(E_{\rm tr}-E_{\rm tr}^{\rm th})} & E_{\rm tr} \geq E_{\rm tr}^{\rm th} \\ 0 & E_{\rm tr} < 0 \end{cases} \tag{3.32}$$

where $m, n \geq 0$. Those functions increase from 0 at $E_{\rm tr} = E_{\rm tr}^{\rm th}$, the exponential term causes the excitation function to pass through a maximum as the energy increase. Such a dependence describe properly the excitation functions for neutral-neutral reactions. The $H + SO_2$ reaction studied by Ballester *et al.* [23] properly fit to this model.

By substituting (3.32), an analytical expression for the rate constant is obtained:

$$\begin{aligned} k(T) &= C\left(\frac{8k_BT}{\pi\mu}\right)^{1/2} \frac{(k_BT)^n e^{-E_{\rm tr}^{\rm th}/k_BT}}{(1+mk_BT)^{n+2}} \times \\ &\quad \times \left[\Gamma(n+2) + \Gamma(n+1)\frac{(1+mk_BT)E_{\rm tr}^{\rm th}}{k_BT}\right] \end{aligned} \tag{3.33}$$

where Γ is the Gamma function, see appendix.

Class II reactions

$$\sigma(E_{\rm tr}) = \begin{cases} \frac{C(E_{\rm tr}-E_{\rm tr}^{\rm th})^n}{E_{\rm tr}} e^{-m(E_{\rm tr}-E_{\rm tr}^{\rm th})} & E_{\rm tr} \geq E_{\rm tr}^{\rm th} \\ 0 & E_{\rm tr} < 0 \end{cases} \tag{3.34}$$

these functions are very similar to the previous one, however they include the excitation function for the collision of hard spheres which requires a critical energy $E_{\rm tr}^{\rm th}$ [21]. This excitation function yields to a rate constant:

$$k(T) = C\left(\frac{8k_BT}{\pi\mu}\right)^{1/2} \frac{(k_BT)^{n-1}\Gamma(n+1)e^{-E^{\rm th}/k_BT}}{(1+mk_BT)^{n+1}} \tag{3.35}$$

Class III reactions

$$\sigma(E_{\rm tr}) = \begin{cases} CE_{\rm tr}^{n} & E_{\rm tr} \geq E_{\rm tr}^{\rm th} \\ 0 & E_{\rm tr} < 0 \end{cases} \tag{3.36}$$

This type of functions applies for collisions between low energy ions and polarizable molecules[22]. For these functions, the rate constant becomes:

$$k(T) = C\left(\frac{8k_BT}{\pi\mu}\right)^{1/2}(k_BT)^n[\Gamma(n+2) - P(n+2, E_{\rm tr}^{\rm th}/k_BT)] \tag{3.37}$$

being P the incomplete Gamma function, see appendix.

3.3.2 Barrier-free reaction

In the collision of two particles (with masses m_1 and m_2) interacting along the centers of mass line, the two-body problem can be simplified into a one-body problem. There, a particle of mass μ ($\mu = m_1m_2/(m_1 + m_2)$) moves under the influence of an effective potential ($V_{\rm eff}$) given by the sum of the interaction between both particles and a centrifugal potential[24].

For reactions which proceed through an attractive potential energy surface, without a barrier (capture-like), the centrifugal barrier on the effective potential $V_{\rm eff}$ may still prevent reaction. To obtain a simple model of such a kind of collision, structureless reactants will be assumed. Considering also a long-range attractive potential in the form:

$$V(R) = -\frac{C_n}{R^n} \tag{3.38}$$

where C_n and n are parameters depending on the interaction type, with $n=3$ when there are dipole-dipole like, $n=4$ for quadrupole-dipole and so on[25,26]. The distance between reactants is represented by R. Of course the above assumption is a large simplification of the problem as in real collisions we deal with reactants having different electric multipoles and also their values can change as the reaction proceeds. However, these effects are supposed to be included in the values on n and C_n with some intermediate values, not corresponding exactly to any specific multipole interaction, but to a mixture of them.

The effective potential becomes:

$$V_{\rm eff}(R) = E_{\rm tr}\frac{b^2}{R^2} - \frac{C_n}{R^n} \tag{3.39}$$

where b is the impact parameter. $V_{\text{eff}}(R)$ has a maximum value at $R = R_0$:

$$R_0 = \left(\frac{nC_n}{2E_{\text{tr}}b^2}\right)^{1/(n-2)} \tag{3.40}$$

With the condition that the translational energy must equal the maximum value of the effective potential for $b{=}b_{max}$, the excitation function then becomes:

$$\sigma(E_{\text{tr}}) = \pi b_{max}^2 = n\pi(n-2)^{(2-n)/n}\left(\frac{C_n}{2E_{\text{tr}}}\right)^{2/n} \tag{3.41}$$

By substituting the previous expression into (**??**), the rate constant is obtained as:

$$k(T) = 2n\pi(n-2)^{(2-n)/n}\left(\frac{2}{\pi\mu}\right)^{1/2}\left(\frac{C_n}{2}\right)^{2/n}\Gamma\left(\frac{2n-2}{n}\right)(k_BT)^{(n-4)/2n} \tag{3.42}$$

Even when this result was obtained for a simplified model of interaction, it fits particularly well the radical-radical reactions[27].

3.4 Final ro-vibrational states

After integrating the classical equations of motion for a given initial condition, the rotational and vibrational energies of the product molecule (C) can assume any value, having a continuous distribution. However it is often interesting to study a reaction as a state-to-state phenomena, and for that purpose one needs to attribute energy quantum number for the product of each trajectory.

3.4.1 Semiclassical binning

A normally used approach for doing so is the semicalsssical binning. From this perspective the rotational quantum number is obtained for the final momenta of the product molecule, using the fact that at the turning points, the kinetic energy is purely rotaional:

$$\frac{\boldsymbol{P}}{2\mu} = \frac{\hbar j(j+1)}{2\mu(q_{\pm})^2} \tag{3.43}$$

and the quantum number is obtained by soving this equation for j and rounding the result to an integer. In turn the vibrational energy is given by the semiclassical (Bohr-Sommerfeld) quantization rule for a non rotating molecule. Noting that the vibrational

diatomic energy is constant and equal to $V_{\mathrm{C}}(q_{\pm})$, the kinetic energy is written in function of the internuclear distance as $V_{\mathrm{C}}(q_{\pm}) - V_{\mathrm{C}}(q)$, it follows that:

$$(n + 1/2)h = 2\int_{q_-}^{q^+} p dq = 2\int_{q_-}^{q^+} [2\mu(V_{\mathrm{C}}(q_{\pm}) - V_{\mathrm{C}}(q))]^{-1/2}\, dq \tag{3.44}$$

where again the equation is solve for n and rounded to an integer.

3.4.2 Momentum Gaussian binning

A more elaborated scheme for binning the QCT output is the recently proposed Momentum Gaussian Binning (MGB)[28,29]. Within this approach, instead of assigning quantum number for each trajectory, this method gives probability distribution over the various quantum numbers, which is summed over all the calculated trajectories. The state-specific cross section and rate constant can be calculated afterwards by using the probability of an specific state as given by the distribution summed over all trajectories.

The physical basis behind this approach consist of considering the ith trajectory as a wave package ψ^i and expanding it in terms of the products orthonormal ro-vibrational eigen-states $\phi_{\alpha\beta}$

$$\psi^i = \sum_{\alpha\beta} c^i_{\alpha\beta} |\phi_{\alpha\beta}\rangle \tag{3.45}$$

where the coefficients $c_{\alpha\beta}i$ contain information about how much of the trajectory i is localized at the diatomic eigenvalue $E_{\alpha\beta} = \langle\phi_{\alpha\beta}|H|\phi_{\alpha\beta}\rangle$. The internal energy obtained from the integration of the classical trajectory could then be expressed as

$$\varepsilon^i \langle\psi^i|H|\psi^i\rangle = \sum_{\alpha\beta} {c^i_{\alpha\beta}}^* c^i_{\alpha\beta} \langle\phi_{\alpha\beta}|H|\phi_{\alpha\beta}\rangle = \sum_{\alpha\beta} W^i_{\alpha\beta} E_{\alpha\beta} \tag{3.46}$$

where W^i is a two dimensional probability matrix, whose elements are understood as weights. The final desired probability that a product molecule is found in the state ν, j is expressed as a sum of $W_{\nu,j}$ over all trajectories.

$$p_{\nu,j} = \sum_{i=1}^{N_{\mathrm{traj}}} W^i_{\nu,j} \tag{3.47}$$

The main problem now is to obtain an approximated way to determine the matrix W^i for each trajectory, since the exact determination of it would imply a knowledge of the coefficients $c^i_{\alpha\beta}$, which is not achievable. Assuming separability of the vibrational and rotational degrees of freedom, one get $W^i_{\alpha\beta} = W^i_\alpha W^i_\beta$, and the MGB approach consists of writing these weights as

$$W^i_\alpha = \frac{1}{\rho_\alpha\sqrt{\pi}}\exp\left(-\left[\frac{\sqrt{E_\alpha}-\sqrt{\varepsilon^i}}{\rho_\alpha\sqrt{\bar{E}_\alpha}}\right]^2\right) \tag{3.48}$$

where ρ is a unitless Gaussian decay parameter and $\bar{E}_\alpha$ is an average separation of two neighboring levels from the basis $((E_{\alpha+1} - E_{\alpha-1})/2)$. Note that this Gaussian is centered at the trajectory energy, making the most weighted states as those with eigenvalues near it. A similar expression holds for the rotational levels (W^i_β).

The parameters ρ_α and ρ_β are considered fine-tuning constant to give the method even more realism. The value of ρ_α is fixed at $\rho_\alpha = 0.1$ while ρ_β is determined as ρ_α times the ratio of the average spacing between vibration levels and the average spacing between rotational levels.

The use of MGB scheme provides a smoother distribution over the quantum states of the product[29–31], if compared to the semiclassical approach, since every trajectory contributes for different quantum states with a given probability, instead of assign just one number. Besides that, the MGB is a non-active scheme that accounts for the leakage of zero point (ZPE) energy in QCT (For this problem, see also Refs. 32–37). This happens because, if a trajectory have a final energy inferior that the ZPE of the product diatomic ($\varepsilon < E_0$), its probability contribution to the ground state population will be smaller, if compared to a trajectory ending up with $\varepsilon = E_0$.

3.5 ZPE leakage of QCT

To study chemical reactions, although the QCT method is computationally easier and faster than quantal methods, it has several shortcomings. The two most serious limitations are the failure to preserve zero-point energy (ZPE) and inability to describe tunnelling

effects. The ZPE would constitute significantly to the total energy, and it can leak to a specific weak bond or into the reaction coordinate, non-physically enhancing reaction. Of course, this effect may partially cancel the lack of tunnelling by facilitating passages over a potential barrier[38].

Within the quasclassical spirit, the trajectories at least begin with zero point vibrational energy in all vibrational degrees of freedom, however, the classical equations of motion Eq. (3.1), do not prevent the vibrational energy in the different modes from dipping below its zero point value at a given moment during the evolution of the system under study. This can lead to significant discrepancies between the classical and quantal results.

For correcting this problem within the quasiclassical method the approaches are divided between active and non-active. In the so-called active schemes 18–21 a normal mode analysis is performed at each integration step to check whether all normal modes have energy superior to the ZPE. In case the condition is violated for a given mode, the trajectory is corrected by changing its point in phase space according to a given scheme. These methods often find problems for an exact conservation of energy and angular momentum, or in some cases make the trajectory not time-reversible.

The non-active method, trajectories which are found to violate some pre-specified physical criteria, for example, vibrational and rotational energy requirement in the products and reagents in the QCT-NVEQMT[35] scheme, are discard from the final statistical analysis[33,35,39–42].

As a final remark, one should notice that simply discarding such trajectories for one of the above methods may introduce a statistical error in the analysis, a problem that was addressed by Varandas in Ref.(36) where a simple model denoted unified statistical (US) model was proposed.

Bibliography

[1] G. H. Peslherbe, H. Wang, and W. L. Hase, Adv. Chem. Phys. **105**, 171 (1999).

[2] M. Karplus, R. N. Porter, and R. D. Sharma, J. Chem. Phys. **43**, 3259 (1965).

[3] D. L. Bunker, Meth. Comp. Physics **10**, 287 (1971).

[4] W. L. Hase, *Encyclopedia of Computational Chemistry* (Wiley, New York, 1998).

[5] H. Goldstein, *Classical Mechanics* (Addison- Wesley, Reading, 1980).

[6] R. N. Porter and L. M. Raff, in *Modern Theoretical Chemistry, Dynamics of Molecular Collisions, part B, vol. II*, edited by W. Miller (Plenum, New York, 1976), p. 1.

[7] D. G. Truhlar and J. T. Muckerman, in *Atom-Molecule Collision Theory*, edited by R. Bernstein (Plenum, New York, 1979), p. 505.

[8] L. M. Raff and D. L. Thompson, in *Theory of Chemical Reaction Dynamics*, edited by M. Baer (Chemical Rubber, Boca Raton, 1985), p. 1.

[9] W. L. Hase, MERCURY: a general Monte-Carlo classical trajectory computer program, QCPE#453. An updated version of this code is VENUS96: W. L. Hase, R. J. Duchovic, X. Hu, A. Komornik, K. F. Lim, D.-H. Lu, G. H. Peslherbe, K. N. Swamy, S. R. van de Linde, A. J. C. Varandas, H. Wang, R. J. Wolf, QCPE Bull 1996, *16*, 43.

[10] R. A. Marcus and O. K. Rice, J. Phys. and Colloid Chem. **55**, 894 (1951).

[11] R. A. Marcus, J. Chem. Phys. **20**, 359 (1952).

[12] D. M. Wardlaw and R. A. Marcus, Adv. Chem. Phys. **70**, 231 (1988).

[13] D. L. Bunker, J. Chem. Phys. **40**, 1946 (1964).

[14] D. L. Bunker and W. L. Hase, J. Chem. Phys. **54**, 4621 (1973).

[15] D. L. Bunker, *Unimolecular Reaction Dynamics. Theory and Experiments* (Oxford University Press, New York, 1996).

[16] M. C. Gutzwiller, *Chaos in Classical and Quantum Mechanics* (Springer-Verlag, Heidelberg, 1990).

[17] J. H. Hammersley and D. C. Handscomb, *Monte Carlo Methods* (Chapman and Hall, London, 1964).

[18] M. Karplus, R. N. Porter, and R. D. Sharma, J. Chem. Phys. **40**, 2033 (1964).

[19] A. J. C. Varandas, A. A. C. C. Pais, J. M. C. Marques, and W. Wang, Chem. Phys. Lett. **249**, 264 (1996).

[20] A. S. Davydov, *Quantum Mechanics* (Edicion Revolucionaria, La Habana, 1965).

[21] M. Brouard, *Reaction Dynamics* (Oxford University Press, 1998).

[22] R. L. Le Roy, J. Chem. Phys. **73**, 4338 (1969).

[23] M. Y. Ballester, P. J. S. B. Caridade, and A. Varandas, Chem. Phys. Lett. **439**, 301 (2007).

[24] H. Goldstein, *Classical Mechanics* (Addison- Wesley, London, 1950).

[25] J. D. Jackson, *Classical Electrodynamics* (Academic Press, New York, 1999), 3rd edn.

[26] J. O. Hirschfelder, C. F. Curtis, and R. B. Bird, *Molecular Theory of Gases and Liquids* (Wiley, New York, 1954).

[27] A. J. C. Varandas, in *Conferencias Plenarias de la XXIII Reunienal de Química*, edited by A. S. Feliciano, M. Grande, and J. Casado (Universidad de Salamanca, Salamanca, 1991), p. 321.

[28] L. Bonnet and J. C. Rayez, Chem. Phys. Lett. **277**, 183 (1997).

[29] A. J. C. Varandas, Chem. Phys. Lett. **439**, 386 (2007).

[30] Y. Z. Song, P. J. S. B. Caridade, and A. Varandas, J. Phys. Chem. A **113**, 9213 (2009).

[31] P. J. S. B. Caridade, B. R. L. G. ao, and A. Varandas, J. Phys. Chem. A **114**, 6063 (2010).

[32] A. J. C. Varandas, J. Brand and M. R. Pastrana, J. Chem. Phys. **96**, 5137 (1992).

[33] A. J. C. Varandas and J. M. C. Marques, J. Chem. Phys. **97**, 4050 (1992).

[34] A. J. C. Varandas and L. Zhang, Chem. Phys. Lett. **385**, 409 (2004).

[35] A. J. C. Varandas, J. Chem. Phys. **99**, 1076 (1993).

[36] A. J. C. Varandas, Chem. Phys. Lett. **225**, 18 (1994).

[37] A. J. C. Varandas, Chem. Phys. Lett. **235**, 111 (1995).

[38] M. E. Mandy and P. G. Martin, J. Phys. Chem. **95**, 8726 (1991).

[39] J. C. Gray, D. G. Truhlar, L. Clemens, J. W. Duff, F. M. C. Jr., G. O. Morrell, and E. F. Hayes, J. Chem. Phys. **69**, 240 (1978).

[40] J. C. Gray, B. C. Garrett, and D. G. Truhlar, J. Chem. Phys. **70**, 5921 (1979).

[41] G. Nyman and J. Davidsson, J. Chem. Phys. **92**, 2415 (1990).

[42] G. Nyman, Chem. Phys. **173**, 159 (1993).

Part II

Publications

THE JOURNAL OF PHYSICAL CHEMISTRY A

Article

pubs.acs.org/JPCA

Accurate ab-Initio-Based Single-Sheeted DMBE Potential-Energy Surface for Ground-State N_2O

Jing Li and António J. C. Varandas*

Departamento de Química, Universidade de Coimbra, 3004-535 Coimbra, Portugal

Supporting Information

ABSTRACT: A global accurate double-many-body expansion potential-energy surface is reported for the electronic ground state of N_2O. The new form is shown to accurately mimic the ab-initio points calculated at the multireference configuration interaction level using the aug-cc-pV*T*Z basis set and the full-valence-complete-active-space wave function as reference. To improve the calculated raw energies, they have been extrapolated to the completed basis set limit and most importantly to the full configuration-interaction limit by correcting semiempirically the calculated dynamical correlation with the double-many-body expansion-scaled external correlation method. The topographical features of the novel potential-energy surface were examined in detail and compared with those of other potential functions available in the literature. Good agreement with the experimental data is observed.

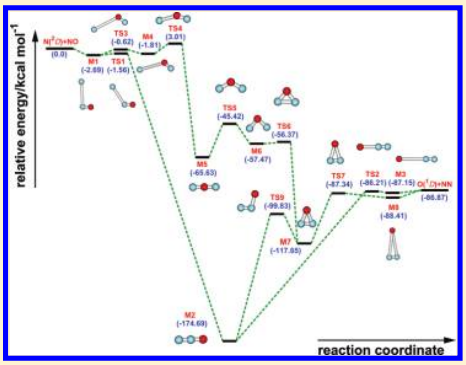

1. INTRODUCTION

Nitrous oxide (N_2O) is an extremely important species in atmospheric chemistry. Emission of N_2O is currently the single most important ozone-depleting process and expected to remain the largest throughout the 21st century.[1] Among the main three dissociation processes of the title system,

$$N_2O(X^1\Sigma^+) \rightarrow O(^1D) + N_2(X^1\Sigma_g^+) \quad (1)$$

$$\rightarrow N(^2D) + NO(X^2\Pi) \quad (2)$$

$$\rightarrow O(^3P) + N_2(X^1\Sigma_g^+) \quad (3)$$

process 1 is the main loss mechanism and therefore has a significant impact on the chemistry of the atmosphere, being studied in great detail experimentally as well as theoretically. Process 2 can also take place in the ground electronic state of N_2O, but only a few theoretical studies and several experimental kinetic ones are available. Dissociation of N_2O via channel 3 to singlet and triplet states is forbidden under $C_{\infty v}$ symmetry but becomes allowed under C_s symmetry and may be significant due to vibrational averaging.

The nitrous oxide molecule has been an important subject of study in a number of scientific fields such as life sciences,[2] earth sciences,[3] atmospheric sciences,[4] and fuel industry.[5] It has also been the subject of various theoretical and experimental studies.[6−8] Theoretical studies of nitrous oxide date back to the two-dimensional potential-energy surfaces (PESs) calculated by Brown et al.[9] with the NN bond length kept fixed at the experimental value of 2.13199 a_0 and used by Johnson et al.[10] in dynamics calculations. In the same year, Nakamura and Kato[11] calculated the spin-forbidden predissociation reaction of N_2O using a PES of the double-many-body-expansion (DMBE[12−14]) family fitted to their own ab-initio calculations for the singlet and triplet surfaces that are coupled by spin−orbit terms. Subsequently, González et al.[15] made an extensive theoretical study of the $N(^2D) + NO(X^2\Pi) \rightarrow O(^1D) + N_2(X^1\Sigma_g^+)$ exothermic reaction on its lowest $^1A'$ PES and found several minima and transition states along the different minimum energy paths (MEPs) connecting reactants and products. Improved electronic structure calculations were later carried out by Daud et al.[16] using the complete-active-space self-consistent field (CASSCF) and multireference configuration-interaction (MRCI) methods, still keeping the NN bond fixed at the equilibrium value. At about the same time, Nanbu and Johnson[17] reported full three-dimensional PESs and utilized them for dynamics calculations. Recently, Schinke[18] calculated the ground-state and exited-state potential-energy surfaces and performed dynamics calculations. Most recently, Defazio et al.[19] reported spin−orbit and Renner−Teller quantum dynamics of the spin-forbidden quenching reaction $O(^1D) + N_2(X^1\Sigma_g^+) \rightarrow O(^3P) + N_2(X^1\Sigma_g^+)$ on the N_2O $\tilde{X}^1A'$, $\tilde{a}^3A''$, and $\tilde{b}^3A'$ PESs. For the ground electronic state of the N_2O molecule, the majority of structural studies focus on its global minimum. Thus, the design of the grid of points chosen to calculate the PES via ab-initio calculations is usually focused onto the vicinity of the potential well of the linear $C_{\infty v}$ isomer. Indeed, as far as we are aware, no work toward obtaining a global potential-energy surface for the ground state of N_2O has been reported. Therefore, there is a need for a realistic global potential-energy surface of nitrous oxide, which covers a large angular area and is sufficiently accurate for studies of reaction dynamics and chemical kinetics. Thus, we report in the present

Received: March 6, 2012
Revised: April 11, 2012
Published: April 11, 2012

work a realistic global PES for ground-state N_2O via DMBE[12−14] theory which is calibrated from 809 ab-initio points calculated at the multireference configuration interaction (MRCI)[20] level of theory using the full-valence-complete-active-space (FVCAS)[21] wave function as reference and Dunning's[22,23] aug-cc-pVTZ (AVTZ) basis set. The ab-initio energies calculated in this way have been subsequently corrected using the double-many-body expansion-scaled external correlation method (DMBE-SEC)[24] method to extrapolate them to the complete configuration-interaction limit. As usual in DMBE theory, the PES so obtained (hereinafter referred to as DMBE PES) shows the correct long-range behavior at all dissociation channels while providing a realistic representation of the surface features at all interatomic separations.

The paper is organized as follows. Section 2 reports the ab-initio calculations here performed, while section 3 surveys the DMBE formalism. The topographical features of the DMBE PES are discussed in section 4. Section 5 gathers the concluding remarks.

2. AB-INITIO CALCULATIONS

Ab-initio calculations have been carried out at the MRCI level using the FVCAS wave function as reference. The AVTZ basis set of Dunning has been employed, with the calculations performed using the Molpro[25] package. A grid of 809 ab-initio points has been chosen to map the PES over the O−N_2 region defined by $1.5 \le R_{N_2}/a_0 \le 3.5$, $1.0 \le r_{O-N_2}/a_0 \le 10.0$, and $0 \le \gamma/\text{deg} \le 90$. For the N−NO interactions, a grid defined by $1.5 \le R_{NO}/a_0 \le 3.5$, $1.0 \le r_{N-NO}/a_0 \le 10.0$, and $0 \le \gamma/\text{deg} \le 180$ has been chosen. For both channels, r, R, and γ are the atom−diatom Jacobi coordinates.

To account for electronic excitations beyond singles and doubles and, most importantly, for the incompleteness of the basis set, the calculated ab-initio energies have been subsequently corrected using the DMBE-SEC method. Thus, the total DMBE-SEC interaction energy is written as

$$V(\mathbf{R}) = V_{\text{FVCAS}}(\mathbf{R}) + V_{\text{SEC}}(\mathbf{R}) \tag{4}$$

where

$$V_{\text{FVCAS}}(\mathbf{R}) = \sum_{\text{AB}} V^{(2)}_{\text{AB,FVCAS}}(R_{\text{AB}}) + V^{(3)}_{\text{ABC,FVCAS}}(\mathbf{R}) \tag{5}$$

$$V_{\text{SEC}}(\mathbf{R}) = \sum_{\text{AB}} V^{(2)}_{\text{AB,SEC}}(R_{\text{AB}}) + V^{(3)}_{\text{ABC,SEC}}(\mathbf{R}) \tag{6}$$

where $\mathbf{R} = \{R_{\text{AB}},R_{\text{BC}},R_{\text{AC}}\}$ is a collective variable of all internuclear distances. Explicitly, expansion of the two terms in eq 6 assumes the form

$$V^{(2)}_{\text{AB,SEC}}(R_{\text{AB}}) = \frac{V^{(2)}_{\text{AB,FVCAS-CISD}}(R_{\text{AB}}) - V^{(2)}_{\text{AB,FVCAS}}(R_{\text{AB}})}{F^{(2)}_{\text{AB}}} \tag{7}$$

$$V^{(3)}_{\text{ABC,SEC}}(\mathbf{R}) = \frac{V^{(3)}_{\text{AB,FVCAS-CISD}}(\mathbf{R}) - V^{(3)}_{\text{ABC,FVCAS}}(\mathbf{R})}{F^{(3)}_{\text{ABC}}} \tag{8}$$

Following previous work,[24] $F^{(2)}_{\text{AB}}$ in eq 7 is chosen to reproduce the bond dissociation energy of the corresponding AB diatom while $F^{(3)}_{\text{ABC}}$ in eq 8 is estimated as the average of the three two-body F factors. Such a procedure leads to the following results for the AVTZ basis set: $F^{(2)}_{\text{NN}} = 0.3532$, $F^{(2)}_{\text{NO}} = 0.6532$, and $F^{(3)}_{\text{ONN}} = 0.5532$. Not surprisingly, due to triple-ζ basis sets being known to recover only a modest fraction of the calculated dynamical correlation, the scaling factor for N_2 turns out to be smaller than 0.5. Although this could, in principle, question the validity of the approach, it turns out that the results to be presented later do not appear to show any undesirable misprediction. Since the use of a larger basis set would make the present work much more expensive, we are content with those here presented.

3. DOUBLE-MANY-BODY-EXPANSION POTENTIAL-ENERGY SURFACE

The title system has the following dissociation scheme

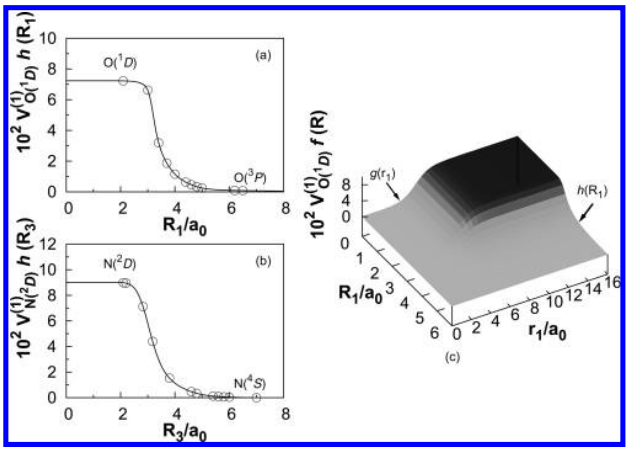

Figure 1. Switching function used to model the pseudo-one-body energy terms in the single-sheeted N_2O DMBE PES of the present work. (a) Fit of the $h(R_1)$ switching form to the ab-initio points calculated for the O + N_2 configuration as a function of the N−N distance (R_1). (b) Fit of $h(R_3)$ for the N + NO configuration as a function of the N−O distance (R_3). (c) Perspective view of the global switching function $f_1(\mathbf{R})$ for oxygen.

$$N_2O(^1A') \rightarrow N_2(X^1\Sigma_g^+) + O(^1D) \tag{9}$$

$$\rightarrow NO(X\,^2\Pi) + N(^2D) \tag{10}$$

Since the diatomic molecules $NO(X\,^2\Pi)$ and $N_2(X^1\Sigma_g^+)$ dissociate to their ground-state atoms [i.e., $N(^4S)$ and $O(^3P)$] but the excited-state atoms [i.e., $N(^2D)$ and $O(^1D)$] appear in the above two channels, it is unavoidable to use switching functions in order to obtain an approximate representation of the actual multisheeted PES by a single-sheeted one. Such a procedure has been proposed by Murrell and Carter,[26] who applied it in the construction of an approximate PES for the ground-state H_2O. Accordingly, in 2000 González et al.[15] made a detailed study of the reaction

$$N(^2D) + NO(X\,^2\Pi) \rightarrow O(^1D) + N_2(X\,^1\Sigma_g^+)$$

using the switching function for the oxygen and nitrogen atoms. Although the Murrell−Carter switching forms (also utilized by González et al.[15]) can ensure the correct asymptotic limit, they fail to warrant a unique value for the energy at the geometries of the system where three atoms are far away from each other. Such inconsistency prompted us to obtain a single-sheeted function capable of mimicking both the $N(^2D)$ + $NO(X\,^2\Pi)$

dx.doi.org/10.1021/jp302173h | J. Phys. Chem. A 2012, 116, 4646−4656

Table 1. Equilibrium Geometries (in Angstroms), Vibrational Frequencies (cm^{-1}), and Dissociation Energies (kcal mol^{-1}) of N_2 and NO

	$N_2(X^1\Sigma_g^+)$			$NO(X^2\Pi)$			ΔE^c	
method	R_e	D_e	w_e	R_e	D_e	w_e	$N(^4S-^2D)$	$O(^3P-^1D)$
DMBE PES[a]	1.1038	228.47	2331.6	1.1563	152.56	1884.4	56.34	45.39
CASSCF/AVTZ[b]	1.1056	212.04	2330.6	1.1558	130.10	1880.2	69.97	51.42
MRCI(Q)/AVTZ[b]	1.1056	219.23	2322.3	1.1585	144.52	1882.1	58.68	46.73
CASSCF/6-311G(2d)[15]	1.1056	210.36	2334.6	1.1609	128.23	1878.0	66.00	51.51
CASPT2/6-311G(2d)[15]	1.1034	212.55	2316.7	1.1598	140.73	1857.9	62.07	48.65
exp.[50,51]	1.0977	228.41	2358.6	1.1508	152.53	1904.2	54.96	45.37

[a]This work. From the potential-energy curves fitted to MRCI/AVTZ energies. [b]This work. From ab-initio points at CASSCF and MRCI(Q) levels of theory. [c]Energy difference between $N(^4S)$ to $N(^2D)$ and $O(^3P)$ to $O(^1D)$.

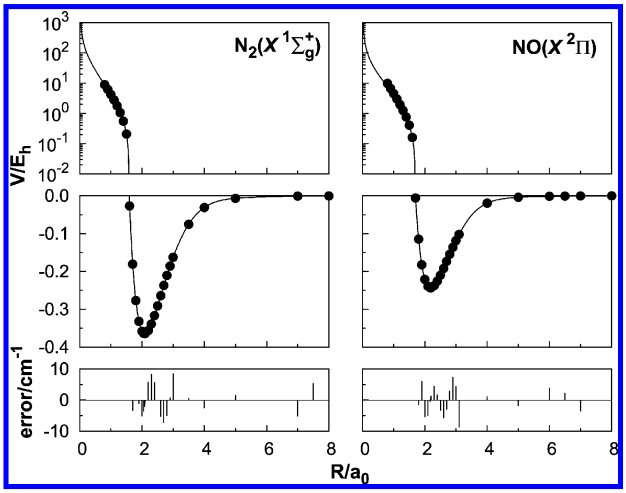

Figure 2. Potential-energy curve for $N_2(X^1\Sigma_g^+)$ and $NO(X^2\Pi)$ and the differences between the energies predicted from the fit and the actual ab-initio energies.

Table 2. Numerical Values for NO Dipole and Quadrupole Moments and NN Quadrupole Moment

	D_{NO}	Q_{NO}	Q_{NN}
Q_∞/ea_0^2		0.449421	0.0
M_6/ea_0^8		3500	3500
R_{ref}/a_0	3.32461	5.17897	4.9296
D_M[a]	−0.234954	−0.0594638	−0.150932
a_1/a_0^{-1}	−0.161567	0.749951	0.879603
a_2/a_0^{-2}	−0.738644	0.272525	0.288471
a_3/a_0^{-3}	0.471858	0.0132849	0.0189779
b_1/a_0^{-1}		2.50415	2.5508
b_1/a_0^{-2}	0.462051	0.502533	0.54759
b_1/a_0^{-3}	0.18244	0.0196438	0.0170144

[a]The units are ea_0 for D_{NO} and ea_0^2 for Q_{NO} and Q_{NN}.

and the $O(^1D) + N_2(X^1\Sigma_g^+)$ dissociation limits using a variant of a switching function previously developed in our group[27] assuming the form

$$h_i(\mathbf{R}_i) = \frac{1}{4}\sum_{m=1}^{2}\{1 - \tanh[\alpha_m(R_i - R_i^{m0}) + \beta_m(R_i - R_i^{m1})^3]\}, \quad i = 1, 2, 3 \tag{11}$$

where i = 1, 2, and 3 are indexes employed to label the O, N_a, and N_b atoms, respectively, R_1, R_2, and R_3 represent the N_a−N_b, N_a−O, and N_b−O distances, respectively, while a and b

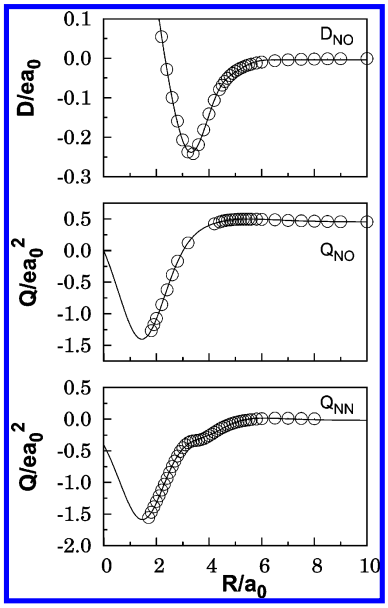

Figure 3. Variation of the NO dipole and quadrupole moments and NN quadrupole moment with internuclear distance.

Table 3. Stratified Root-Mean-Square Deviations (in kcal mol^{-1}) of the DMBE PES

energy[a]	N^b	max dev[c]	rmsd	$N^d_{>rmsd}$
10	76	0.478	0.187	19
20	93	1.297	0.268	19
30	106	1.473	0.344	17
40	109	1.473	0.371	18
50	116	1.473	0.400	20
60	121	1.473	0.410	22
70	136	2.312	0.507	26
80	161	4.103	0.798	32
90	189	4.103	0.841	39
100	243	4.103	0.843	55
200	617	4.142	0.916	159
300	802	4.142	0.932	202
400	807	4.142	0.936	204
500	809	4.142	0.940	204

[a]The units of energy and rmsd are kcal mol^{-1}. [b]Number of points in the indicated energy range. [c]Maximum deviation up to the indicated energy range. [d]Number of points with an energy deviation larger than the rmsd.

dx.doi.org/10.1021/jp302173h | J. Phys. Chem. A 2012, 116, 4646−4656

distinguish the two identical N atoms. In turn, α_m and β_m are parameters to be calibrated from a least-squares fit to an extra set of 15 AVTZ points that control the $O(^1D)-O(^3P)$ decay as the N_a-N_b distance increases for O + N_2 configurations, as shown in Figure 1a, and another set of 23 AVTZ points that control the $N(^2D)-N(^4S)$ decay as the N_b-O distance increases for the N_a + N_bO configurations, as shown in Figure 1b. Because N_a and N_b are indistinguishable, the same set of parameters in the switching function is attributed to nitrogen atoms *a* and *b*. As a check to the fit, we observe that at the diatomic equilibrium bond length the switching function becomes smaller than 10^{-6}, thus warranting the correct energetics at the $N(^2D)$ + $NO(X\ ^2\Pi)$ and $O(^1D)$ + $N_2(X^1\Sigma_g^+)$ asymptotes. To get a smooth three-body energy term, we further choose to multiply eq 11 by an amplitude function that annihilates eq 11 at short range (short $O-N_2$ and N−NO distances)

$$g_i(\mathbf{r}_i) = \frac{1}{2}\{1 + \tanh[\alpha(r_i - r_i^0)]\},\ i = 1, 2, 3 \tag{12}$$

where $\mathbf{r}_1$ is the distance of the O atom to the center of mass of N_2. A word is necessary at this point to clarify the notation. The indexes (*i,j,k*) number atoms (say, 1 for O and 2 and 3 for N), and r_i represents the Jacobi coordinate separating atom *i* from the center of mass of diatom *jk* whose bond distance is itself denoted by R_i. The final switching function then assumes the form

$$f_i(\mathbf{R}) = g_i(r_i)h_i(R_i),\ i = 1, 2, 3 \tag{13}$$

with the parameters of $g(r_i)$ being chosen such as to guarantee that its main effect occurs for $O-N_2$ and N−NO distances larger than 8 a_0 or so, as illustrated in Figure 1c. All numerical values of the parameters in eq 13 are collected in Table 1.

Within the framework of DMBE theory, the single-sheeted PES assumes the form

$$\begin{aligned} V(\mathbf{R}) = {} & V^{(1)}_{O(^1D)} f_1(\mathbf{R}) + V^{(1)}_{N_a(^2D)} f_2(\mathbf{R}) + V^{(1)}_{N_b(^2D)} f_3(\mathbf{R}) \\ & + \sum_{i=1}^{3} [V^{(2)}_{EHF}(R_i) + V^{(2)}_{dc}(R_i)] + V^{(3)}_{EHF}(\mathbf{R}) \\ & + V^{(3)}_{dc}(\mathbf{R}) \end{aligned} \tag{14}$$

In the one-body term $V^{(1)}_{O(^1D)}$ represents the energy difference between the ^1D and the ^3P states of atomic oxygen, $V^{(1)}_{O(^1D)}$ = 0.0723399 E_h, and $f_1(\mathbf{R})$ is the switching function used to warrant the correct behavior at the $N_2(X^1\Sigma_g^+)$ + $O(^1D)$ dissociation limits. Similarly, $V^{(1)}_{Na(^2D)}$ and $V^{(1)}_{Nb(^2D)}$ represent the energy difference between the $N(^2D)$ and $N(^4S)$ states: $V^{(1)}_{Na(^2D)}$, $V^{(1)}_{Nb(^2D)}$ = 0.0898679 E_h. Correspondingly, $f_2(\mathbf{R})$ and $f_3(\mathbf{R})$ are the switching functions that warrant the correct behavior at the $NO(X\ ^2\Pi)$ + $N(^2D)$ dissociation limit. Table 1 compares the calculated energy differences for atomic oxygen and nitrogen with the experimental results. As seen, the results of the DMBE PES give a very good overall behavior of such attributes, improving significantly the energy differences with respect to ab-initio results. The energy differences for nitrogen and oxygen with respect to the experimental data are seen to be of 1.38 and 0.02 kcal mol^{-1} (respectively), thus in very good agreement with the experimental counterpart. Of course, this is an essential requirement for construction of a realistic PES to be used for dynamics and kinetics studies.

Note that we used the switching functions for O, N_a, and N_b separately. In fact, for the title system, when the oxygen atom is in the $O(^1D)$ excited state, the nitrogen atom must decay to $N(^4S)$, because the N_2 fragment is on its ground singlet state. This behavior is well described by our switching functions, since the oxygen atom is in the $O(^1D)$ excited state for large intermolecular distances of r_{O-N_2} and short N−N bond distances, with both N_a and N_b decaying to $N(^4S)$ with growing N−O distance. Of course, an accurate representation of the PES would require at least a double-sheeted representation of the PES, i.e., $N(^4S)$ + $N(^4S)$ + $O(^1D)$ and $N(^2D)$ + $N(^4S)$ + $O(^3P)$. However, we expect the above approximate single-sheeted representation to provide a realistic description of the lowest adiabatic singlet-state PES for the title molecule.

As usual in DMBE theory, the two-body and three-body energy terms will be split into two contributions: the extended Hartree−Fock (EHF) and dynamical correlation (dc) energies. The following subsections give a brief description of the various energy terms, with the reader being addressed to refs 27 and 28 and references therein for details.

3.1. Two-Body Energy Terms. For the diatomic potential-energy curves, we employ the extended Hartree−Fock approximate correlation energy method, including the united atom limit (EHFACE2U),[29] which shows the correct behavior at the asymptotes $R \to 0$ and $R \to \infty$. In turn, the EHF energy part of diatomic curve assumes the form

$$V_{EHF}(R) = -\frac{D}{R}\left(1 + \sum_{i=1}^{n} a_i r^i\right)\exp(-\gamma r) \tag{15}$$

where $\gamma = \gamma_0[1 + \gamma_1 \tanh(\gamma_2 r)]$ and $r = R - R_e$ is the displacement from the equilibrium diatomic geometry. In turn, the dc energy contribution is written as[30]

$$V_{dc}(R) = -\sum_{n=6,8,10} C_n \chi_n(R) R^{-n} \tag{16}$$

In the present work, the potential-energy curves for both $NO(X\ ^2\Pi)$ and $N_2(X^1\Sigma_g^+)$ are modeled from our own calculated ab-initio energies and experimental dissociation energy[31,32] as implied by the DMBE-SEC[24] method. As shown in Figure 2, both potential curves mimic accurately the calculated ab-initio energies. Equilibrium geometries, vibrational frequencies, and dissociation energies are also collected in Table 1. As seen, the results at the MRCI(Q) level of theory are closer to the experimental values, although the tendency is not so clear when considering the vibrational frequencies. The increase in accuracy of the dissociation energy of the diatomic when the raw ab-initio points are corrected by scaling[33] the dynamical correlation as in the DMBE-SEC[24] method is remarkable. The numerical values of all parameters for both diatomic curves are gathered in Table 2 of the Supporting Information (the number of significant figures in the tabulated Supporting Information may appear be excessive in some cases but is given for convenience in reproducing the data).

3.2. Three-Body Energy Terms. *3.2.1. Three-Body Dynamical Correlation Energy.* The three-body dc energy assumes the usual form of a summation in inverse powers of the fragment separation distances[28]

$$V^{(3)}_{dc} = -\sum_i \sum_n f_i(\mathbf{R}) \chi_n(r_i) C_n^{(i)}(R_i, \theta_i) r_i^{-n} \tag{17}$$

dx.doi.org/10.1021/jp302173h | J. Phys. Chem. A 2012, 116, 4646−4656

Table 4. Minima of N_2O DMBE PES

feature	method	E^c/kcal mol^{-1}	R_{NN}/Å	R_{NO}/Å	α^d	ω_1	ω_2	ω_3
$C_{\infty v}$								
M2	DMBE[a]	−174.69, −89.63	1.1399	1.1928	180.0	2251.3	1314.1	453.6
	MRCI(Q)/AVTZ[b]	−170.00, −82.55	1.1322	1.1882	180.0	2283.9	1298.8	600.3
	CASPT2/6-311G(2d)[15]	−170.10, −84.85	1.1355	1.1947	180.0	2223.7	1269.6	589.5
	González et al.[15]	−170.90	1.1326	1.1999	180.0	2216.5	1250.2	589.7
	Schinke[18]	−85.63	1.1315	1.1897	180.0			
	exp.[48]	−172.50, −87.25	1.1282	1.1842	180.0	2223.7	1276.5	589.2
$D_{\infty h}$								
M5	DMBE[a]	−65.63	2.4175	1.2087	180.0	1726.6	1059.3	508.4
	MRCI(Q)/AVTZ[b]	−63.25	2.4361	1.2180	180.0	1722.8	1079.6	432.2
	CASPT2/6-311G(2d)[15]	−62.71	2.4256	1.2128	180.0	1695.7	1056.4	434.4
	González et al.[15]	−63.78	2.3237	1.1618	180.0	2041.8	894.1	245.3
C_{2v}								
M6	DMBE[a]	−57.47	1.8520	1.3097	89.5	1222.9	460.1	1037.5
	CASPT2/6-311G(2d)[15]	−46.72	1.7416	1.3547	80.0	1104.8	187.0	890.8
M7	DMBE PES[a]	−117.65	1.1891	1.5145	46.2	2047.0	857.6	235.2
	MRCI(Q)/AVTZ[b]	−102.86	1.2037	1.5492	45.7	1763.3	740.1	267.8
	CASPT2/6-311G(2d)[15]	−103.45	1.2054	1.5487	45.3	1731.0	757.2	303.2
	González et al.[15]	−104.60	1.1558	1.5887	42.7	1745.7	913.7	682.5
M8	DMBE[a]	−88.41	1.1050	3.6426	17.2	2320.8	105.7	40.4
	CASPT2/6-311G(2d)[15]	−85.89	1.1061	2.9785	21.4	2010.3	46.0	299.4
	González et al.[15]	−86.31	1.1170	2.7413	23.5	2153.4	168.9	146.1
C_s								
M1	DMBE[a]	−2.69	3.5776	1.1611	93.0	1823.5	60.2	32.5
	CASPT2/6-311G(2d)[15]	−1.37	3.2166	1.1597	93.4	1801.7	43.9	12.3
	González et al.[15]	−0.65	3.3471	1.1590	158.4	1847.7	64.3	23.0
M3	DMBE PES[a]	−87.15	1.1071	3.9188	179.6	2303.0	53.0	36.9
	CASPT2/6-311G(2d)[15]	−86.10						
	González et al.[15]	−87.37	1.1109	2.8191	131.3	2306.8	184.2	103.8
M4	DMBE[a]	−1.81	3.6426	2.7375	134.6	1869.4	95.3	83.5
	CASPT2/6-311G(2d)[15]	−1.58	3.3416	2.6062	120.2	1854.3	141.6	78.8
	González et al.[15]	−5.05	3.1981	2.7543	102.1	1855.9	293.4	232.2

[a]This work. From fit to DMBE-SEC energies resulting from MRCI(Q)/AVTZ calculations. [b]This work. Stationary points obtained through optimization at the MRCI/AVTZ level of theory. [c]Energies relative to N(^2D) + NO and O(^1D) + N_2 asymptotes, from left-hand side to right-hand side, respectively. [d]α is the angle ∠NON of C_{2v}, $D_{\infty h}$, and NON (C_s) structures, or ∠NNO otherwise.

where the first summation runs over all atom−diatom interactions ($i \equiv$ A−BC), R_i is the diatomic internuclear distance, r_i is the separation between atom A and the center-of-mass separation of the BC diatom, and θ_i is the angle between these two vectors (see Figure 1 of ref 34). In turn, $f_i(\mathbf{R}) = (1/2)\{1 - \tanh[\xi(\eta R_i - R_j - R_k)]\}$ is a convenient switching function. Following recent work,[27] we fixed $\eta = 6$ and $\xi = 1.0a_0^{-1}$, while the damping function $\chi_n(r_i)$ takes the form employed elsewhere.[28,27] All numerical values of the parameters in eq 17 are given in Table 3 in the Supporting Information, while their internuclear dependences are displayed in Figure 1.

3.2.2. Three-Body Electrostatic Energy. The electrostatic energy is due to the interaction of the quadrupole and higher permanent electric moments of O(^1D) and N(^2D) with the dipole and higher ones of $N_2(X^1\Sigma_g^+)$ and NO($X\ ^2\Pi$). In the present work, we considered the interactions of the oxygen quadrupole with the nitric oxide dipole and quadrupole moments and nitrogen quadrupole with the N_2 dipole and quadrupole moments. Following previous work,[35−37] the electrostatic energy is written as

$$V_{ele}^{(3)} = f(\mathbf{R})\{C_4(R, r)A_{DQ}(\theta_a, \theta, \phi_{ab})r^{-4} + C_5(R, r)A_{QQ}(\theta_a, \theta, \phi_{ab})r^{-5}\} \quad (18)$$

where $f(\mathbf{R})$, R, r, and θ have the same meaning as in section 3.2.1, θ_a is the angle that defines the atomic quadrupole orientation, and ϕ_{ab} is the corresponding dihedral angle. Since the N_2 permanent electric dipole moment $D_{NN}(R)$ is 0, the coefficients $C_4(R,r)$ and $C_5(R,r)$ are given by

$$C_4(R, r) = \frac{3}{2}Q_N D_{NO}(R)\chi_4(r)$$

$$C_5(R, r) = \frac{3}{4}\{Q_N Q_{NO}(R) + Q_O Q_{NN}(R)\}\chi_5(r) \quad (19)$$

where $D_{NO}(R)$ and $Q_{NO}(R)$ are the permanent electric dipole and quadruple moments of NO and $Q_{NN}(R)$ is the quadruple moment of NN. Q_N and Q_O are the quadruple moments of the nitrogen and oxygen atoms. The functional form of the angular variations of A_{DQ} and A_{QQ} take the expressions employed in previous work[35,37,38] based on the classical-optimized-quadruple (COQ) model.[39−43]

The analytical expression for the NO dipole has been obtained by fitting our own ab-initio results to the form[44]

$$D(R) = D_M\left(1 + \sum_{i=1}^{3} a_i r^i\right)\exp\left(-a_1 r - \sum_{i=2}^{3} b_i r^i\right) \quad (20)$$

dx.doi.org/10.1021/jp302173h | J. Phys. Chem. A 2012, 116, 4646−4656

Table 5. Transition States of N_2O DMBE PES

feature	ref	E^c/kcal mol^{-1}	R_{NN}/Å	R_{NO}/Å	α^d	ω_1	ω_2	ω_3
$C_{\infty v}$								
TS2	DMBE[a]	−86.21	1.1045	2.3487	180.0	2350.7	136.4	235.5i
	CASPT2/6-311G(2d)[15]	−88.20						
	González et al.[15]	−86.4	1.1027	2.3869	150.6	2335.5	122.8	195.3i
C_s								
TS1	DMBE[a]	−1.56	3.0486	1.1489	124.5	1913.2	84.33	157.5i
	González et al.[15]	−0.46	2.8792	1.1554	140.7	1815.6	103.7	94.6i
TS3	DMBE[a]	−0.62	4.3557	1.1611	113.3	1820.3	48.9	54.3i
	González et al.[15]	−0.13	3.7490	1.1574	93.6	1852.2	38.1	70.1i
TS4	DMBE[a]	3.01	2.8994	2.5354	96.3	1738.1	225.3	254.5i
	CASPT2/6-311G(2d)[15]	1.90	3.0965	2.0914	140.8	1825.6	195.7	509.6i
	González et al.[15]	1.91	2.9979	2.1367	129.9	1709.8	201.6	418.0i
TS9	DMBE[a]	−99.83	1.1743	1.4240	100.3	1664.8	751.3	786.1i
	MRCI(Q)/AVTZ[b]	−89.64	1.1214	1.4208	102.1	1802.3	682.5	724.3i
	CASPT2/6-311G(2d)[15]	−88.65	1.1452	1.4122	101.4	1856.1	549.0	541.7i
	González et al.[15]	−90.46	1.1347	1.4029	97.6	1986.3	810.2	744.7i
C_{2v}								
TS5	DMBE[a]	−45.42	2.2419	1.3055	118.3	960.2	504.4i	1256.6
	MRCI(Q)/AVTZ[b]	−42.48	2.2559	1.3133	118.3	996.6	590.4i	1139.3
	CASPT2/6-311G(2d)[15]	−38.79	2.2650	1.3205	118.1	973.8	570.2i	1117.8
TS6	DMBE[a]	−56.37	1.7986	1.3889	80.7	961.6	262.7i	795.6
	MRCI(Q)/AVTZ[b]	−50.75	1.7965	1.3823	81.0	1042.3	311.6i	892.3
	CASPT2/6-311G(2d)[15]	−46.59	1.7950	1.3465	83.6	1117.5	302.7i	939.9
	González et al.[15]	−45.70	1.7643	1.3171	85.3	1254.0	518.6i	1018.1
TS7	DMBE[a]	−87.34	1.1077	2.2572	28.4	2312.1	232.3i	181.1
	MRCI(Q)/AVTZ[b]	−83.51	1.1122	2.1199	30.0	2155.4	465.3i	282.6
	CASPT2/6-311G(2d)[15]	−83.05	1.1176	2.1043	30.8	2025.9	336.8i	286.8
	González et al.[15]	−82.49	1.1100	2.1379	30.1	2174.7	385.6i	410.1

[a]This work. From fit to DMBE-SEC energies resulting from calculated MRCI(Q)/AVTZ points. [b]This work. Stationary points calculated by optimization at the MRCI/AVTZ level of theory. [c]Energies given relative to N(^2D) + NO asymptote. [d]α is the angle ∠NON for C_{2v} and $D_{\infty h}$ and NON (C_s) structure, or ∠NNO otherwise.

where $r = R - R_{ref}$ and R_{ref} is the reference distance corresponding to the maximum in the $D(R)$ curve. In turn, the variation of the NO and NN quadrupole moments with the internuclear distance as approximated by their z components has been modeled by[43]

$$Q(R) = D_M\left(1 + \sum_{i=1}^{3} a_i r^i\right)\exp\left(-\sum_{i=1}^{3} b_i r^i\right) + Q_\infty + \chi_8(R)\frac{M^6}{R^6} \quad (21)$$

where $r = R - R_{ref}$ with R_{ref} is the reference distance corresponding to the maximum in the $Q(R)$ curve. Q_∞ is the value of the quadrupole limit. The parameters in eqs 20 and 21 are collected in Table 2, while a graphical view of the modeled functions can be seen in Figure 3.

3.2.3. Three-Body Extended Hartree–Fock Energy. The total three-body energy can be obtained, for a given triatomic geometry by removing the sum of the one-body and two-body energy terms from the corresponding DMBE-SEC interaction energies in eq 14. Subsequently, by subtracting both the three-body dc energy part described in eq 17 and the three-body electrostatic energy in eq 18 from the total three-body energy one obtains the three-body EHF energy. This can now be suitably represented by the following three-body distributed polynomial[45] form

$$V_{EHF}^{(3)} = \sum_{j=1}^{5} P^j(Q_1, Q_2, Q_3) \times \prod_{i=1}^{3}\{1 - \tanh[\gamma_i^j(R_i - R_i^{j,ref})]\} \quad (22)$$

where $P^j(Q_1,Q_2,Q_3)$ is the jth polynomial up to six order in the symmetry coordinates which are defined as

$$\begin{pmatrix} Q_1 \\ Q_2 \\ Q_3 \end{pmatrix} = \begin{pmatrix} \sqrt{1/3} & \sqrt{1/3} & \sqrt{1/3} \\ 0 & \sqrt{1/2} & -\sqrt{1/2} \\ \sqrt{2/3} & -\sqrt{1/6} & -\sqrt{1/6} \end{pmatrix}\begin{pmatrix} R_1 - R_1^{j,ref} \\ R_2 - R_2^{j,ref} \\ R_3 - R_3^{j,ref} \end{pmatrix} \quad (23)$$

As usual, we obtain the reference geometries $R_i^{j,ref}$ by first assuming their values to coincide with bond distances of the associated stationary points. Subsequently, we relax this condition via a trial-and-error least-squares fitting procedure. Similarly, the nonlinear range-determining parameters γ_i^j have been optimized in this way. The complete set of parameters amounts to a total of 171 coefficients c_i, 5 nonlinear coefficients γ_i^j, and 5 reference geometries $R_i^{j,ref}$. All numerical values of the least-squares parameters are gathered in Tables 4 and 5 of the Supporting Information. Table 3 shows the stratified root-mean-squared deviations (rmsd) values of the final PES with respect to all fitted ab-initio energies. A total of 809 points covering a range of energy up to ~500 kcal mol^{-1} above the

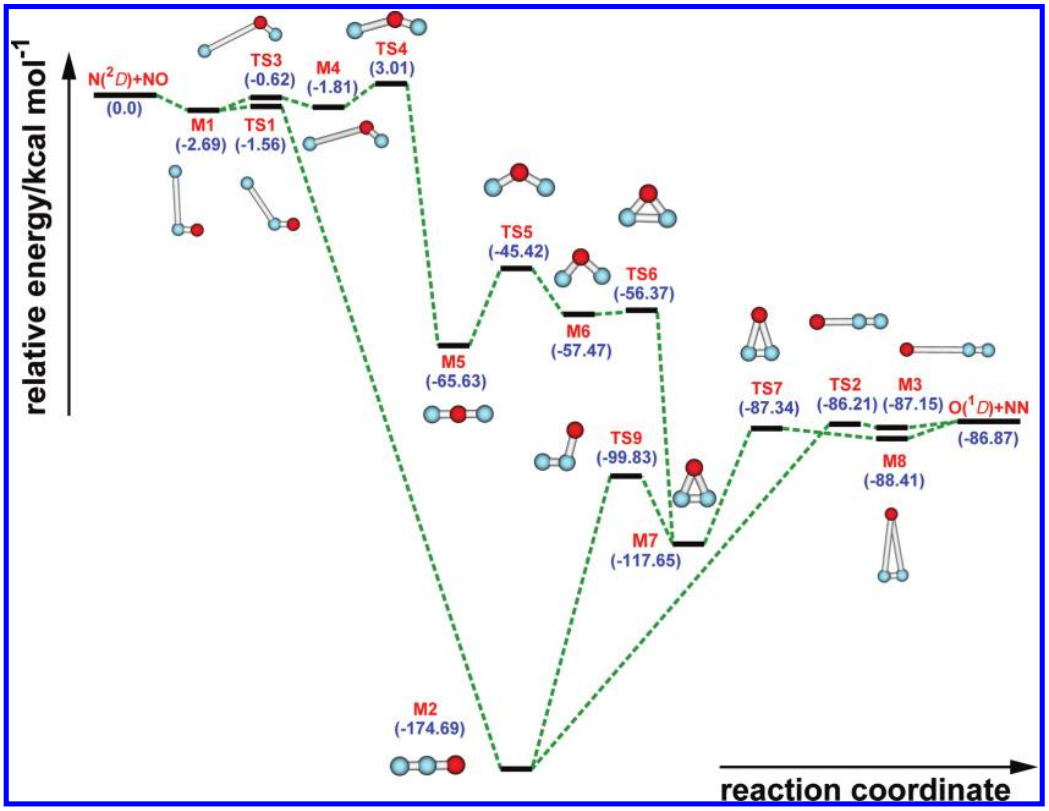

Figure 4. Energy diagram of stationary points located on the double many-body expansion (DMBE) PES. Energies (in kcal mol^{-1}) are relative to the N(^2D) + NO asymptote.

N_2O global minimum have been utilized for the calibration procedure, with the total rmsd being 0.940 kcal mol^{-1}.

4. FEATURES OF DMBE PES

Tables 4 and 5 compare the attributes of the stationary points of the DMBE PES with other theoretical and experimental results, having employed for the sake of comparison the labeling utilized in ref 15. In particular, we indicate the stationary-point geometries on the ground-state $^1A'$ PES that have been calculated through optimization searches of both minima (Ms) and transition states (TSs) at the MRCI(Q)/AVTZ level, employing analytic gradients. The results obtained by González et al.[15] at the CASPT2/6-311G(2d) level of theory and the analytical PES obtained from a fit to such points are also gathered in those two tables. The global minimum (M2) for the N_2O ground state is a linear (N−N−O) geometry in

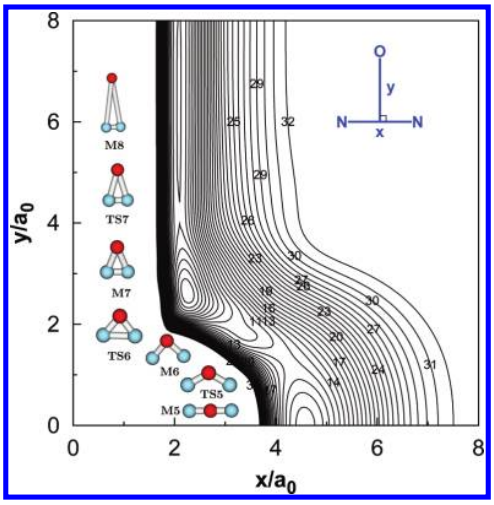

Figure 5. Contour plot for C_{2v} insertion of the O atom into the N_2 fragment. Contours equally spaced by 0.01 E_h, starting at −0.3427 E_h.

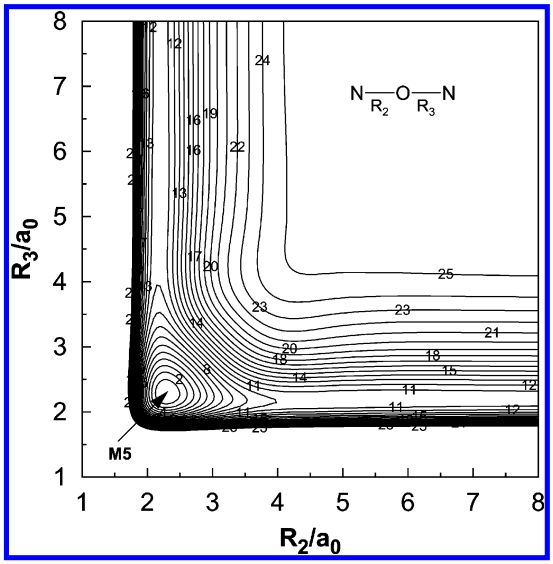

Figure 6. Contour plot for bond stretching in the N−O−N linear configuration. Contours equally spaced by 0.01 E_h, starting at −0.258 E_h.

dx.doi.org/10.1021/jp302173h | J. Phys. Chem. A 2012, 116, 4646−4656

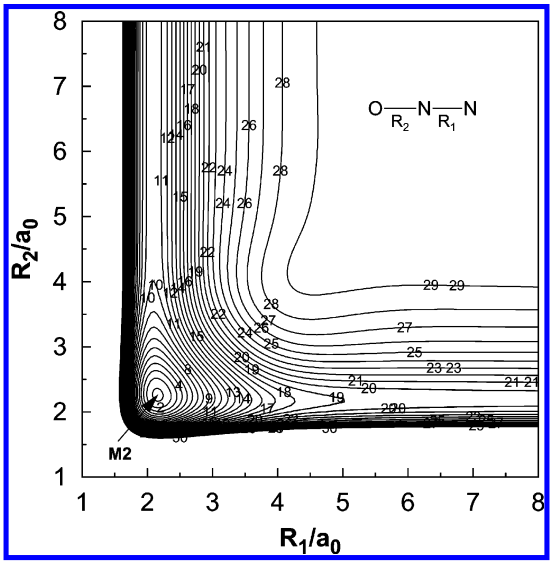

Figure 7. Contour plot for bond stretching in O−N−N collinear configuration. Contours equally spaced by 0.015 E_h, starting at −0.434 E_h.

our DMBE PES, which is predicated to be located at R_{NN} = 1.1399 Å and R_{NO} = 1.1928 Å and with a well depth of −174.69 and −89.63 kcal mol^{-1} relative to the $O(^1D)$ + $N_2(X^1\Sigma_g^+)$ and $N(^2D)$ + $NO(X\ ^2\Pi)$ dissociation energies, respectively. The energy differences with respect to the experimental data are 2.19 and 2.38 kcal mol^{-1}, relative errors less than 1.2% and 2.7%, respectively, in very good accordance with the experimental data. The existence of some of the reported minima has been noted previously; a linear NON minimum (M5) was confirmed and is well studied.[15,46,47] The present work yields for M5 a N−O distance of 1.2087 Å and a relative energy of −65.63 kcal mol^{-1}, in very good agreement with good-quality ab-initio data at the MRCI(Q)/AV*T*Z level of theory and other theoretical values. A cyclic-C_{2v} minimum (M7) in the ground state of N_2O is also reported in the present study as a more stable minimum than M5, with bond lengths of R_{NN} = 1.1891 Å and R_{NO} = 1.5145 Å and a relative energy of −117.65 kcal mol^{-1}. The above three isomers correspond therefore to a linear N−N−O structure as the global minimum with $C_{\infty v}$ symmetry, with the cyclic isomer having C_{2v} symmetry to be a local minimum lying 57.04 kcal mol^{-1} above the N−N−O global minimum and a linear N−O−N local minimum of $D_{\infty h}$ symmetry lying 109.06 kcal mol^{-1} higher than the global minimum and 52.02 kcal mol^{-1} above the cyclic C_{2v} one. Full agreement with other predictions is found insofar as the stability ordering of the three N_2O minima is concerned: NNO($C_{\infty v}$) > NON(C_{2v}) > NON($D_{\infty h}$). Many other minima and transition states found in the present work are also gathered in Tables 4 and 5 and compared with other theoretical predictions. As seen from Tables 4 and 5, the predicted values from our DMBE PES are in a good agreement with the stationary-point geometries obtained by optimization searches and other experimental and theoretical results.

In order to clarify the reactive mechanism, Figure 4 displays schematically the Ms and TSs predicted from the DMBE PES and their relative energies. Clearly, the reaction path is found to be in close agreement with previous work.[15] Several reactive paths can be distinguished from this plot. In the first path, the reacting N(^2D) atom attacks the N end of the NO molecule (M1) and evolves through the transition state TS1 and global minimum M2, then proceeding via a linear barrier (TS2) and minimum (M3) before dissociating to the products (route 1). The second path also occurs via M1 but with the N atom attacking the O end of the NO molecule and hence forming structures with NON connectivity. It evolves through the transition state TS3 to form a bent van der Waals structure (M4) which connects to a linear $D_{\infty h}$ one (M5) through a transition state (TS4) with a barrier of 3.01 kcal mol^{-1} relative to the reactants. Keeping C_{2v} symmetry, the oxygen atom then moves away from NN through a series of minima (i.e., M6, M7,

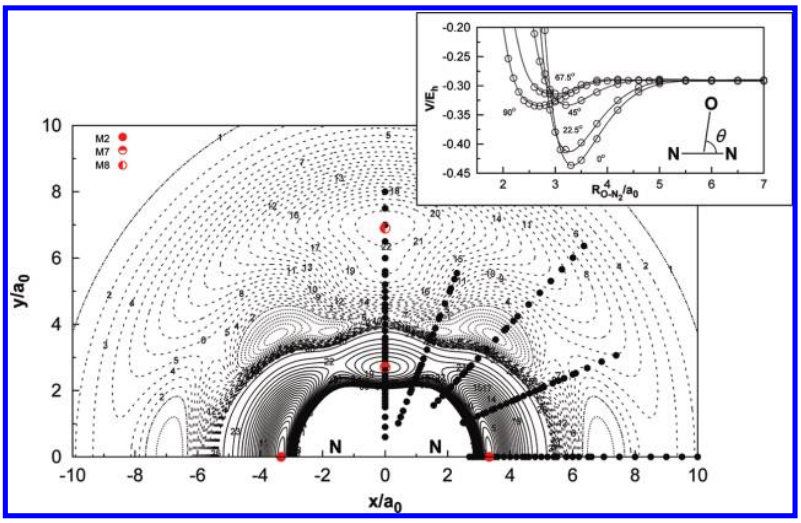

Figure 8. Contour plot for the O atom moving around a N_2 diatom fixed at its equilibrium geometry of R_{N_2} = 2.1410 a_0, which lies along the *x* axis with the center of the bond fixed at the origin. Contours are equally spaced by 0.006 E_h, starting at −0.4326 E_h. Dashed and dotted areas are contours equally spaced by −0.0001 and 0.0002 E_h, respectively, starting at −0.290 E_h. Also shown are the calculated ab-initio points for the O atom moving around N_2 diatomic, whose bond distance varied between 1.8 and 3.5 a_0. Shown at the insert are cuts along the atom−diatom radial coordinate for selected values of the Jacobi angle. Also indicated for clarity are the major minimal structures.

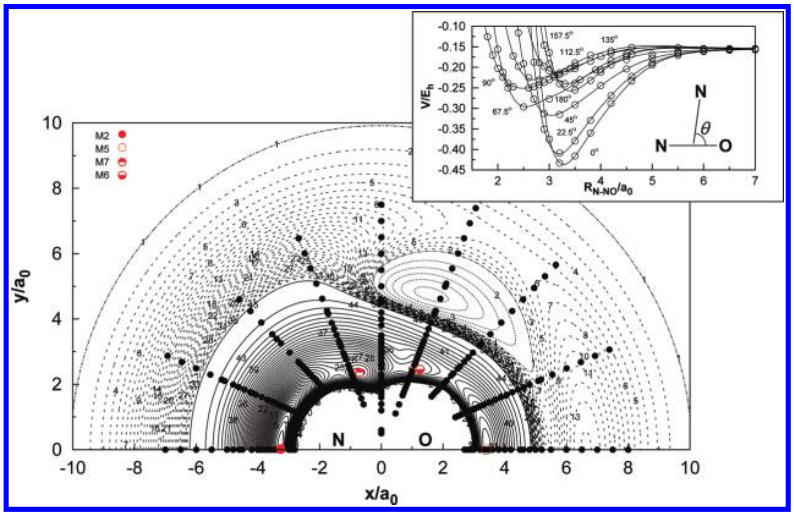

Figure 9. Contour plot for the N atom moving around a fixed NO diatom with the bond length fixed at R_{NO} = 2.2485 a_0, which lies along the x axis with the center of the bond fixed at the origin. Contours are equally spaced by 0.0062 E_h, starting at −0.4326 E_h. Dashed and dotted lines are contours equally spaced by −0.0002 and 0.001 E_h, respectively, starting at −0.15248 E_h. Also shown are the calculated ab-initio points for the N atom moving around NO diatomic, whose bond distance varied between 1.8 and 3.5 a_0. Insert shows cuts along the atom−diatom radial coordinate for selected values of the Jacobi angle. Minimal structures are also indicated for clarity.

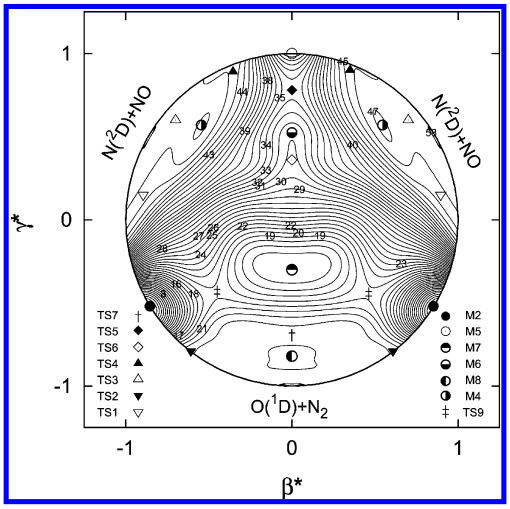

Figure 10. Relaxed triangular plot[49] in hyperspherical coordinates illustrating the location and symmetry of all stationary points discussed in the present work for ground-state N_2O.

and M8) and transition states (i.e., TS5, TS6 and TS7) before finally dissociating to products, $O(^1D)$ + $N_2(X^1\Sigma_g^+)$ (route 2). Connecting the above two paths, there is a C_s transition state, TS9. The third path starts in one of the above routes and ends on the other, forming $O(^1D)$ + $N_2(X^1\Sigma_g^+)$: it occurs through the global minimum (M2), transition state TS9 (with a barrier of 13.62 kcal mol^{-1} lower than TS2 in route 1), C_{2v} symmetry minimum M7, TS7 barrier, and minimum M8 to finally form the products (route 3).

Figures 5−9 show the major topographical features of the N_2O DMBE PES reported in the present work. The salient features from these plots are the most relevant stationary points for the title system, also characterized in Tables 4 and 5. As seen, all plots illustrate the smooth and correct behavior of the DMBE function for the ground-state N_2O species over its entire configuration space. In particular, Figure 5 shows a contour plot for the C_{2v} insertion of the $O(^1D)$ atom into N_2. It is visible from this plot that it reproduces the regions of the PES that link M8 and M5 through a series of transition states (i.e., TS7, TS6, and TS5) and minima (i.e., M7 and M6). When the O atom inserts into N_2, the ∠NON opens progressively while the distance of O to the center of N−N bond shortens and the bond length of N−N increases.

Figure 6 shows a contour plot for linear N−O−N stretch. The notable feature here is the linear N−O−N minimum (M5) located at R_{NO} = 1.2087 Å with an energy of 109.06 kcal mol^{-1} above of the global minimum of N_2O. In turn, Figure 7 illustrates in a clear manner the presence of the global minimum (M2). The predicted geometry is seen to agree nicely with the experimental results and with the PES reported by Schinke[18] which is based on MRCI calculations using the AVQZ basis set: the bond length differences are 0.0084 and 0.0031 Å, on the same order. The harmonic frequencies of the global minimum are 2253.3, 1314.1, and 453.6 cm^{-1}, with the MRCI(Q) results being 2283.9, 1298.8, and 600.3 cm^{-1}. In turn, the experimental values given by Warneck[48] are 2223.7, 1276.5, and 589.2 cm^{-1}, while the corresponding values reported by González et al.[15] at the CASPT2/6-311G(2d) level of theory and the analytical PES obtained from a fit to such points are 2223.7, 1269.6, and 589.5 cm^{-1} and 2216.3, 1250.2, and 589.7 cm^{-1} (respectively). As seen from Table 4, the results from the DMBE PES also show good agreement with the available estimates except, perhaps, for the bending frequency which is somewhat too small. Although this could possibly be improved by weigthing the points close to the minimum, no attempt has been made to do so since the experimental data refer to fundamentals rather than to harmonic frequencies.

Figure 8 shows a contour plot for the O atom moving around the N_2 ground-state diatom whose bond length is fixed at its equilibrium geometry of R_{NN} = 2.1410 a_0. The corresponding plot for the N atom moving around the NO diatom with its bond distance fixed at R_{NO} = 2.2485 a_0 is presented in Figure 9. The two plots clearly show a smooth behavior at both short- and long-range regions. From Figure 8 we can see the presence of minima (i.e., M2, M7, M8, M3) and transition states (i.e.,

TS7, TS9, TS2) according to dissociation routes 2 and 3 signaled above, see Figure 4. A transition state (TS9) is located between M2 and M7, corresponding basically to a stretched NNO structure which is located at R_{NN} = 1.1743 Å, R_{NO} = 1.4240 Å, and ∠NNO = 100.3° with an energy of 74.86 kcal mol^{-1} higher than the global minimum (M2) and 17.82 kcal mol^{-1} above M7. Also visible is the portion of the PES linking M8 to M7 minimum through the TS7 transition state, which corresponds to oxygen-atom insertion perpendicular to the N−N bond. Clearly, the trends mentioned when discussing Figure 4 are well reproduced. Also visible from this plot are TS2 and M3, which have linear geometries. Figure 9 shows the process connecting the linear ($C_{\infty v}$) NNO isomer to the cyclic (C_{2v}) and linear ($D_{\infty h}$) NON isomers, as indicated by M2 → TS9 → M7 → TS6 → M6 → TS5 → M5. In turn, Figures 8 and 9 illustrate the long-range parts of the PES which were fitted such as to provide a reliable description of the van der Waals minima and associated transition states.

All major topographical features of the PES are probably better viewed in a relaxed triangular plot[49] utilizing scaled hyperspherical coordinates ($\beta^* = \beta/Q$ and $\gamma^* = \gamma/Q$)

$$\begin{pmatrix} Q \\ \beta \\ \gamma \end{pmatrix} = \begin{pmatrix} 1 & 1 & 1 \\ 0 & \sqrt{3} & -\sqrt{3} \\ 2 & -1 & -1 \end{pmatrix} \begin{pmatrix} {R_1}^2 \\ {R_2}^2 \\ {R_3}^2 \end{pmatrix} \tag{24}$$

Figure 10 shows such a plot with all stationary points discussed above visible in it, thus allowing one to establish their connectivity in a more physical, multidimensional, way.

5. CONCLUDING REMARKS

A global single-sheeted DMBE PES has been reported for the ground state of N_2O from a least-squares fit to high-level AV*T*Z ab-initio energies, suitably corrected with the DMBE-SEC method. All topographical features have been carefully examined and compared with previously reported ones and experimental results when available. The DMBE PES here reported has been shown to be globally valid while fitting accurately all ab-initio points. A variety of minima and transition states has been predicted and various paths connecting reactants and products signaled. Good agreement is observed with previous high-quality theoretical studies and experimental data. The present single-sheeted DMBE PES should therefore be valuable for studying the dynamics and kinetics of reactions involving ground-state N_2O, work that is currently in progress.

■ ASSOCIATED CONTENT

Supporting Information

Parameters utilized to describe the DMBE potential-energy surface from this work and dispersion coefficients for the O−N_2 and N−NO channels as a function of the bond length of the diatomic. This material is available free of charge via the Internet at http://pubs.acs.org.

■ AUTHOR INFORMATION

Corresponding Author

*E-mail: varandas@qtvs1.qui.uc.pt.

Notes

The authors declare no competing financial interest.

■ ACKNOWLEDGMENTS

This work was financed by FEDER through Programa Operacional Factores de Competitividade-COMPETE and national funds under the auspices of Fundação para a Ciência e a Tecnologia, Portugal (projects PTDC/QUI-QUI/099744/2008, PTDC/AAC-AMB/099737/2008, and SFRH/BD/66471/2009).

■ REFERENCES

(1) Ravishankara, A. R.; Daniel, J. S.; Portmann, R. W. *Science* **2009**, *326*, 123.
(2) Remsen, L. G.; Pagel, M. A.; McCormick, C. I.; Fiamengo, S. A.; Sexton, G.; Neuwelt, E. A. *Anesth. Analg. (N.Y.)* **1999**, *88*, 559.
(3) Alm, J.; Saarnio, S.; Nykanen, H.; Silvola, J.; Martikainen, P. J. *Biogeochemistry* **1999**, *44*, 163.
(4) Rahn, T.; Zhang, H.; Wahlen, M.; Blake, G. A. *Res. Lett.* **1998**, *25*, 1189.
(5) Chakraborty, D.; Lin, M. C. *J. Phys. Chem. A* **1999**, *103*, 601.
(6) Maki, A. G.; Wells, J. S.; Vanek, M. D. *J. Mol. Spectrosc.* **1989**, *138*, 84.
(7) Teffo, J.-L.; Chendin, A. *J. Mol. Spectrosc.* **1989**, *135*, 389.
(8) Hishikawa, A.; Iwamae, A.; Hoshina, K.; Kono, M.; Yamanouchi, K. *Res. Chem. Intermed.* **1998**, *24*, 765.
(9) Brown, A.; Jimeno, P.; Balint-Kurti, G. G. *J. Phys. Chem. A* **1999**, *103*, 11089.
(10) Johnson, M. S.; Billing, G. D.; Gruodis, A.; Janssen, M. H. M. *J. Phys. Chem. A* **2001**, *105*, 8672.
(11) Nakamura, H.; Kato, S. *J. Chem. Phys.* **1999**, *110*, 9937.
(12) Varandas, A. J. C. *Adv. Chem. Phys.* **1988**, *74*, 255.
(13) Varandas, A. J. C. In *Lecture Notes in Chemistry*; Laganá Riganelli, A., Ed.; Springer: Berlin, 2000; Vol. *75*, pp 33.
(14) Varandas, A. J. C. *Conical Intersections: Electronic Structure, Spectroscopy and Dynamics*; Advanced Series in Physical Chemistry; World Scientific Publishing: Singapore, 2004; Chapter 5, p 91.
(15) González, M.; Valero, R.; Sayós, R. *J. Chem. Phys.* **2000**, *113*, 10983.
(16) Daud, M. N.; Balint-Kurti, G. G.; Brown, A. *J. Chem. Phys.* **2005**, *122*, 054305.
(17) Nanbu, S.; Johnson, M. S. *J. Phys. Chem. A* **2004**, *108*, 8905.
(18) Schinke, R. *J. Chem. Phys.* **2011**, *134*, 064313.
(19) Defazio, P.; Gamallo, P.; Petrongolo, C. *J. Chem. Phys.* **2012**, *136*, 054308.
(20) Werner, H. J.; Knowles, P. J. *J. Chem. Phys.* **1988**, *89*, 5803.
(21) Knowles, P. J.; Werner, H.-J. *Chem. Phys. Lett.* **1985**, *115*, 259.
(22) Marchetti, O.; Werner, H.-J. *Phys. Chem. Chem. Phys.* **2008**, *10*, 3400.
(23) Dunning, T. H., Jr. *J. Chem. Phys.* **1989**, *90*, 1007.
(24) Varandas, A. J. C. *J. Chem. Phys.* **1989**, *90*, 4379.
(25) Werner, H.-J.; Knowles, P. J.; Knizia, G.; Manby, F. R.; Schütz, M.; et al. *MOLPRO*, version 2010.1, a package of ab initio programs; University College Cardiff: Cardiff, UK, 2010.
(26) Murrell, J. N.; Carter, S. *J. Phys. Chem.* **1984**, *88*, 4887.
(27) Varandas, A. J. C.; Poveda, L. A. *Theor. Chem. Acc.* **2006**, *116*, 404.
(28) Varandas, A. J. C. *J. Chem. Phys.* **1996**, *105*, 3524.
(29) Varandas, A. J. C.; Silva, J. D. *J. Chem. Soc., Faraday Trans.* **1992**, *88*, 941.
(30) Varandas, A. J. C. *Mol. Phys.* **1987**, *60*, 527.
(31) Huber, K. P.; Herzberg, G. *Molecular Spectra and Molecular Structure Constants of Diatomic Molecules*; van Nostrand Reinhold: New York, 1979.
(32) Lodders, K. *J. Phys. Chem. Ref. Data.* **2004**, *33*, 357.
(33) Brown, F. B.; Truhlar, D. G. *Chem. Phys. Lett.* **1985**, *117*, 307.
(34) Varandas, A. J. C. *Chem. Phys. Lett.* **1992**, *194*, 333.
(35) Martnez-Núñez, E.; Varandas, A. J. C. *J. Phys. Chem. A* **2001**, *105*, 5923.
(36) Rodrigues, S. P. J; Sabn, J. A.; Varandas, A. J. C. *J. Phys. Chem. A* **2002**, *106*, 556.

(37) Varandas, A. J. C.; Rodrigues, S. P. J *J. Phys. Chem A* **006**, *110*, 485.
(38) Varandas, A. J. C.; Rodrigues, S. P. J *J. Phy. Chem. A* **2007**, *111*, 4869.
(39) Varandas, A. J. C. *J. Mol. Struct. (THEOCHEM)* **1988**, *166*, 59.
(40) Varandas, A. J. C.; Brandão, J.; Quintales, L. A. M. *J. Phys. Chem.* **1988**, *92*, 3723.
(41) Varandas, A. J. C.; C., A. A. C. *Pais, Mol. Phys.* **1988**, *65*, 843.
(42) Varandas, A. J. C.; Rodrigues, S. P. J *J. Chem. Phys.* **1997**, *106*, 9647.
(43) Rodrigues, S. P. J; Varandas, A. J. C. *Phys. Chem. Chem. Phys.* **2000**, *2*, 435.
(44) Varandas, A. J. C. In *Conferencias Plenarias de la XXIII Reunión Bienal de Qumica*; Feliciano, A. S., Grande, M., Casado, J., Eds.; Universidad de Salamanca: Salamanca, 1991; p 321.
(45) Martínez-Nuñez, E.; Varandas, A. J. C. *J. Phys. Chem.* **2001**, *105*, 5923.
(46) Peyerimhoff, S. D.; Buenker, R. J. *J. Chem. Phys.* **1968**, *49*, 2473.
(47) Wang, F.; Harcourt, R. D. *J. Phys. Chem. A* **2000**, *104*, 1304.
(48) Warneck, P. *Chemistry of the Natural Atmosphere*; Academic: San Diego, 1998.
(49) Varandas, A. J. C. *Chem. Phys. Lett.* **1987**, *138*, 455.
(50) Huber, K. P.; Herzberg, G. *Molecular Spectra and Molecular Structure. IV Constants of Diatomic Molecules*; Van Nostrand: New York, 1979.
(51) Bashkin, S.; Stoner, J. O., Jr. *Atomic Energy Levels and Grotrian Diagrams*; North-Holland: Amsterdam, 1975.

J. Phys. Chem. A 116, 4646-4656 (2012): SI.

Toward an accurate single-sheeted DMBE potential energy surface for the ground state of N_2O

Jing Li and António J. C. Varandas*[1]
Departamento de Química, Universidade de Coimbra

3004-535 Coimbra, Portugal

[1]Corresponding author: varandas@uc.pt

Table 1: Parameters in the switching functions.

Parameters	$f_1(\mathbf{R})$	Parameters	$f_{2,3}(\mathbf{R})$
α_1	0.632144	α_1	0.627059
α_2	0.685171	α_2	0.355785
β_1	1.59035	β_1	0.521073
β_2	0.268852	β_2	0.278026
R_1^{10}	1.65274	$R_{2,3}^{10}$	2.63604
R_1^{11}	3.98608	$R_{2,3}^{11}$	3.78884
R_1^{20}	2.8661	$R_{2,3}^{20}$	0.70132
R_1^{21}	4.74015	$R_{2,3}^{21}$	4.74172
α	0.75	α	0.75
r_1^0	5.5	$r_{2,3}^0$	5.5

Table 2: Parameters for two-body potential energy curves

.

Parameter	$N_2(X^1\Sigma_g^+)$	$NO(X^2\Pi)$
R_e/a_0	2.090857	2.190801
$D/\mathrm{E_h}$	0.705383	0.482145
$\alpha_1/\mathrm{a_0^{-1}}$	1.39496	1.46119
$\alpha_2/\mathrm{a_0^{-2}}$	-1.02806	-0.929602
$\alpha_3/\mathrm{a_0^{-3}}$	0.627289	0.840211
$\alpha_4/\mathrm{a_0^{-3}}$	-0.237656	-0.516115
$\alpha_5/\mathrm{a_0^{-3}}$	0.0418688	0.120291
$\gamma_0/\mathrm{a_0^{-1}}$	0.85959	0.922289
$\gamma_1/\mathrm{a_0^{-1}}$	1.7281	1.77394
$\gamma_2/\mathrm{a_0^{-1}}$	0.14546	0.225366
R_0/a_0	6.5780	6.1160
$C_6/\mathrm{E_h a_0^{-6}}$	24.10	18.78
$C_8/\mathrm{E_h a_0^{-8}}$	438.4155	305.3882
$C_{10}/\mathrm{E_h a_0^{-10}}$	10447.8275	6505.4914

Table 3: Numerical values (in atomic unit) of the parameters in Eq. (18).

	$C_6^0(R)$	$C_6^2(R)$	$C_8^0(R)$	$C_8^2(R)$	$C_8^4(R)$	$C_{10}^0(R)$
$O-N_2$						
R_M/a_0	3.5420	3.4783	3.5483	3.4879	3.4765	3.5522
D_M/E_h	44.363	5.7508	1684.5394	805.7889	63.0748	83794.8807
a_1/a_0^{-1}	1.19418998	-0.872172953	0.531898763	1.45365474	1.5986895	1.23751524
a_2/a_0^{-2}	0.204898558	0.238686556	-0.0004061	0.784568952	0.702606311	0.228397612
a_3/a_0^{-3}	0.00074840	0.00864448	-0.0223353	0.147548894	0.129022906	0.0016833
b_2/a_0^{-2}	0.435614640	0.512820625	0.334567520	0.871286483	0.512538430	0.491703448
b_3/a_0^{-3}	5.8×10^{-2}	3.1×10^{-9}	3.8×10^{-9}	3.7×10^{-9}	2.6×10^{-2}	7.3×10^{-2}
$N-NO$						
R_M/a_0	3.4000	3.3437	3.2932	3.3017	3.3074	4.2247
D_M/E_h	53.0984	7.4737	1827.0389	1176.5849	105.1093	192939.9868
a_1/a_0^{-1}	0.811851550	0.878344815	0.764321651	1.15666958	0.970437546	1.04109955
a_2/a_0^{-2}	-0.353046402	0.233889325	0.15085383	0.52621789	0.260198976	0.28356877
a_3/a_0^{-3}	-0.205365383	0.00098762	-0.01364140	0.02152999	-0.00166280	0.00010487
b_2/a_0^{-2}	0.359021660	0.585315550	0.557005836	1.16884594	0.08573123	0.16127091
b_3/a_0^{-3}	5.5×10^{-2}	2.3×10^{-9}	1.5×10^{-8}	$1.5 \times 10^{-8}/$	8.5×10^{-9}	9.5×10^{-3}

Table 4: Parameters and reference geometries of DMBE PES in the extended Hartree-Fock energy of Eq. (22).

Coefficients	$P^{(1)}$	$P^{(2)}$	$P^{(3)}$	$P^{(4)}$	$P^{(5)}$
$\gamma_1^{(j)}/\mathrm{a}_0^{-1}$	1.4	1.4	0.2	4.0	1.2
$\gamma_2^{(j)}/\mathrm{a}_0^{-1}$	-0.4	1.1	1.2	1.9	0.4
$\gamma_3^{(j)}/\mathrm{a}_0^{-1}$	1.1	-0.4	1.2	1.9	0.4
$R_1^{(j),\mathrm{ref}}/\mathrm{a}_0$	2.15	2.15	2.5	3.5	2.301
$R_2^{(j),\mathrm{ref}}/\mathrm{a}_0$	4.40	2.25	2.795	2.58	2.89
$R_3^{(j),\mathrm{ref}}/\mathrm{a}_0$	2.25	4.40	2.795	2.58	2.89

Table 5: Numerical values of DMBE PES in the extended Hartree-Fock energy of Eq.(22).

Coefficients	$P^{(1)}+P^{(2)}$	$P^{(3)}$	$P^{(4)}$	$P^{(5)}$
c_1/a_0^0	-3.5381946851	4.2007705945	0.0356238663	-3.0904118697
c_2/a_0^{-1}	1.1147692480	0.2915958413	0.1145327539	0.5811321195
c_3/a_0^{-1}	-2.4169129261	-3.4039542773	-0.0387539965	1.0816793893
c_4/a_0^{-2}	-1.2194551980	2.0052856021	0.0526697633	-0.6531757544
c_5/a_0^{-2}	-0.8568452569	2.7891224317	0.0782002792	-1.5109866892
c_6/a_0^{-2}	1.1788575352	-3.4288441158	0.3606665227	-4.0911284424
c_7/a_0^{-2}	1.5395730981	0.5439425584	0.0747798103	1.7988380874
c_8/a_0^{-3}	0.3883857578	-0.2621186302	0.0070033708	0.0627874792
c_9/a_0^{-3}	-0.4353418403	1.4062128004	0.1815351093	-0.3051320738
c_{10}/a_0^{-3}	0.1085413585	0.2273765814	0.0416226946	-0.0123575759
c_{11}/a_0^{-3}	-0.9180817925	-1.1467328245	1.0236679403	0.2247887270
c_{12}/a_0^{-3}	-0.3073234676	-1.0966219283	0.2256294349	0.1360338601
c_{13}/a_0^{-3}	-1.7972734487	-1.6047871173	-0.1101845374	-0.4602862578
c_{14}/a_0^{-4}	-0.1733211752	0.2228173913	-0.0199225836	0.0129253221
c_{15}/a_0^{-4}	-0.0595522418	0.1201076356	0.6954514708	0.0783571071
c_{16}/a_0^{-4}	-0.1920075644	0.8726739942	-0.0903584476	0.1959991238
c_{17}/a_0^{-4}	-0.3502524369	-0.4126742359	-0.1375295487	-0.0818758063
c_{18}/a_0^{-4}	0.0601423454	-0.5064526814	0.5630773626	0.0332283833
c_{19}/a_0^{-4}	0.5353895120	-0.7804908148	-0.1383547308	-0.0113571881
c_{20}/a_0^{-4}	0.0492156480	-0.7528712442	-0.3189359859	0.2128147790
c_{21}/a_0^{-4}	-0.6622178856	0.4388360013	0.0846829992	-0.1123859239

Table 6: Numerical values of DMBE PES in the extended Hartree-Fock energy of Eq.(22).

Coefficients	$P^{(1)}+P^{(2)}$	$P^{(3)}$	$P^{(4)}$
c_{22}/a_0^{-4}	0.1853772400	0.5650993683	-0.0890235678
c_{23}/a_0^{-5}	0.0372207808	0.0923923973	0.1222965174
c_{24}/a_0^{-5}	-0.2058526833	0.6058375503	1.0882935948
c_{25}/a_0^{-5}	0.0117308843	0.4453015587	-0.1175408941
c_{26}/a_0^{-5}	-0.3528079953	-0.2937705252	-0.2722566085
c_{27}/a_0^{-5}	0.1170883883	0.1937185636	-0.0823859957
c_{28}/a_0^{-5}	-0.1513298537	-0.5121361904	-0.1790544334
c_{29}/a_0^{-5}	0.1323336610	-0.3934528961	-0.4048532161
c_{30}/a_0^{-5}	0.0098216808	-0.6733875421	-0.1019237044
c_{31}/a_0^{-5}	-0.2032874082	0.3733306369	0.0658370911
c_{32}/a_0^{-5}	0.0553877097	0.1930920784	-0.1029215397
c_{33}/a_0^{-5}	-0.4287246833	-0.2655241031	0.1952959107
c_{34}/a_0^{-5}	0.1523304117	0.2250341468	0.0763029527
c_{35}/a_0^{-6}	0.0032165816	0.0033091534	0.0884242435
c_{36}/a_0^{-6}	0.0657009132	0.1339181959	0.5359292097
c_{37}/a_0^{-6}	-0.0798326369	0.1511443309	-0.1418253741
c_{38}/a_0^{-6}	0.0744811100	-0.0470482574	-0.0170352328
c_{39}/a_0^{-6}	0.0142436675	0.0213821443	-0.0339485728
c_{40}/a_0^{-6}	0.1145171169	0.0415298209	0.1050835689
c_{41}/a_0^{-6}	-0.0277242436	0.0270569992	-0.0113488202
c_{42}/a_0^{-6}	0.0576751475	-0.0559392579	-0.3425367353
c_{43}/a_0^{-6}	-0.0381269462	-0.0847208105	-0.1533812770
c_{44}/a_0^{-6}	-0.0163948123	-0.3166690352	0.1069963535
c_{45}/a_0^{-6}	-0.0556135384	0.0675235838	0.0433358444
c_{46}/a_0^{-6}	-0.0864453614	-0.0888476353	0.0033996661
c_{47}/a_0^{-6}	-0.0983578155	-0.1134057749	0.1820241036
c_{48}/a_0^{-6}	0.1167603512	0.0629810638	0.0813457448
c_{49}/a_0^{-6}	-0.0071857986	-0.0189224912	-0.0519404966
c_{50}/a_0^{-6}	0.2882458560	-0.0021512042	-0.0149811090

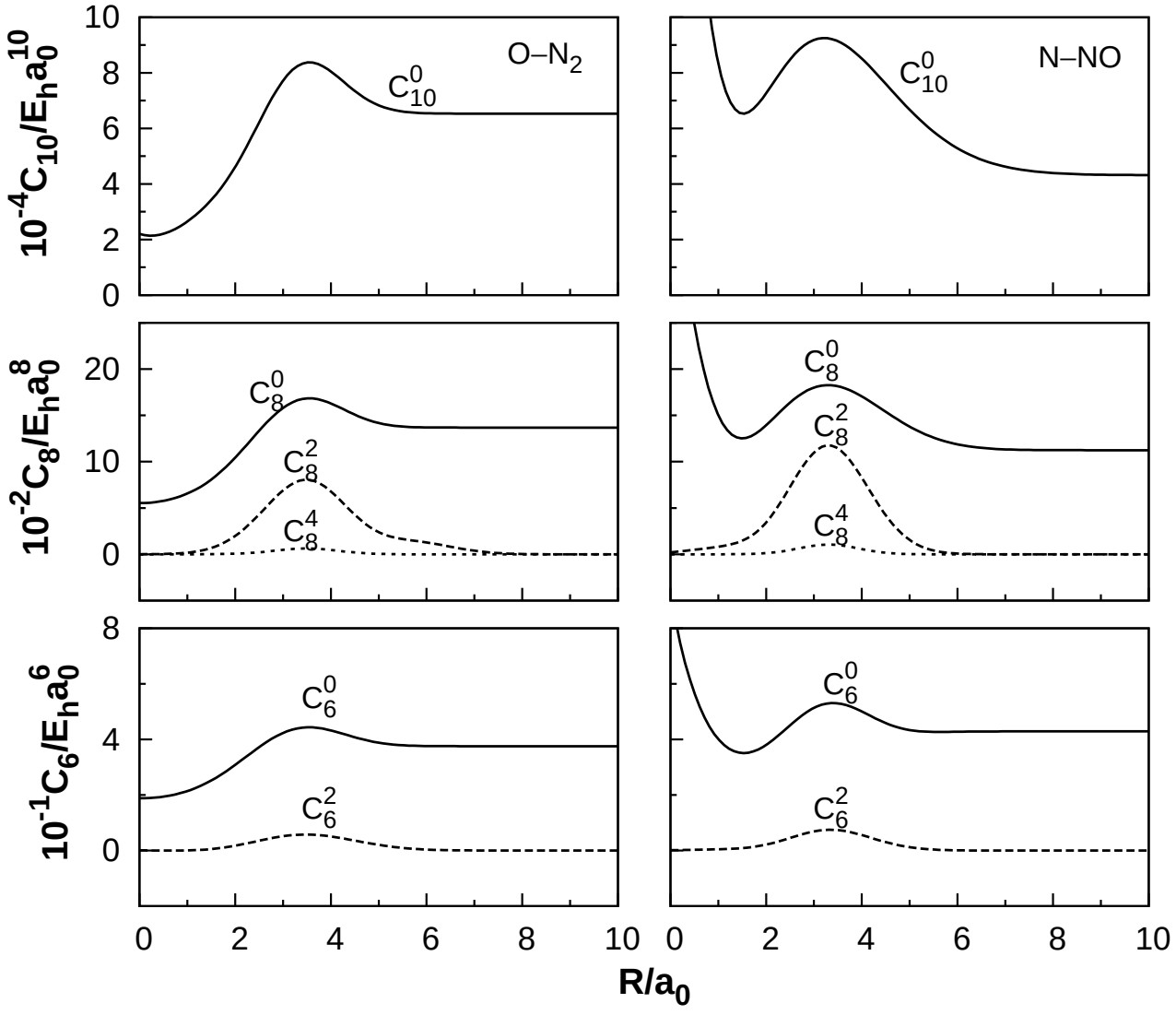

Figure 1: Dispersion coefficients for the atom-diatom asymptotic channels of N_2O as a function of this corresponding internuclear distance of diatom.

THE JOURNAL OF PHYSICAL CHEMISTRY A

Article

pubs.acs.org/JPCA

Quasiclassical Trajectory Study of the Atmospheric Reaction $N(^2D)$ + $NO(X\ ^2\Pi) \rightarrow O(^1D) + N_2(X\ ^1\Sigma_g^+)$

Jing Li,[†] Pedro J. S. B. Caridade,[†] and António J. C. Varandas[†,*]

[†]Departamento de Química, Universidade de Coimbra, 3004-535 Coimbra,Portugal

[‡]Centro de Química, Universidade de Coimbra, 3004-535 Coimbra, Portugal

ABSTRACT: Quasiclassical trajectories have been run for the title atmospheric reaction over the range of temperatures $5 \leq T/\mathrm{K} \leq 3000$ on a recently proposed single-sheeted double many-body expansion (DMBE) potential energy surface for ground-state $N_2O(^1A')$. As typical in a capture-like reaction, the rate constant decreases with temperature for $50 \leq T/\mathrm{K} \leq 800$ K, while showing a small dependence at higher temperature regimes. At room temperature, it is predicted to have a value of $(20.1 \pm 0.2) \times 10^{-12}$ cm^3 s^{-1}. The calculated cross sections show a monotonic decay with temperature and translational energy. Good agreement with the experimental data has been observed, providing more realistic rate constants and hence support of enhanced accuracy for the DMBE potential energy surface with respect to other available forms.

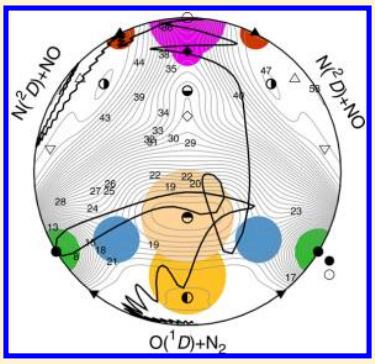

1. INTRODUCTION

Interest in the N_2O system has been increasing in recent years due to its key role in the ozone-depleting process.[1] In particular, the $N(^2D,^4S)$ + NO reactions and dynamics have been the subject of much theoretical and experimental work due to their role in environmental issues.[2−9] Specifically, the reaction of $N(^2D)$ with NO is a good prototype in collisional dynamics, as demonstrated by the many experimental measurements of the thermal rate constant for the total removal of $N(^2D)$ by NO at 300 K.

There are several energetically accessible processes for the $N(^2D)$ + NO collisional process at room temperature:

$$N_a(^2D) + N_bO(X^2\Pi) \rightarrow O(^3P) + N_2(X^1\Sigma_g^+) \quad \Delta E = -132.30\ \mathrm{kcal\ mol^{-1}} \tag{1}$$

$$\rightarrow O(^1D) + N_2(X^1\Sigma_g^+) \quad \Delta E = -86.87\ \mathrm{kcal\ mol^{-1}} \tag{2}$$

$$\rightarrow O(^1S) + N_2(X^1\Sigma_g^+) \quad \Delta E = -35.68\ \mathrm{kcal\ mol^{-1}} \tag{3}$$

$$\rightarrow N_a(^2D) + N_bO(X^2\Pi) \tag{4}$$

$$\rightarrow N_b(^2D) + N_aO(X^2\Pi) \tag{5}$$

where the subscripts a and b label the two nitrogen atoms. Processes 1−3 lead to formation of atomic oxygen in the fundamental or excited states, with the N_2 fragment left in its ground electronic state. Reactions 4 and 5 represent instead inelastic/elastic processes, and the exchange reaction of atomic nitrogen, respectively. Other important processes are those that involve the $^2D/^4S$ electronic quenching of the nitrogen atom (ΔE = 56.39 kcal mol^{-1}), but these are out of the scope of the present work.

The previous *ab initio* studies by Hopper[10] and Donovan and Husain[11] provided a detailed overview of the low-lying excited state potential energy surfaces (PESs) for the title system. From a total of 20 PESs [5($^1A'$), 5($^1A''$), 5($^3A'$), and 5($^3A''$)] which adiabatically correlate with reactants in C_s symmetry, there are 3($^1A'$) and 2($^1A''$) PESs correlating with products for reaction 2, while only $^3A''$ and $^1A'$ PESs are associated with reactions 1 and 3, respectively. Furthermore, the existence of five adiabatic PESs involved in reaction 2 suggests that this exothermic process should significantly contribute to the $N(^2D)$ total removal rate constant.

Reaction 2 is important in both atmospheric and combustion processes because it is a source of highly reactive oxygen atoms in the first excited state.[12] However, only a few experimental kinetic studies are available dealing with the thermal rate constant for the total removal of $N(^2D)$ by NO at 300 K. The earlier determination by Black et al.[13] analyzed the transient measurements of NO (β) emission to give the rate coefficients for removal of $N(^2D)$ by several simple molecules, which predicted a rate constant of $(180 \pm 50) \times 10^{-12}$ cm^3 s^{-1}. In 1971, the line absorption technique was applied by Lin and Kaufman[14] to the kinetic study of the metastable atomic nitrogen $N(^2D)$ in a flowing afterglow system. Their measurements led to a rate constant at room temperature of $(70 \pm 25) \times 10^{-12}$ cm^3 s^{-1}. Husain et al. obtained values of[15] $(61 \pm 37) \times 10^{-12}$ cm^3 s^{-1} and[16] $(59 \pm 4) \times 10^{-12}$ cm^3 s^{-1} using a fast flow technique. In turn, the lowest value of $(35 \pm 3) \times 10^{-12}$ cm^3 s^{-1}

Received: August 24, 2013
Revised: January 28, 2014
Published: January 30, 2014

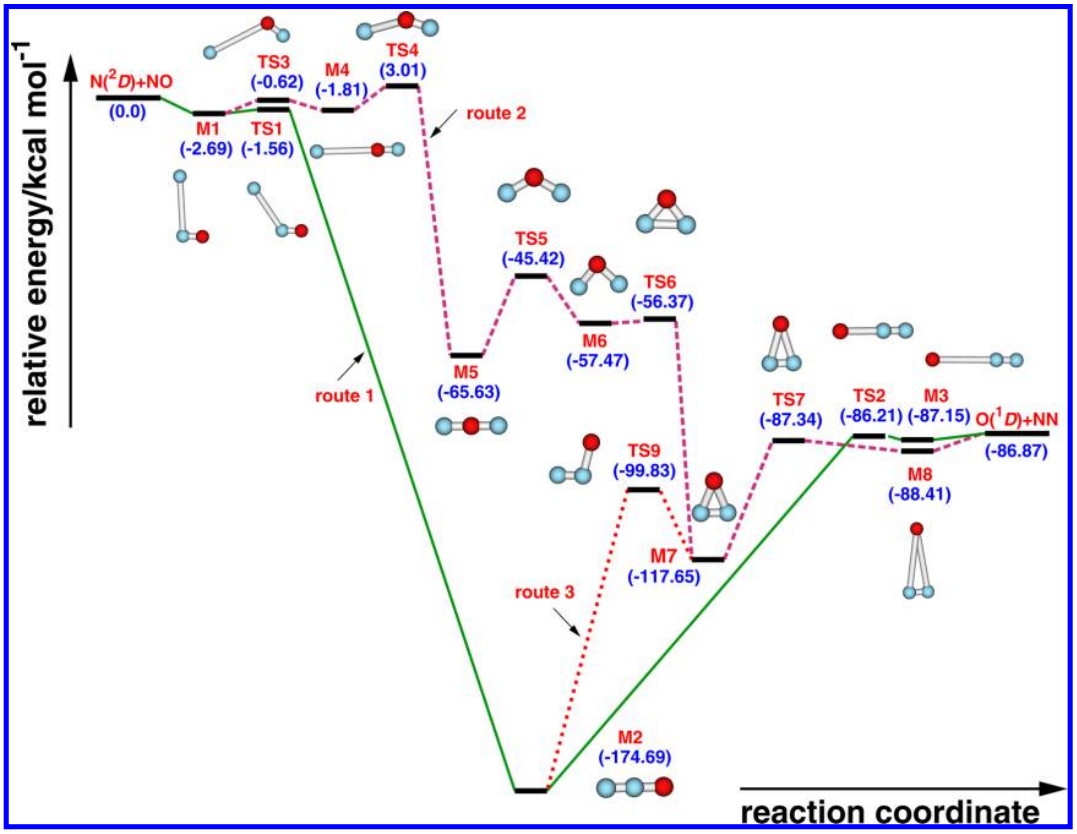

Figure 1. Energy diagram of the stationary points located on the DMBE PES. Energies are given relative to the N(^2D) + NO asymptote (in kcal mol^{-1}). The existence of several reaction pathways through which the system can evolve along the $^1A'$ PES has been shown in terms of the labeled routes 1 (drawn in green solid line), 2 (indicated in dark-pink dashed line), and 3 (links routes 1 and 2, shown in red dotted line).

reported by Sugawara et al.[17] using the pulse-radiolysis technique for measurement of the quenching rates of the metastable nitrogen atom, ^2D and ^3P in both nitrogen and helium, has been attributed to a flaw in their method of obtaining the NO partial pressure. Not surprisingly, therefore, the recommended room temperature rate constant, 60×10^{-12} cm^3 s^{-1}, is based on the data of Lin and Kaufman,[14] Husain et al.,[15,16] and Umemoto et al.[18] Although there is no certainty on the formed product states in such studies,[11] the reaction most likely leads to formation of $N_2(X\ ^1\Sigma_g^+)$ + O(^3P,^1D,^1S), which thence forms atomic oxygen in all allowed electronic states.

The N_2O system for the first singlet $^1A'$ has been extensively studied both experimental and theoretically. However, for the PES of the N_2O molecule, the majority of structural studies focused on its global minimum, with this information being also of relevance for the reaction of concern. Theoretical studies of nitrous oxide date back to the first two-dimensional PESs calculated by Brown et al.[19] with the NN bond length kept fixed at the experimental value of 1.1282 Å, which predicted a well depth of −80.41 kcal mol^{-1} relative to O(^1D) + $N_2(X\ ^1\Sigma_g^+)$, thence within 8% of the experimental dissociation energy of −87.25 kcal mol^{-1} and which has been subsequently used by Johnson et al.[20] in dynamics calculations. Improved electronic structure calculations have been performed later by Daud et al.[21] using the complete-active-space self-consistent field (CASSCF) and the multireference configuration interaction (MRCI) electronic structure methods, still keeping the NN bond fixed at the equilibrium value. At the same time, Nanbu and Johnson[22] reported full three-dimensional PESs and employed them in dynamics calculations. Schinke[23] calculated the ground state PESs, which show a minimum of −85.63 kcal mol^{-1} for a linear NNO structure, and used them for wave packet dynamics.[24−26] However, theoretical studies of the N(^2D) + NO($X\ ^2\Pi$) reactions are very scarce, with González et al.[27] being the only authors to make an extensive theoretical study of the N(^2D) + NO($X\ ^2\Pi$) → O(^1D) + $N_2(X\ ^1\Sigma_g^+)$ exothermic reaction. The resulting PES (heretofore denoted GRR PES) has been employed for quasi-classical trajectory (QCT) calculations, and obtained a value of $(2.63 \pm 0.07) \times 10^{-12}$ cm^3 s^{-1} at room temperature, thus largely underestimating the total experimental rate constant.

The present study has a dual purpose: first, to test the accuracy of our recently proposed double many-body expansion[28−30] (DMBE) PES for the title system[31] based on MRCI(Q)[32,33] (multireference configuration interaction including the Davidson correction) energies, using the aug-cc-pVTZ (AVTZ) basis set of Dunning;[34,35] second, to improve our understanding of the results for the rate constant and cross sections within the QCT dynamical approach here employed. State-specific QCT cross sections and thermalized rate constants have therefore been calculated using the newly reported N_2O ($^1A'$) DMBE PES.[31] The paper is structured as follows. Section 2 gives a brief survey of the PES and utilized computational methods, while the results and discussion are in section 3. The concluding remarks are summarized in section 4.

dx.doi.org/10.1021/jp408487y | J. Phys. Chem. A 2014, 118, 1277−1286

2. CALCULATION DETAILS

2.1. Potential Energy Surface. Dynamics calculations have been performed previously on a many-body expansion[36] (MBE) PES constructed by González et al.[27] for the ground state ($^1A'$) of N_2O. They performed CASSCF electronic structure calculations, followed by second-order perturbation theory calculations using the CASSCF wave function as reference (CASPT2). Both studies employed the standard Cartesian 6-311G(2d) basis set of Pople and co-workers,[37,38] predicting a well depth of −170.9 kcal mol^{-1} relative to the N(^2D) + NO($X\ ^2\Pi$) dissociation limit.

In this work we have employed the global single-sheeted DMBE PES that we have recently reported based on a least-squares fit to a set of high level MRCI(Q)/AVTZ *ab initio* energies, which have been suitably corrected using the DMBE-scaled external correlation[39] (DMBE-SEC) method. A total of 809 points covering a range of energy up to ∼500 kcal mol^{-1} above the N_2O global minimum have been used for the calibration procedure, with the total rmsd being 0.940 kcal mol^{-1}. One of the most important properties of the DMBE PES is the proper description of the long-range forces, which, in this case, are of major relevance for the N(^2D) + NO reaction. Since this DMBE PES has been described in detail elsewhere, the reader is directed elsewhere[31] for a more detailed description.

The global minimum of ground-state N_2O has a linear (N−N−O) geometry, which in the DMBE PES here utilized is predicted to be located at R_{NN} = 1.1399 Å, and R_{NO} = 1.1928 Å, with a well depth of −174.69 kcal mol^{-1} and −89.63 kcal mol^{-1} relative to the N(^2D) + NO($X\ ^2\Pi$) and O(^1D) + N_2($X\ ^1\Sigma_g^+$) dissociation channels, respectively. The energy differences with respect to the experimental data are of 2.19 kcal mol^{-1} and 2.38 kcal mol^{-1}, with relative errors smaller than 1.2% and 2.7% (respectively), thence in very good accordance with the experimental data. Figure 1 displays the minima and transition states predicted on the DMBE PES and their relative energies. From this plot, several reactive paths can be distinguished in terms of the routes labeled 1, 2, and 3, with the most likely minimum energy path for the title reaction being via N(^2D) atom attack to the N end of the NO molecule (M1), through the transition state TS1, then evolving through the global minimum (M2), the linear barrier (TS2), and the minimum M3, and finally dissociating to products (route 1).

Figure 2 shows a relaxed triangular plot[40] utilizing the reduced hyperspherical coordinates $\beta^* = \beta/Q$ and $\gamma^* = \gamma/Q$:

$$\begin{pmatrix} Q \\ \beta \\ \gamma \end{pmatrix} = \begin{pmatrix} 1 & 1 & 1 \\ 0 & \sqrt{3} & -\sqrt{3} \\ 2 & -1 & -1 \end{pmatrix} \begin{pmatrix} R_1^2 \\ R_2^2 \\ R_3^2 \end{pmatrix} \tag{6}$$

Besides illustrating in a single plot all important topographical features of the PES, such a plot can also be used to visualize the trajectories run.[41] An example of a short-lived reactive trajectory is actually shown there by the wigly line. The colored circles indicate regions utilized for the assignment of reactive trajectories to passage over specific stationary points.

2.2. Quasiclassical Trajectory Calculations. All dynamics calculations here reported have utilized the QCT method, which is widely described in the literature.[42] The classical equations of motion have been integrated using a time step of 0.2 fs, such as to warrant conservation of the total energy within

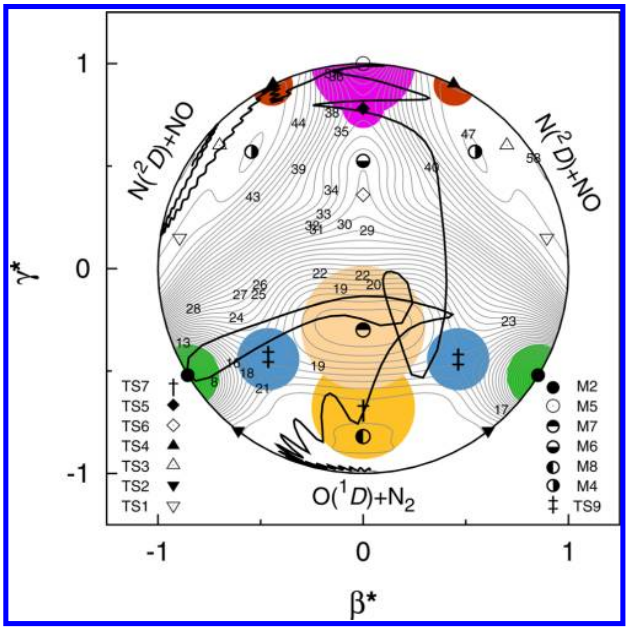

Figure 2. Relaxed triangular plot in hyperspherical coordinates illustrating the location and symmetry of all stationary points located on the DMBE PES. The circles in different colors refer to the estimation of the reactive trajectories passing the certain stationary point. Juxtaposed on this plot as the solid line is a short-lived reactive trajectory.

0.01 kcal mol^{-1} or smaller, with the reactants initially separated by 19 Å. All remaining dynamical parameters have been obtained by the standard QCT procedure. The reactive cross section for the state-specific (v = 0, j = 1) can be calculated using the traditional expression

$$\sigma_r(E_{tr};\ v = 0, j = 1) = \pi b_{\max}^2 \frac{N_r}{N} \tag{7}$$

with the 68% statistical uncertainty being given by $\Delta\sigma_r = \sigma_r[(N - N_r)/(NN_r)]^{1/2}$. The symbols have their usual meaning: N_r is the total number of reactive trajectories out of a set of N integrated ones, and b_{max} is the maximum impact parameter for the reaction, which has been determined in the traditional way.[42] The state-specific rate constant is then given by averaging the cross section over the translation energy

$$k_{vj}(T) = g_e(T)\left(\frac{8k_BT}{\pi\mu_{N+NO}}\right)^{1/2}\left(\frac{1}{k_BT}\right)^2 \int_0^\infty E_{tr}\sigma_r \times \exp\left(-\frac{E_{tr}}{k_BT}\right) dE_{tr} \tag{8}$$

where μ_{N+NO} is the reduced mass of the reactants, and k_B the Boltzmann constant. Because the dynamics is performed adiabatically on the $^1A''$ state, the electronic degeneracy factor assumes the form

$$g_e(T) = q_{N_2O}(T)\ q_{N(^2D)}^{-1}(T)\ q_{NO(^2\Pi)}^{-1}(T) \tag{9}$$

with the electronic partition functions accounting for the fine-structure of N(^2D) and NO($^2\Pi$):

$$q_{N_2O} = 1 \tag{10}$$

dx.doi.org/10.1021/jp408487y | J. Phys. Chem. A 2014, 118, 1277−1286

$$q_{N(^2D)}(T) = 6 + 4\exp(-12.53/T) \quad (11)$$

$$q_{NO(^2\Pi)}(T) = 2 + 2\exp(-177.1/T) \quad (12)$$

The thermal rate constant can be obtained by averaging the internal states of the NO molecule and translational energy:

$$k(T) = g_e(T)\left(\frac{2}{k_BT}\right)^{3/2}\left(\frac{1}{\pi}\right)^{1/2} Q_{vj}^{-1}(T)\sum_{vj}(2j+1) \times \exp\left(-\frac{E_{vj}}{k_BT}\right)\int_0^\infty E_{tr}\sigma^x \exp\left(-\frac{E_{tr}}{k_BT}\right) dE_{tr} \quad (13)$$

where $Q_{vj}(T)$ the rovibrational partition function and E_{vj} the (v,j) state energy. The cumulative function of the translation energy sampling assumes the form.[42,43] $E_{tr} = k_BT\ln(\xi_1\xi_2)$, where ξ_i are freshly generated random numbers (see elsewhere[44] for an alternative scheme).

For a realistic sampling of the internal states of the NO diatomic, the method described in ref 45 has been adopted. It starts with the cumulative rovibrational Boltzmann distribution

$$C(v,j;T) = \sum_{v'=0}\sum_{j'=1}(2j'+1)\exp(-E_{v',j'}/k_BT)Q_{v'j'}^{-1}(T) \quad (14)$$

where $Q_{vj}(T)$ is the rovibrational partition function for all the states of NO($X\ ^2\Pi$), with the rovibrational energies calculated by solving the nuclear Schrödinger equation for the diatomic fragment.[46] Note that the sum in eq 14 is over rovibrational states, thus avoiding the traditional energy partitioning into vibrational and rotational components. For each temperature, the (v, j) state is sampled via eq 14 when the condition $C(v,j;T) \geq \xi_3$ is satisfied for a freshly generated random number, ξ_3.

For vibrational state-specific calculations, eq 14 is also used by summing only the rotational states for a fixed v, and $Q_{vj}^{-1}(T)$ is the rotational partition function for that specific vibrational state. The thermal rate constant is then obtained as

$$k(T) = g_e\left(\frac{8k_BT}{\pi\mu_{N+NO}}\right)^{1/2}\pi b_{max}^2\frac{N_r}{N} \quad (15)$$

with the corresponding error being given by $\Delta k(T) = k(T)[(N - N_r)/(NN_r)]^{1/2}$. A total of 10^5 trajectories have been run for T = 300 K, and 10^4 for the other temperatures, which were considered sufficient to obtain a low statistical deviation for all the studied properties.

3. RESULTS AND DISCUSSION

3.1. Rate Constants. As pointed out in the Introduction, experimental information on the studied reaction is scarce, referring only to the total N(^2D) + NO($X\ ^2\Pi$) rate constant at room temperature (around 300 K). Thus, a direct comparison between the calculated and experimental rate constants is not free of some ambiguity. Table 1 compares the calculated rate constants at room temperature with the total removal of N(^2D) by NO and the calculated QCT result. To a first approximation on accounting for the total reactivity of the system, the ground-state $^1A'$ will yield a value of $k(300) = (20.1 \pm 0.2) \times 10^{-12}$ cm^3 s^{-1} at room temperature. Such a result yields only about one-third of the experimental rate constant, $k = 60 \times 10^{-12}$ cm^3 s^{-1} for the total reaction in N(^2D) + NO($X\ ^2\Pi$).

Table 1. Rate Constants for the N(^2D) + NO($X\ ^2\Pi$) at Room Temperature ($T \approx 300$ K)

source	year	method	$k/10^{-12}$ cm^3 s^{-1}
Black et al.[13]	1969	FP-CL	180 ± 50
Lin and Kaufman[14]	1971	DF-RA	70 ± 25
Husain et al.[15]	1972	FP-RA	61 ± 37
Husain et al.[16]	1974	FP-RA	59 ± 4.0
Sugawara et al.[17]	1980	PR-RA	35 ± 3.0
Fell et al.[47]	1990	LP-LIF	67 ± 13
Umemoto et al.[18]	1998	LP-LIF	82.7 ± 2.9
González et al.[27]	2000	QCT	2.63 ± 0.07
this work	2012	QCT	20.3 ± 0.1

As stated in the Introduction, the total experimental rate constant is a sum of the rate constants of every process that can be responsible for the depletion of N(^2D), with the reaction almost certainly forming $N_2 + O(^3P,^1D,^1S)$. Indeed, there are 1 ($2^3A''$), 5[$1^1A'$, $2^1A'$, $3^1A'$, $1^1A''$, and 2 $^1A''$] and 1 (4 $^2A'$) PESs that correlate with products for reactions 1, 2, and 3, respectively. González et al.[27] have tried to take into account the reactivity due to the other four excited PESs connecting with products. They calculated the energies of these states with an equally weighted state-average over the states considered in selected points of an approximation barrier in the entrance NNO channel using the CASPT2 method, and they reported that at least the two first 1 $^1A'$ PESs, whose barriers are below 1 kcal mol^{-1}, would contribute significantly to reactivity at a temperature of 300 K. Briefly, they concluded that the rate constant for reaction 2 could reasonably be within the range 2.6 $\times 10^{-12}$ cm^3 s^{-1} with $1^1A'$ contribution to 7.9 $\times 10^{-12}$ cm^3 s^{-1}, if a similar contribution of the $1^1A'$, $2^1A'$ PESs to the total rate constant were assumed. In particular, the ground state $1^1A'$ with a deep well which is barrierless for the linear abstraction mechanism in reaction 2 suggests that this exothermic reaction should furnish an important contribution to the N(^2D) total removal rate constant. Clearly, our result is reasonable and substantially larger (about 8 times) than the QCT result obtained from the MBE PES.[27] Such a difference may be explained due to the fact that the DMBE potential energy surface is based on a set of MRCI(Q)/AVTZ *ab initio* energies, which have been suitably corrected using the DMBE-scaled external correlation (DMBE-SEC) method. It shows a well depth of −174.69 kcal mol^{-1} and −89.63 kcal mol^{-1} relative to the N(^2D) + NO($X\ ^2\Pi$) and O(^1D) + $N_2(X\ ^1\Sigma_g^+)$ dissociation channels, respectively, which amount to energy differences more attractive than the experimental values by only 2.19 kcal mol^{-1} and 2.38 kcal mol^{-1}. Note that the PES of ref 27 is based on second-order perturbation theory calculations using the CASSCF wave function as reference (CASPT2) with the standard Cartesian 6-311G(2d) basis set: it has a well depth of −170.9 kcal mol^{-1}, with the N(^2D) + NO($X\ ^2\Pi$) dissociation limit lying higher than the experimental value by 1.6 kcal mol^{-1}. Another important feature of the DMBE PES concerns the proper description of long-range forces which are critical for a quantitative description of the title reaction.

Table 3 summarizes the thermally averaged rate constants for the N(^2D) + NO($X\ ^2\Pi$) reaction. The calculations cover the range of temperatures from 5 to 3000 K, with a total of 10 000 trajectories being integrated for each temperature. Figure 3 compares the calculated rate constants vs temperature with the experimental and previous QCT results. As inferred from Figure 3, the results of the title reaction can be divided into two

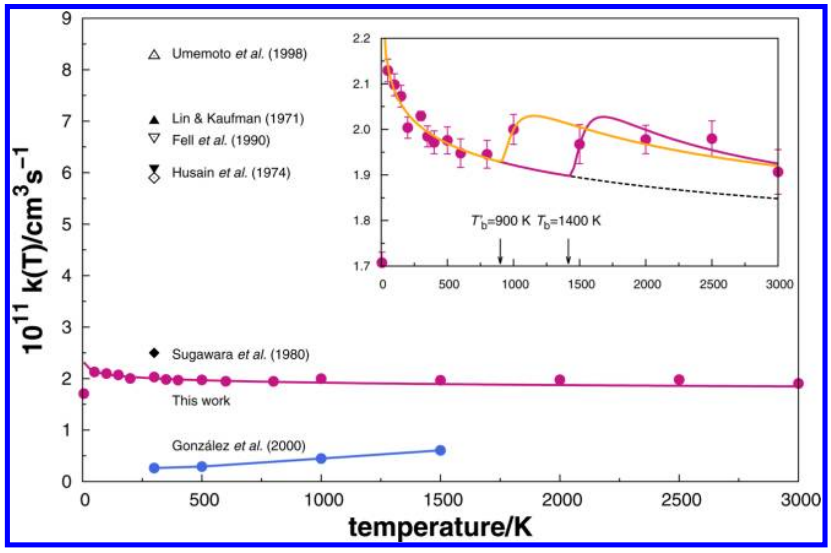

Figure 3. Rate constant for the $N(^2D) + NO(X\ ^2\Pi) \rightarrow O(^1D) + N_2(X\ ^1\Sigma_g^+)$ reaction as a function of temperature. The open circle symbols refer to the QCT calculations, while the solid curves through the data correspond to the best least-squares fits of eq 12. The fits are shown as a blue solid line and a red dashed line with T_b fixed at 900 and 1400 K, and the black dotted line corresponds to the fit of capture type eq 13 (see inset). Also shown are results reported by González et al. and the experimental values for the total removal of $N(^2D)$ by NO.

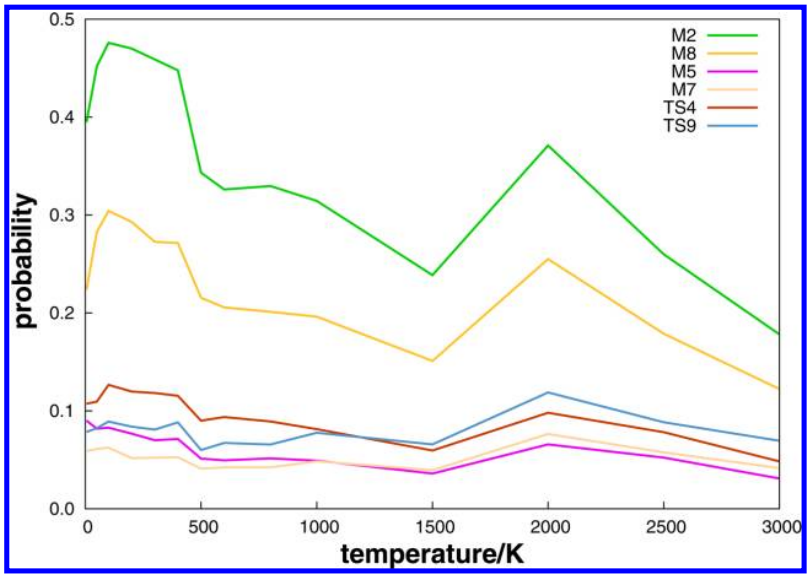

Figure 4. Reaction probability that may be approximately ascribed to various stationary points as a function of temperature.

parts. At low temperatures (from 50 to 800 K) the rate constant of reaction 2 decreases with T, as is typical of a capture-like reaction, while at 1000 K it increases and then decreases again until 3000 K although showing only a small dependence on the temperature. To model the calculated rate constants, we have therefore employed the composite form,

$$k(T) = k_{cap}(T) + k_b(T) \tag{16}$$

where k_{cap} accounts for the rate constants due to capture of a nitrogen atom from NO and k_b is a rate constant that is operative at high temperatures after overcoming the barrier in the entrance channel. As an aid to classify the different types of rate constants, we have employed the forms[48]

$$k_{cap}(T) = g_e(T)\left[\frac{2^{(3n-4)/2n} n\pi^{1/2}}{(n-2)^{(n-2)/n}\mu^{1/2}} \times \Gamma\left(\frac{2n-2}{n}\right)(k_B T)^{(n-4)/2n} C_n^{2/n}\right] \quad (T < T_b) \tag{17}$$

$$k_b(T) = g_e(T) A (T - T_b)^m \exp[-B/(T - T_b)] \quad (T \geq T_b) \tag{18}$$

leading to optimum least-squares parameters of $n = 3.74$, $C_n = 1.69\ E_h a_0^n$, and $A = 6.41 \times 10^{-9}$ K^{-m} cm^3 s^{-1}, $B = 221.11$ K, $m = -0.7093$ for T_b fixed at 1400 K, while $A' = 1.35 \times 10^{-9}$ K^{-m} cm^3 s^{-1}, $B' = 117.31$, $m' = -0.4959$ for T_b fixed at 900 K.

As Figure 3 shows, the above fit mimics the calculated rate constant over the entire range of temperatures considered in

dx.doi.org/10.1021/jp408487y | J. Phys. Chem. A 2014, 118, 1277−1286

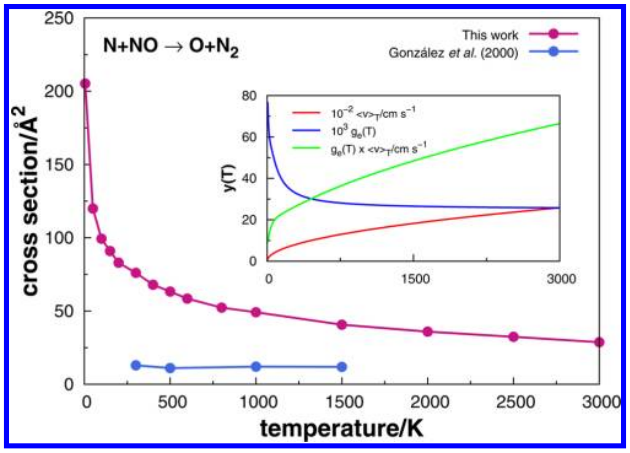

Figure 5. Cross section (Å^2) for the reaction N(^2D) + NO($X\ ^2\Pi$) → O(^1D) + N$_2$($X\ ^1\Sigma_g^+$) as a function of temperature. Also shown are $g_e(T)$ with the same form in eq 15, $\langle v\rangle_T = (8k_BT/\pi\mu_{N+NO})^{1/2}$, and $g_e(T)\langle v\rangle_T$.

Table 2. QCT Cross Sections for N(^2D) + NO($X\ ^2\Pi$) Reaction as a Function of Collision Energy

	N$_2$ + O				N-exchange		
E_{tr}/eV	b_{max}/Å	$100P_r$	σ_r/Å^2	$100\Delta\sigma_r$/Å^2	$100P_r$	σ_r/Å^2	$100\Delta\sigma_r$/Å^2
0.1	7.1	79.9	126.5	89.8	4.8	7.5	47.7
0.3	6.5	75.6	100.3	80.6	4.8	6.4	40.1
0.5	6.2	73.5	88.8	75.3	2.7	3.3	27.8
1.0	5.8	67.7	71.5	69.9	2.3	2.5	22.5
1.5	5.6	63.2	62.3	67.2	2.8	2.7	22.9
2.0	5.4	61.8	56.6	63.0	3.0	2.7	22.0
3.0	5.2	57.7	49.0	59.3	3.2	2.7	21.2
4.0	5.0	56.9	44.7	55.0	2.8	2.2	18.4
5.0	4.8	56.4	40.8	50.8	3.3	2.4	18.3
7.0	4.6	54.5	36.2	46.8	2.9	2.0	15.9
8.0	4.5	54.4	34.6	44.8	2.7	1.7	14.6
10.0	4.3	54.4	31.6	40.9	3.0	1.7	14.6

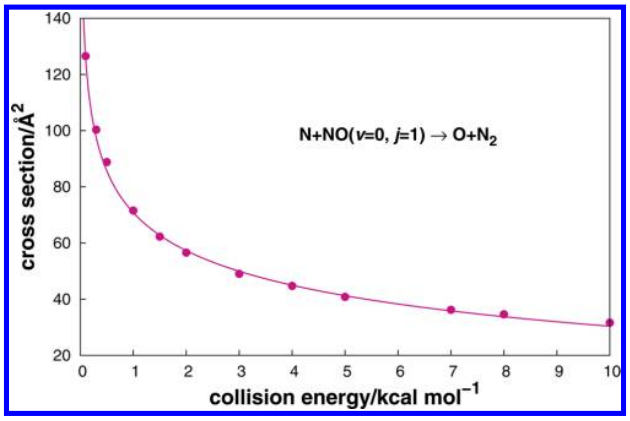

Figure 6. Estimated state-specific cross section (Å^2) for the reaction N(^2D) + NO(v = 0,j = 1) as a function of the collision energy.

the present work, with the threshold temperature fixed at T_b = 1400 K and T_b' = 900 K. Within the T range between 50 and 800 K, the rate constant changes from (21.3 ± 0.3) to (19.5 ± 0.3) × 10^{-12} cm^3 s^{-1}. The analysis for reaction at low temperature ($T < T_b$, T_b') indicates that most of the trajectories only traverse TS1, heading for the NNO minimum and dissociating to the products (see Figure 1 of route 1). At higher temperatures, the rate constant increases to (20.0 ± 0.3) × 10^{-12} cm^3 s^{-1} at 1000 K and then decreases to (19.1 ± 0.5) × 10^{-12} cm^3 s^{-1} at the highest temperature considered: T = 3000 K. There is a significant enhancement of the other reaction pathways: despite the magnitude of the entrance barriers, the N(^2D) atom could attack the NO oxygen side, leading to products through the reaction pathway route 2 (shown in Figure 1). Note that in fit I the threshold temperature has been fixed at 900 K, corresponding to a barrier value of 1.79 kcal mol^{-1} excluding the zero-point energy (ZPE) correction, and mimics all points. A fit II has been carried out where the T_b was fixed at 1400 K, passes through a maximum as the temperature increases, and then decreases at a rate determined by the parameter m, while the point at 1000 K was omitted in this fit procedure. Moreover, at the lowest temperature explored, the rate constant goes down to (17.1 ± 0.2) × 10^{-12} cm^3 s^{-1}. This may be attributed to the following mechanistic interpretation: although the magnitude of the entrance barrier facilitates an attack of the N(^2D) atom to the nitrogen side of its counterpart NO, traversing TS1 with a barrier of −1.56 kcal mol^{-1} and heading for the global minimum, in some trajectories the N(^2D) atom could attack the oxygen side of NO, proceeding to reaction pathway route 2, then returning to TS1, evolving through the global minimum to the products at a very low temperature. Also shown in Figure 3 are the experimental and theoretical data from the literature. As noted above, our results are more realistic and much larger than the QCT values obtained by González et al.[27] but, unlike the latter, show a near invariance with temperature in the covered range.

We have tried to account for the probabilities of the reactive trajectories passing via specific stationary points (or regions associated with them, as indicated by the colored circles in Figure 2), with the results being shown in Figure 4. As noted above, the calculated probabilities are in accordance with the rate constant as a function of temperature. The calculated probabilities show a decrease with increasing temperature at temperatures less than T_b, present a small peak at T = 2000 K, and attain the largest value when passing through the global minimum M2. This may be explained by noting that most reactive trajectories follow route 1 by forming a collision complex close to collinear NNO structures at low temperatures, while at high temperatures the trajectories can overcome the barrier and eventually evolve through less attractive regions of the PES, such as the ones involving bent NNO structures. Note also that the reaction probability involving TS4 and M4 is also significant. Indeed, N(^2D) may evolve through route 2, and even interchange routes.

3.2. Cross Sections. The calculated thermal cross sections for reaction 2 are reported in Table 3 and represented in Figure 5. For a given temperature and using the rovibrational and translational energy samplings of the previous section, a thermal cross section may be defined as $\sigma(T) = \pi b_{max}^2 N_r/N$, in which N_r is the number of reactives out of a batch of N trajectories. As seen, the reaction cross section decreases with T from 5 to 3000 K, with a sharp decrease from (205 ± 3) Å at 5 K to (120 ± 1) Å^2 at 50 K. More generally, it decreases monotonically over a wide range of temperature (T = 100−3000 K), namely from (99 ± 1) to (28.7 ± 0.7) Å^2. We analyzed various contributions of eq 15 (see the inset), with the term $\langle v\rangle_T = (8k_BT/\pi\mu_{N+NO})^{1/2}$, making a major contribution to such an unusual behavior in such a manner that the largest cross section turns out to yield the lowest rate constant at 5 K;

Table 3. Summary of the QCT Results for the $N(^2D)$ + $NO(X\ ^2\Pi)$ Reaction[a]

	N_2 + O			N-exchange			
T/K	b_{max}/Å	N_r[b]	σ_r/Å^2	$10^{12}k(T)$/ cm^3 s^{-1}	N_r[b]	σ_r/Å^2	$10^{13}k(T)$/ cm^3 s^{-1}
5	13.6	3531	205 ± 3	17.1 ± 0.2	231	13.4 ± 0.9	11.2 ± 0.7
50	9.5	4230	120 ± 1	21.3 ± 0.3	220	6.2 ± 0.4	11.1 ± 0.7
100	8.6	4276	99 ± 1	20.9 ± 0.3	192	4.5 ± 0.3	9.4 ± 0.7
150	8.2	4305	91 ± 1	20.7 ± 0.3	152	3.2 ± 0.3	7.3 ± 0.6
200	7.9	4230	83 ± 1	19.9 ± 0.3	123	2.4 ± 0.2	5.8 ± 0.2
300	9.2	28612	76.1 ± 0.4	20.3 ± 0.1	752	2.0 ± 0.1	5.3 ± 0.2
300[c]	6.0		12.9 ± 0.2	2.63 ± 0.04		0.023 ± 0.011	
400	7.5	3843	67.9 ± 0.9	19.7 ± 0.3	117	2.1 ± 0.2	6.0 ± 0.6
500	8.1	3068	63 ± 1	19.8 ± 0.3	72	1.5 ± 0.2	4.6 ± 0.5
500[c]	5.13		11.07 ± 0.3	2.92 ± 0.08		0.010 ± 0.005	
600	8.2	2766	58.4 ± 0.9	19.5 ± 0.3	60	1.3 ± 0.2	4.2 ± 0.5
800	7.6	2882	52.3 ± 0.8	19.5 ± 0.3	88	1.6 ± 0.2	5.9 ± 0.6
1000	7.6	2707	49.1 ± 0.8	20.0 ± 0.3	71	1.3 ± 0.2	5.3 ± 0.6
1000[c]	4.59		12.03 ± 0.28	4.48 ± 0.11		0.25 ± 0.04	
1500	8.6	1748	40.6 ± 0.9	19.7 ± 0.4	62	1.4 ± 0.2	7.0 ± 0.9
1500[c]	4.47		11.89 ± 0.29	6.06 ± 0.12		0.37 ± 0.04	
2000	6.3	2878	35.9 ± 0.6	19.8 ± 0.3	159	2.0 ± 0.2	10.9 ± 0.9
2500	7.1	2047	32.4 ± 0.6	19.8 ± 0.4	140	2.2 ± 0.2	14 ± 1
3000	8.3	1325	28.7 ± 0.7	19.1 ± 0.5	110	2.4 ± 0.2	16 ± 1

[a]Reaction channel: $N_a(^2D)$ + $N_bO(X\ ^2\Pi)$ → $O(^1D)$ + $N_2(X\ ^1\Sigma_g^+)$ (2) and $N_a(^2D)$ + $N_bO(X\ ^2\Pi)$ → $N_b(^2D)$ + $N_aO(X\ ^2\Pi)$. [b]100 000 trajectories calculated at 300 K and 10 000 otherwise. [c]QCT results from ref 27.

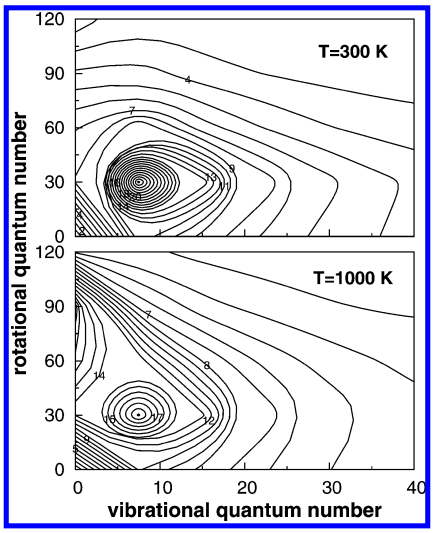

Figure 7. Comparison of the rovibrational distribution of the products of the title reaction on DMBE PESs for T = 300 and 1000 K. The lines are the probability contours starting at 0 and space by 0.00002.

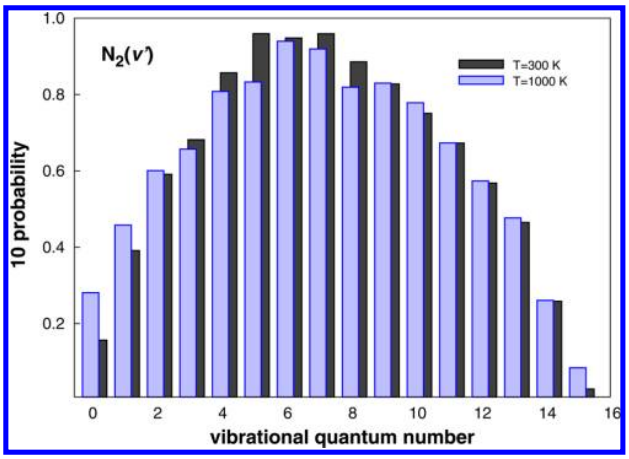

Figure 8. Total vibrational distribution for product N_2 in the N + $NO(\nu, j = 1)$ reaction under different temperatures: solid line, T = 300 K; dashed line, T = 1000 K.

see ref 49 for a similar pattern for the O + OH reaction. Also indicated for comparison in Figure 5 are the theoretical results by González et al.[27] Their smaller values do not show any obvious temperature-dependence, being 6 times smaller than ours.

The dependence of the state-specific cross section of reaction 2, as a function E_{tr} for the $NO(v = 0,j = 1)$ reaction, is given in Table 2 and shown in Figure 6. To model the collision energy dependence of the calculated cross sections, we have employed the form

$$\sigma(E_{tr}) = a + bE_{tr}^{n} \quad (19)$$

with optimum parameters being defined as follows: a = −79.6 Å^2, b = 150.4 Å^2(kcal mol^{-1})$^{-n}$, and n = −0.136. Note that the value of b_{max} increases with decreasing translation energy while for higher translation energies it is essentially constant or slightly increases with E_{tr}. A similar behavior has been described elsewhere for OH + O_2 reaction.[50] Thus, we expect N_2O formation to be dictated in the present case by a capture-type mechanism where long-range forces play an important role. Such a dependence of b_{max} on E_{tr} may therefore be rationalized as follows: the dominant contribution for the interaction between $N(^2D)$ and $NO(X\ ^2\Pi)$ arises from the long-range electrostatic term[51−53] involving the quadrupole moment of atomic nitrogen and the dipole moment of NO, and also the quadrupole moment of N and the quadrupole moment of NO. Since the NO stretching leads to an increase of its electric quadrupole moment, it may then be expected to yield a more attractive long-range interaction. This may explain why b_{max} increases with decreasing translation energy. Conversely, for high translation energy, long-range forces should be less

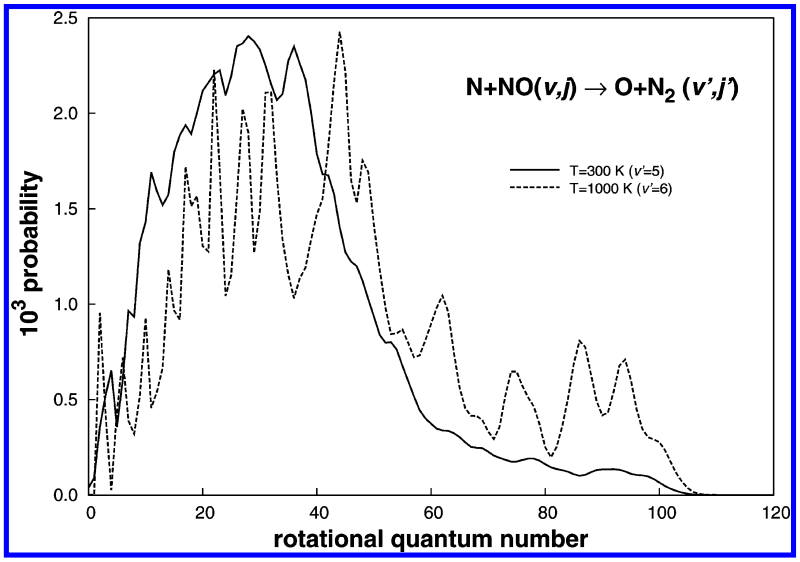

Figure 9. Comparison for the rotational distribution of the most populated N_2 vibrational state $\nu' = 5$, $\nu' = 6$ for $T = 300$ and 1000 K, respectively.

important for reaction, leading only to a small decrease in b_{max}. In summary, the cross sections of reaction 2 strongly decrease with E_{tr} in the 0.1−1 kcal mol^{-1} range, with a gradual stabilization then occurring until the cross section becomes nearly independent of E_{tr} above 5 kcal mol^{-1}.

Additional calculations of the N-exchange reaction (eq 5) have also been carried out, with the results being reported in Tables 2 and 3. The results show that the rate constant decreases with T between 5 and 200 K and then increases from 300 to 3000 K. A significant contribution of the N-exchange reaction is therefore expected at high temperatures. In turn, the cross sections of the N-exchange reaction decrease with translation energy while, for high temperatures, they become essentially constant or manifest a slight decrease with E_{tr}.

3.3. Rovibrational Product Analysis. The analysis of vibrational and rotational distribution for the newly formed N_2 on the DMBE PES has been studied by the momentum Gaussian-binning (shortly MGB) method.[54] Briefly, the probability of a rovibrational state (υ,j) is given by

$$P_{\upsilon j} = \sum_{i=1}^{N} \frac{W_{\upsilon j}^{i}}{N_r} \tag{20}$$

where $W_{\upsilon j}^{i} \sim W_{\upsilon}^{i} W_{j}^{i}$ and

$$W_{k}^{i} = \frac{1}{\rho k \sqrt{\pi}} \exp\left[-\left(\frac{\sqrt{E_k} - \sqrt{\epsilon_k^i}}{\rho k \sqrt{\bar{E}_k}} \right)^2 \right] \tag{21}$$

where E_k is the kth diatomic energy eigenvalue, $\bar{E}_k$ is an average separation between neighboring levels, and ϵ_k^i is the final energy of the ith trajectory (vibrational or rotational). The separation of the internal energy is carried out using the standard procedure;[42] that is, after the end of trajectory is reached, 200 circles are used to obtain the rotational energy while vibrational energy is obtained by the difference with the internal energy. It should be noted that the MGB differs slightly from the GB,[55] as suggested by the theory. In fact, the weights should reflect a squared Gaussian dependence on the displacements from the square-root of the energy of a given contributing state to the supposedly known classical value (viewed as the centroid of the relevant quantum distribution).[54]

Figure 7 shows a contour for the state-specific probabilities as a function of the product's rovibrational level for $T = 300$ K and $T = 1000$ K. As it can be seen, the highest probability occurs for $\upsilon' = 8$ and $j' = 29$ for $T = 300$ K, whereas for $T = 1000$ K it displays a broader bimodal distribution centered at $\upsilon' = 8$ and $\upsilon' = 0$. Figure 8 compares the vibrational distributions obtained from the MGB scheme for $T = 300$ K and $T = 1000$ K. The results show only small differences, with a peak at $\upsilon' = 5$ for $T = 300$ K, while, for the larger temperature $T = 1000$ K, the peak is at $\upsilon' = 6$, as expected for an exothermic reaction. Significant differences arise, though in the corresponding vibrationally specific rotational distributions. This is illustrated in Figure 9, which corresponds to the maximum populated vibrational states, $\upsilon' = 5$ and $\upsilon' = 6$. It presents a peak at about $j' = 25$ and $j' = 41$, at $T = 300$ K and $T = 1000$ K, respectively. By checking the probability of the rotational states for each of the temperatures calculated for the title system, we have found that, at $T = 300$ K, the probability for the $j' = 0$−41 levels lies higher than that for $T = 1000$ K obtained for their corresponding υ' state. This relation is inverted when $j' > 41$ until the probability goes to 0.

4. CONCLUDING REMARKS

In spite of its importance, the title multichannel reaction has only a few theoretical studies so far due to lack of realistic PESs. Our motivation in this work has been to cover this gap and hence initiate a series of studies using a DMBE PES for the ground state of N_2O that we have recently proposed.[31] Specifically, we have carried out a QCT study of the rate constant for the $N(^2D)$ + $NO(X\ ^2\Pi)$ reaction, with the prediction that only a relatively small variation is expected over a wide temperature range (50−3000 K). We have reported cross sections as a function of the translation energy, which depicted the following behavior: the cross section increases with decreasing translation energy at low collision energies while for higher ones σ becomes essentially constant or just slightly increases with E_{tr}. Extensive comparisons with previous experimental and theoretical predictions have also been

performed, with the results showing a higher reactivity than others available in the literature. An improved agreement with the experimental results has therefore been obtained, even though there are large experimental uncertainties. Since nitrous oxide is known to be important in the chemistry of both the atmosphere[8] and combustion[7] with many reactions occurring on the potential energy surface studied in the present work (and others, some under investigation in our group), we hope that the present study may help with rationalization of the observed data.

AUTHOR INFORMATION

Corresponding Author

*E-mail: varandas@uc.pt.

Notes

The authors declare no competing financial interest.

ACKNOWLEDGMENTS

This work was financed by FEDER through Programa Operacional Factores de Competitividade-COMPETE and national funds under the auspices of Fundação para a Ciência e a Tecnologia, Portugal (Projects PTDC/QEQ-COM/3249/2012, PTDC/AAG-MAA/4657/2012, and SFRH/BD/66471/2009).

REFERENCES

(1) Ravishankara, A. R.; Daniel, J. S.; Portmann, R. W. Nitrous Oxide (N_2O): The Dominant Ozone-Depleting Substance Emitted in the 21st Century. *Science* **2009**, *326*, 123−125.

(2) Phillips, L. F.; Schiff, H. I. Mass Spectrometric Studies of Atom Reactions. 1. Reactions in the Atomic Nitrogen-Ozone System. *J. Chem. Phys.* **1962**, *36*, 1518.

(3) Husain, D.; Slater, N. K. H. Kinetic Study of Ground State Atomic Nitrogen, $N(2^4S_{3/2})$, by Time-Resolved Atomic Resonance Fluorescence. *J. Chem. Soc., Faraday Trans II* **1980**, *76*, 606−619.

(4) Cheah, C. T.; Clyne, M. A. A. Reactions Forming Electronically-excited Free Radicals Part 2. Formation of N^4S, N^2D and N^2P Atoms in the H + NF_2 Reaction, and N Atom Reactions. *J. Chem. Soc., Faraday Trans II* **1980**, *76*, 1543−1560.

(5) Gilibert, M.; Aguilar, A.; González, M.; Mota, F.; Sayós, R. Dynamics of the $N(^4S_u)$ + $NO(X\ ^2\Pi)$ → $N_2(X\ ^1\Sigma_g^+)$ + $O(^3P_g)$ Atmospheric Reaction on the $^3A''$ Ground Potential Energy Surface. I. Analytical Potential Energy Surface and Preliminary Quasiclassical Trajectory Calculations. *J. Chem. Phys.* **1992**, *97*, 5542−5553.

(6) Herron, J. T. Evaluated Chemical Kinetics Data for Reactions of N^2D, N^2P, and $N_2(A^3\Sigma_u^+)$ in the Gas Phase. *J. Phys. Chem. Ref. Data* **1999**, *28*, 1453−1483.

(7) Dean, A. M.; Bozzelli, J. W. In *Gas-Phase Combustion Chemistry*; Gardiner, J. W. C., Ed.; Springer: New York, 2000; pp 125−341.

(8) Wayne, R. P. *Chemistry of Atmospheres*, 3rd ed.; Oxford University Press: 2000.

(9) Gamallo, P.; Martínez, R.; Sayós, R.; González, M. Quasiclassical Dynamics and Kinetics of the N + NO → N_2 + O,NO + N Atmospheric Reactions. *J. Chem. Phys.* **2010**, *132*, 144304.

(10) Hopper, D. G. *Ab initio* Multiple Root Optimization MCSCF Study of the $C_{\infty v}/C_s$ Excitation Spectra and Potential Energy Surfaces of N_2O. *J. Chem. Phys.* **1984**, *80*, 4290−4316.

(11) Donovan, R. J.; Husain, D. Recent Advances in the Chemistry of Electronically Excited Atoms. *Chem. Rev.* **1970**, *70*, 489−516.

(12) Brouard, M.; Duxon, S. P.; Enriquez, P. A.; Simons, J. P. The Stereochemistry of the $O(^1D)$ + N_2O → NO + NO Reaction via Velocity-aligned Photofragment Dynamics. *J. Chem. Phys.* **1992**, *797*, 7414−7422.

(13) Black, G.; Slanger, T. G.; John, G. A. S.; Young, R. A. Vacuum-Ultraviolet Photolysis of N_2O. IV. Deactivation of $N(^2D)$. *J. Chem. Phys.* **1969**, *51*, 116−121.

(14) Lin, C.; Kaufman, F. Reactions of Metastable Nitrogen Atoms. *J. Chem. Phys.* **1971**, *55*, 3760−3770.

(15) Husain, D.; Kirsch, L. J.; Wiesenfeld, J. R. Collisional Quenching of Electronically Excited Nitrogen Atoms, $N(2^2D_J,2^2P_J)$ by Time-resolved Atomic Absorption Spectroscopy. *Faraday Discuss. Chem. Soc.* **1972**, *53*, 201.

(16) Husain, D.; Mitra, S. K.; Young, A. N. Kinetic Study of Electronically Excited Nitrogen Atoms, $N(2^2D_J,2^2P_J)$, by Attenuation of Atomic Resonance Radiation in the Vacuum Ultra-violet. *J. Chem. Soc., Faraday Trans. 2* **1974**, *70*, 1721−1731.

(17) Sugawara, K.; Ishikawa, Y.; Sato, S. The Rate Constants of the Reactions of the Metastable Nitrogen Atoms, ^2D and ^2P, and the Reactions of $N(^4S)$ + NO → N_2 + $O(^3P)$ and $O(^3P)$ + NO + M → NO_2 + M. *Bull. Chem. Soc. Jpn.* **1980**, *53*, 3159−3164.

(18) Umemoto, H.; Hachiya, N.; Matsunaga, E.; Suda, A.; Kawasaki, M. Rate Constants for the Deactivation of $N(2^2D)$ by Simple Hydride and Deuteride Molecules. *Chem. Phys. Lett.* **1998**, *296*, 203−207.

(19) Brown, A.; Jimeno, P.; Balint-Kurti, G. G. Photodissociation of N_2O. I. *Ab Initio* Potential Energy Surfaces for the Low-Lying Electronic States $\tilde{X}^1A'$, $2\ ^1A'$, and $1\ ^1A''$. *J. Phys. Chem. A* **1999**, *103*, 11089−11095.

(20) Johnson, M. S.; Billing, G. D.; Gruodis, A.; Janssen, M. H. M. Photolysis of Nitrous Oxide Isotopomers Studied by Time-Dependent Hermite Propagation. *J. Phys. Chem. A* **2001**, *105*, 8672−8680.

(21) Daud, M. N.; Balint-Kurti, G. G.; Brown, A. *Ab initio* Potential Energy Surfaces, Total Absorption Cross Sections, and Product Quantum State Distributions for the Low-lying Electronic States of N_2O. *J. Chem. Phys.* **2005**, *122*, 054305.

(22) Nanbu, S.; Johnson, M. S. Analysis of the Ultraviolet Absorption Cross Sections of Six Isotopically Substituted Nitrous Oxide Species Using 3D Wave Packet Propagation. *J. Phys. Chem. A* **2004**, *108*, 8905−8913.

(23) Schinke, R. Photodissociation of N_2O: Potential Energy Surfaces and Absorption Spectrum. *J. Chem. Phys.* **2011**, *134*, 064313.

(24) Schinke, R.; Schmidt, J. A.; Johnson, M. S. Photodissociation of N_2O: Triplet States and Triplet Channel. *J. Chem. Phys.* **2011**, *135*, 194303.

(25) Schmidt, J. A.; Johnson, M. S.; Schinke, R. Isotope Effects in N_2O Photolysis From First Principles. *Atmos. Chem. Phys.* **2011**, *11*, 8965−8975.

(26) Schmidt, J. A.; Johnson, M. S.; Lorenz, U.; McBane, G. C.; Schinke, R. Photodissociation of N_2O: Energy Partitioning. *J. Chem. Phys.* **2011**, *135*, 024311.

(27) González, M.; Valero, R.; Sayós, R. *Ab initio* and Quasiclassical Trajectory Study of the $N(^2D)$ + $NO(X\ ^2\Pi)$ → $O(^1D)$ + $N_2(X\ ^1S_g^+)$ Reaction on the Lowest $^1A'$ Potential Energy Surface. *J. Chem. Phys.* **2000**, *113*, 10983−10998.

(28) Varandas, A. J. C. Modeling and Interpolation of Global Multi-sheeted Potential Energy Surface. In *Conical Intersections: Electronic Structure, Spectroscopy and Dynamics*; Domcke, W., Yarkony, D. R., Köppel, H., Eds.; Adv. Series Phys. Chem.; World Scientific Publishing: 2004; Vol. *15*; Chapter 5, pp 205−270.

(29) Varandas, A. J. C. Intermolecular and Intramolecular Potentials: Topographical Aspects, Calculation, and Functional Representation via a DMBE Expansion Method. *Adv. Chem. Phys.* **1988**, *74*, 255−338.

(30) Varandas, A. J. C. Multivalued Potential Energy Surfaces for Dynamics Calculations. In *Lecture Notes in Chemistry*; Laganá, A., Riganelli, A., Eds.; Springer: Berlin, 2000; Vol. *75*; pp 33−56.

(31) Li, J.; Varandas, A. J. C. Accurate Ab-initio-based Single-sheeted DMBE Potential-Energy Surface for Ground-State N_2O. *J. Phys. Chem. A* **2012**, *116*, 4646−4656.

(32) Werner, H. J.; Knowles, P. J. An Efficient Internally Contracted Multiconfiguration-reference Configuration Interaction Method. *J. Chem. Phys.* **1988**, *89*, 5803−5814.

(33) Knowles, P. J.; Werner, H.-J. An Efficient Method for the Evaluation of Coupling Coefficients in Configuration Interaction Calculations. *Chem. Phys. Lett.* **1988**, *145*, 514−522.

(34) Kendall, R. A.; Dunning, T. H., Jr.; Harrison, R. J. Electron Affinities of the First-row Atoms Revisited. Systematic Basis Sets and Wave Functions. *J. Chem. Phys.* **1992**, *96*, 6796−6806.
(35) Dunning, T. H., Jr. Gaussian Basis Sets for Use in Correlated Molecular Calculations. I. The Atoms Boron Through Neon and Hydrogen. *J. Chem. Phys.* **1989**, *90*, 1007−1024.
(36) Murrell, J. N.; Carter, S.; Farantos, S. C.; Huxley, P.; Varandas, A. J. C. *Molecular Potential Energy Surfaces*; Wiley: New York, 1984.
(37) Krishnan, R.; Binkley, J. S.; Pople, J. A. Self-consistent Molecular Orbital Methods. XX. A Basis Set for Correlated Wave Functions. *J. Chem. Phys.* **1980**, *72*, 650−654.
(38) Frish, M. J.; Pople, J. A.; Binkley, J. S. Self-consistent Molecular Orbital Methods 25. Supplementary Functions for Gaussian Basis Sets. *J. Chem. Phys.* **1984**, *80*, 3265−3269.
(39) Varandas, A. J. C. A Semiempirical Method for Correcting Configuration Interaction Potential Energy Surfaces. *J. Chem. Phys.* **1989**, *90*, 4379−4391.
(40) Varandas, A. J. C. A Useful Triangular Plot of Triatomic Potential Energy Surfaces. *Chem. Phys. Lett.* **1987**, *138*, 455−461.
(41) Varandas, A. J. C. General discussion. *Faraday Discuss. Chem. Soc.* **1987**, *84*, 351−357.
(42) Peslherbe, G. H.; Wang, H.; Hase, W. L. Monte Carlo Sampling for Classical Trajectory Simulations. *Adv. Chem. Phys.* **1999**, *105*, 171−201.
(43) Hase, W. L.; Duchovic, R. J.; Hu, X.; Komornicki, A.; Lim, K. F.; Lu, D.; Peslherbe, G. H.; Swamy, K. N.; Linde, S. R. V.; Varandas, A. J. C.; et al. VENUS96: A General Chemical Dynamics Computer Program. *QCPE Bull.* **1996**, *16*, 43.
(44) Varandas, A. J. C.; Brandão, J.; Pastrana, M. R. Quasiclassical Trajectory Calculations of the Thermal Rate Coefficients for the Reactions H(D) + O_2 → OH(D) + O and O + OH(D) → O_2 + H(D) as a Function of Temperature. *J. Chem. Phys.* **1992**, *96*, 5137−5150.
(45) Caridade, P. J. S. B.; Varandas, A. J. C. Dynamics Study of the N(^4S) + O_2 Reaction and Its Reverse. *J. Phys. Chem. A* **2004**, *108*, 3556−3564.
(46) LeRoy, R. L.*LEVEL 7.5, A Computer Program for Solving the Radial Schrödinger Equation for Bound and Quasi-bound Levels*; University of Waterloo Chemical Physics Research Report; 2002; http://leroy.waterloo.ca/
(47) Fell, C.; Steinfeld, J. I.; Miller, S. Quenching of N(^2D) by O(^3P). *J. Chem. Phys.* **1990**, *92*, 4768−4778.
(48) LeRoy, R. L. *J. Phys. Chem.* **1969**, *73*, 4338−4344.
(49) Varandas, A. J. C. Accurate Combined-hyperbolic-inverse-power-representation of *Ab initio* Potential Energy Surface for the Hydroperoxyl Radical and Dynamics Study of O + OH Reaction. *J. Chem. Phys.* **2013**, *138*, 134117.
(50) Garrido, J. D.; Caridade, P. J. S. B.; Varandas, A. J. C. Dynamics Study of the HO($v' = 0$) + O_2(v'') Branching Atmospheric Reaction. 1. Formation of Hydroperoxyl Radical. *J. Phys. Chem.* **1999**, *103*, 4815−4822.
(51) Martínez-Núñez, E.; Varandas, A. J. C. Single-Valued DMBE Potential Energy Surface for HSO: A Distributed *n*−Body Polynomial Approach. *J. Phys. Chem. A* **2001**, *105*, 5923−5932.
(52) Rodrigues, S. P. J.; Sabn, J. A.; Varandas, A. J. C. Single-Valued Double Many-Body Expansion Potential Energy Surface of Ground-State SO_2. *J. Phys. Chem. A* **2002**, *106*, 556−562.
(53) Varandas, A. J. C.; Rodrigues, S. P. J. New Double Many-body Expansion Potential Energy Surface for Ground-state HCN from a Multiproperty Fit to *Ab Initio* Energies and Rovibrational Data. *J. Phys. Chem. A* **2006**, *110*, 485−493.
(54) Varandas, A. J. C. Trajectory Binning Scheme and Non-active Treatment of Zero-point Energy Leakage in Quasi-classical Dynamics. *Chem. Phys. Lett.* **2007**, *439*, 386−392.
(55) Bonnet, L.; Rayez, J. Quasiclassical Trajectory Method for Molecular Scattering Processes: Necessity of a Weighted Binning Approach. *Chem. Phys. Lett.* **1997**, *277*, 183.

(Submitted to *J. Chem. Phys.*)

Accurate Double Many-Body Expansion Potential Energy Surface for the $2^1A^{'}$ state of N_2O

Jing Li and António J. C. Varandas*[1]
Departamento de Química, Universidade de Coimbra

3004-535 Coimbra, Portugal

Abstract

An accurate double many-body expansion potential energy surface is reported for the $2^1A^{'}$ state of N_2O. The new DMBE form has been fitted to a wealth of *ab initio* points that have been calculated at the multi-reference configuration interaction level using the full-valence-complete-active-space wave function as reference and the cc-pV*Q*Z basis set, and subsequently corrected semiempirically via double many-body expansion-scaled external correlation method to extrapolate the calculated energies to the limit of a completed basis set and, most importantly, the limit of an infinite configuration interaction expansion. The topographical features of the novel potential energy surface are then examined in detail and compared with corresponding attributes of other potential functions available in the literature. Exploratory trajectories have also been run on this DMBE form with the quasiclassical trajectory method, with the thermal rate constant so determined at room temperature significantly enhancing agrrement with experimental data.

1 Introduction

Recently, the research on the potential energy surface (PES) and dynamics of N_2O has been the subject of considerable experimental[1–5] and theoretical work.[6–11] The collision process of energetically accessible at room temperature:

$$N(^2D) + NO(X\,^2\Pi) \rightarrow O(^1D) + N_2(X\,^1\Sigma_g^+) \tag{1}$$

and its reverse reaction is of interest in atmosphere chemistry.[12–15] However, only a few experimental kinetic studies[16–21] are available dealing with the thermal rate constant

[1]Corresponding author: varandas@uc.pt

for the total removal of N(^2D) by NO at 300 K. The recommended room temperature rate constant, $60 \times 10^{-12}\,\mathrm{cm^3\,s^{-1}}$, is based on the data of Lin and Kaufman,[17] Husain *et al.*,[18,19] and Umemoto *et al.*[21] Although there are no certainty of the product states in such studies,[22] the reaction almost certainly leads to $N_2(X\,^1\Sigma_g^+) + O(^3P,\,^1D,\,^1S)$.

Theoretically, much research has been carried out on the ground state PES.[7–11,23] The first two-dimensional PESs calculated by Brown *et al.*[7] with the NN bond length kept fixed at the experimental value 2.13199 bohr, were then used by Johnson *et al.*[8] in dynamics calculations. González *et al.*[23] are the only authors to have performed an extensive theoretical study of reaction (1) by running quasi-classical trajectory (QCT) on their own PES. Complete-active-space self-consistent field (CASSCF) and the multireference configuration interaction (MRCI) electronic structure calculations were then carried out by Daud *et al.*[10] to improve the electronic structure data but still keeping the NN bond fixed at the equilibrium geometry. Meanwhile, Nanbu and Johnson[9] reported full three-dimensional PESs, which they have also utilized for dynamics cacculation. More recently, Schinke[11] calculated the ground state and exited-state potential energy surfaces, and performed dynamics calculations. Regarding earlier *ab initio* studies, Hopper,[6] Donovan and Husain[22] provided a detailed overview of the low-lying excited state PESs of N_2O. As shown in Figure 1, there are 5 PESs which adiabatically correlate with reactants in C_s symmetry, and correlate with products in reaction (1): $1^1A'$, $2^1A'$, $3^1A'$, $1^1A''$ and $2^1A''$. The rather extensive studies[24,25] performed by our group provide an excellent start towards an understanding of electronic structure, potential scheme and reactivity of the nitrous oxide system. In previous work, a more accurate global PES of N_2O ground state was reported and employed in QCT calculations to determine thermal rate constants, vibrational and rovibrational distributions. Good agreement with the experimental data has been observed, providing more realis-

tic rate constants and hence support of enhanced accuracy for the double many-body expansion (DMBE) PES with respect to other available forms.

There is no theoretical information about all the regions of PES for $2^1A'$ state, which would be also required for studying fully the dynamics and kinetics of reaction (1). Indeed, the major goal of the present work is to obtain a high quality global PES for the $2^1A'$ of N_2O based on DMBE[26–28] theory (for recent progress on the methodology, see elswhere[29]), which will be calibrated from 836 *ab initio* points calculated at the multireference configuration interaction (MRCI)[30] level using the full valence complete active space (FVCAS)[31] as the reference wave function and the cc-pVQZ (VQZ)[32,33] basis set of Dunning's correlation consistent family. The *ab initio* energies calculated in this way have been subsequently corrected, using the double many-body expansion-scaled external correlation method (DMBE-SEC)[34] to extrapolate to the complete configuration interaction limit. The PES so obtained (hereinafter referred to as DMBE PES) shows the correct long range behaviour at all dissociation channels while providing a realistic representation of the PES at all interatomic separations.

This paper is organized as follows. Section 2 describes the *ab initio* calculations employed in the present work. A brief descrition of the analytical DMBE formalism is then presented in section 3. The main topographical features of the DMBE PES are discussed in Section 4, while a comparison of quasiclassical trajectory (QCT) calculations for the thermal rate constant at T = 300 K with experimental results is reproted in section 5. The concluding remarks are summarized in Section 6.

2 *Ab initio* calculations

The *ab initio* calculations have been carried out at the MRCI level using the FVCAS wave function as reference. The VQZ basis set of Dunning has been employed, with the

calculations performed using the Molpro[35] package. A grid of 836 *ab initio* points have been chosen to map the PES over the $O - N_2$ region defined by $1.5 \leq R_{N_2}/a_0 \leq 3.5$, $1.0 \leq r_{O-N_2}/a_0 \leq 10.0$ and $0 \leq \gamma/\deg \leq 90$. For the $N - NO$ interactions, a grid defined by $1.5 \leq R_{NO}/a_0 \leq 3.5$, $1.0 \leq r_{N-NO}/a_0 \leq 10.0$ and $0 \leq \gamma/\deg \leq 180$ has been chosen. For both channels, r, R and γ are the atom-diatom Jacobi coordinates.

We start the discussion with a survey of the structures of four lowest electronic $^1A'$ states. In these calculations the CASSCF orbitals for the MRCI were obtained by state averaging over all 4 states using equal weights. Figure 2 (a) shows the potential energy curves as a function of Jacobi coordinate r_{O-N_2} at a fixed N_2 bond distance $R_{N_2} = 2.13\,a_0$ and Jacobi angle $\gamma = 0°$. In all of our potential energy cuts, the reference (zero) energy is taken to be the ground state dissociate limit. There are 3 states: $1^1A'$, $2^1A'$ and $3^1A'$ correlated with $O(^1D) + N_2(X\,^1\Sigma_g^+)$ asymptote. Moreover, the $4^1A'$ state correlates with $O(^1S) + N_2(X\,^1\Sigma_g^+)$ asymptote.

Figure 2 (c) shows the magnitude of the transition dipole connecting the ground state to the first singlet excited state as a function of the γ at $R_{N_2} = 2.13\,a_0$ and $r_{O-N_2} = 3.3\,a_0$. It is interesting to note that the transition dipole moment surface shows two distinct maxima and the minimum seam between them corresponds directly with the maximum (minimum) energy seam seen on the $1^1A'$ ($2^1A'$) surface. Both of the dipole moments are zero in the linear geometry and are strongly angle dependent. The sharp dip in the magnitude of the $1^1A' \rightarrow 2^1A'$ transition dipole at around 50.0° coincides with the region of the conical intersection between the two lowest $^1A'$ states.

To account for electronic excitations beyond singles and doubles and, most importantly, for the incompleteness of the basis set, the calculated *ab initio* energies have been subsequently corrected using the DMBE-SEC method. Thus, the total DMBE-

SEC interaction energy is written as

$$V(\mathbf{R}) = V_{FVCAS}(\mathbf{R}) + V_{SEC}(\mathbf{R}) \tag{2}$$

where

$$V_{FVCAS}(\mathbf{R}) = \sum_{\mathrm{AB}} V^{(2)}_{\mathrm{AB},FVCAS}(R_{AB}) + V^{(3)}_{\mathrm{ABC},FVCAS}(R_{\mathrm{AB}}, R_{\mathrm{BC}}, R_{\mathrm{AC}}) \tag{3}$$

$$V_{SEC}(\mathbf{R}) = \sum_{\mathrm{AB}} V^{(2)}_{\mathrm{AB},SEC}(R_{AB}) + V^{(3)}_{\mathrm{ABC},SEC}(R_{\mathrm{AB}}, R_{\mathrm{BC}}, R_{\mathrm{AC}}) \tag{4}$$

where $\mathbf{R} = \{R_{\mathrm{AB}}, R_{\mathrm{BC}}, R_{\mathrm{AC}}\}$ is a collective variable of all internuclear distances. Explicitly, the expansion of the two terms in Eq. (4) assume the form:

$$V^{(2)}_{\mathrm{AB},SEC}(R_{\mathrm{AB}}) = \frac{V^{(2)}_{\mathrm{AB},FVCAS-CISD}(R_{\mathrm{AB}}) - V^{(2)}_{\mathrm{AB},FVCAS}(R_{\mathrm{AB}})}{F^{(2)}_{\mathrm{AB}}} \tag{5}$$

$$V^{(3)}_{\mathrm{ABC},SEC}(\mathbf{R}) = \frac{V^{(2)}_{\mathrm{AB},FVCAS-CISD}(\mathbf{R}) - V^{(3)}_{\mathrm{ABC},FVCAS}(\mathbf{R})}{F^{(3)}_{\mathrm{ABC}}} \tag{6}$$

Following previous work,[34] $F^{(2)}_{\mathrm{AB}}$ in Eq. (5) is chosen to reproduce the bond dissociation energy of the corresponding AB diatom, while $F^{(3)}_{\mathrm{ABC}}$ in Eq. (6) is estimated as the average of the three two-body $F-$factors. For the VQZ basis set, such a procedure yields: $F^{(2)}_{\mathrm{NN}} = 0.7057$, $F^{(2)}_{\mathrm{NO}} = 0.7829$, and $F^{(3)}_{\mathrm{ONN}} = 0.75722$, thence highly improving the scaling factors obatined with the previous AVTZ basis set results:[24] $F^{(2)}_{\mathrm{NN}} = 0.3532$, $F^{(2)}_{\mathrm{NO}} = 0.6532$, and $F^{(3)}_{\mathrm{ONN}} = 0.5532$. Since our MRCI energies have been extrapolated to the complete basis set/configuration interaction limit, and the use of a larger basis set would make the present work computationally unaffordable, we judged as unnecessary any further improvement of the results.

3 Double many-body expansion potential energy surface

Within the framework of DMBE theory, the single-sheeted PES is written as

$$V(\mathbf{R}) = V^{(1)}_{\mathrm{O}(^1D)} f_1(\mathbf{R}) + V^{(1)}_{\mathrm{N_A}(^2D)} f_2(\mathbf{R}) + V^{(1)}_{\mathrm{N_B}(^2D)} f_3(\mathbf{R}) +$$

$$\sum_{i=1}^{3}\left[V_{\rm EHF}^{(2)}(R_i)+V_{\rm dc}^{(2)}(R_i)\right]+V_{\rm EHF}^{(3)}(\mathbf{R})+V_{\rm dc}^{(3)}(\mathbf{R}) \tag{7}$$

In the (psendo-) one-body term, $V_{\rm O(^1D)}^{(1)}=0.0723399\,{\rm E_h}$ represents the energy difference between the ^1D and ^3P states of atomic oxygen, and $f_1(\mathbf{R})$ is a switching function used to warrant the correct behaviour at the $N_2(X\,^1\Sigma_g^+)+O(^1D)$ dissociation limits. In turn, $V_{\rm N_A(^2D)}^{(1)}$ and $V_{\rm N_B(^2D)}^{(1)}$ represent the energy difference between the N(^2D) and N(^4S) states: $V_{\rm N_A(^2D)}^{(1)}$, $V_{\rm N_B(^2D)}^{(1)}=0.0898679\,{\rm E_h}$. Regarding the two-body and three-body energy terms, they are split as usual into two contributions: the extended Hartree-Fock (EHF) and dynamical correlation (dc) energies. The following subsections give a brief description of the various energy terms. (the reader is addressed to Ref. 36, 37 and references therein for details).

3.1 Dissociation scheme and one-body switching function

As shown in Figure 1, the title system has the same dissociation scheme as N_2O (X^1A') ground state:

$$N_2O(2^1A') \rightarrow N_2\,(X\,^1\Sigma_g^+)+O(^1D) \tag{8}$$

$$\rightarrow NO\,(X\,^2\Pi)+N(\,^2D) \tag{9}$$

However, in the $2^1A'$ state of N_2O, the O+N_2 and N+NO channels dissociate into the distinct atoms: O(^1D)+N(^4S)+N(^4S) and N(^2D)+N(^4S)+O(^3P), respectively. To get a simple analytical form for the PES, we have then utilized the same dissociation limit O(^3P)+N(^4S)+N(^4S) as for N_2O (X^1A') ground state. Thus, pseudo one-body terms have been utilized which consist of products of the energy of the excited atoms relative to their fundamental states by suitable three-dimensional switching forms. Specifically, we have utilized a variant of a switching function previously developed in our group,[36]

which has been also utilized for the N_2O (X^1A') ground state PES:

$$h_i(\mathbf{R}_i) = \frac{1}{4}\sum_{m=1}^{2}\{1-\tanh[\alpha_m(R_i-R_i^{m0})+\beta_m(R_i-R_i^{m1})^3]\}, \quad i=1,2,3 \tag{10}$$

where $i = 1, 2, 3$ are the indexes used for O, N_A and N_B (respectively), and R_1, R_2, R_3 correspondingly represent the distances $N_A - N_B$, $N_A - O$, and $N_B - O$. In turn, α_m and β_m are parameters to be specified from a least-squares fit to an extra set of 11 VQZ points that control the $O(^1D) - O(^3P)$ decay as the $N_A - N_B$ distance increases for $O + N_2$ configurations, as shown by the solid line and open circles in Figure 3(a). Another set of 12 VQZ points has been utilized that control the $N_A(^2D) - N_A(^4S)$ decay as the $N_B - O$ distance increases for $N_A + N_BO$ configurations shown by the solid line and open circles in Figure 3(b). Because N_A and N_B are indistinguishable atoms, we have set the same parameters in the switching function for nitrogen.

Thus, the one-body terms assure the correct asymptotic limits in N_2O (X^1A') ground state PES,[24] but in N_2O ($2^1A'$) the oxygen (nitrogen) atom departs in the excited state $O(^1D)$ [$N(^2D)$], thence not showing the energy decay of $O(^1D) - O(^3P)$ [$N(^2D) - N(^4S)$]. We have tried to take into simulate this distinct behavior as a pseudo-one-body energy deference. For this purpose, we have calculated the energy deference between the ground state and $2^1A'$ state PESs for geometries where the O (N) atom is far from the N_2 (NO) and the bond length of the diatom is increasing. The energy difference so obatined has then been fitted using the form:

$$h_i'(\mathbf{R}_i) = \frac{1}{4}\sum_{n=1}^{2}\{1+\tanh[\alpha_n(R_i-R_i^{n0})+\beta_n'(R_i-R_i^{n1})^3]\}, \quad i=1,2,3 \tag{11}$$

with the same representation of parameters in Eq. (10), Thus, α_n and β_n are parameters determined from a least-squares fit to an extra set of 14 points that control the energy deference of the two lowest $^1A'$ states as the $N_A - N_B$ distance increases for $O + N_2$ configurations, as shown the solid line (in red) and closed circles in Figure 3(a).

Similarly, another set of 18 points that control the energy difference as the $N_B - O$ distance increases for $N_A + N_BO$ configurations has been fitted as shown by the solid line (in red) and closed circles in Figure 3(b). As discussed above, the same parameters have been utilized in the switching function for both nitrogen atoms.

To get a smooth three-body energy term, we further choose to multiply Eq. (10) and Eq. (11) by an amplitude function that annihilates Eq. (10) and Eq. (11) at short-ranges (short $O - N_2$ and $N - NO$ distance):

$$g_i(\mathbf{r}_i) = \frac{1}{2}\{1 + \tanh[\alpha(r_i - r_i^0)]\}, \quad i = 1, 2, 3 \tag{12}$$

where r_1 is the distance of the O atom to the center of mass of N_2. A word is necessary at this point to clarify the notation. The indexes (i, j, k) number atoms (say, 1 for O, and 2 and 3 for N), and r_i represents the Jacobi coordinate separating atom i from the center of mass of diatom jk whose bond distance is itself denoted by R_i. The final switching function then assumes the form

$$f_i(\mathbf{R}) = g_i(r_i)[h_i(R_i) + h_i'(R_i))], \quad i = 1, 2, 3 \tag{13}$$

with the parameters in $g(r_i)$ chosen to warrant that its main effect occurs for $O - N_2$ and $N - NO$ distances larger than $8\,a_0$ or so as illustrated in Figure 3(c). All the numerical values of parameters in Eq. (13) are collected in Table 1 of the Supporting Information (SI).

3.2 Two-body energy terms

The potential energy curves of the diatomic fragments have been obtained using the extended Hartree-Fock approximate correlation energy method, including the united atom limit (EHFACE2U),[38] which shows the correct behaviour at the asymptotic limits. they assume the general form

$$V(R) = V_{\mathrm{EHF}}(R) + V_{\mathrm{dc}}(R) \tag{14}$$

where EHF refers to the extended Hartree-Fock type energy and dc is the dynamical correlating energy. The exponentially decaying part of EHF part energy is represented by the general form[27]

$$V_{\rm EHF}(R) = -\frac{D}{R}\left(1 + \sum_{i=1}^{n} a_i r^i\right)\exp(-\gamma r) \tag{15}$$

where $\gamma = \gamma_0\,[1 + \gamma_1 \tanh(\gamma_2 r)]$ and $r = R - R_e$ is the displacement from the equilibrium diatomic geometry. In turn, the dc energy contribution of the diatomic potential function is written as the following damped dispersion series [39]

$$V_{\rm dc}(R) = -\sum_{n=6,8,10} C_n \chi_n(R) R^{-n} \tag{16}$$

As already noted, the potential functions of NO ($X\,^2\Pi$) and $N_2(X\,^1\Sigma_g^+)$ are modelled from our own calculated *ab initio* energies and experimental dissociation energy.[40,41] The relevant numerical data are gathered in Table 2 of the SI. Figure 4 illustrates the NO ($X\,^2\Pi$) and $N_2(X\,^1\Sigma_g^+)$ curves so obtained. Clearly, they mimic accurately the calculated *ab initio* energies as obtained after scaling of the external correlation.[37,42]

3.3 Three-body energy terms

3.3.1 Three-body dynamical correlation energy

The three-body dc energy assumes the usual form of a summation in inverse powers of the fragment separation distances[37]

$$V_{dc}^{(3)} = -\sum_i \sum_n f_i(\mathbf{R}) \chi_n(r_i) C_n^{(i)}(R_i, \theta_i) r_i^{-n} \tag{17}$$

where i labels the I-JK channel associated with the center of mass separation and (r_i,θ_i,R_i) are the Jacobi coordinates corresponding to the specific $\mathbf{R} = (R_1, R_2, R_3)$ geometry of the triatomic system (see Figure 1 of Ref. 43). Moreover $f_i(\mathbf{R}) = \frac{1}{2}\{1 - \tanh[\xi(\eta R_i - R_j - R_k)]\}$ is a convenient switching function. Following recent work on NH_2,[36] we have fixed $\eta = 6$ and $\xi = 1.0\,a_0^{-1}$. $\chi_n(r_i)$ is the damping function, which takes

the form employed elsewhere.[36,37] In additional the value of ρ has been optimized by a trial-and-error to get a good asymptotic behaviour of the dynamical correlation term, leading to $\rho = 16.125a_0$ The atom-diatom dispersion coefficients in Eq. (17), which are given by

$$C_n^{(i)}(R_i) = \sum_L C_n^L(R) P_L(cos\theta_i) \tag{18}$$

Where $P_L(cos\theta_i)$ denotes the Lth Legendre polynomial. For practical purposes, the expansion in Eq. (18) has been truncated by considering only the coefficients C_6^0, C_6^2, C_8^0, C_8^2, C_8^4 and C_{10}^0; all coefficients have been obtained by the generalized Slater-Kirkwood formula,[44] with polarizabilities calculated in the present work at MRCI/VQZ level. As usual, the atom-diatom dispersion coefficients so calculated for a set of internuclear distance have then been fitted to the form

$$C_n^{L,A-BC}(R) = C_n^{L,AB} + C_n^{L,AC} + D_M \left(1 + \sum_{i=1}^{3} a_i r^i\right) \exp\left(-\sum_{i=1}^{3} b_i r^i\right) \tag{19}$$

where $C_n^{L,AB}$, for $L = 0$, are the corresponding diatom dispersion coefficients. All parameters and coefficients in Eq. (19) have been explained elsewhere.[45] The numerical values of parameters in Eq. (17) are collected in Table 3 of the SI, while their internuclear dependences are displayed in Figure 1 of the SI.

3.4 Three-body extended Hartree-Fock energy

For a given triatomic geometry, the total three-body energy can be obtained, by removing the sum of the one-body and two-body energy terms from the corresponding DMBE-SEC interaction energies in Eq. (7). By further subtracting the three-body dc energy part described in Eq. (17) from the total three-body energy, one obatains the three-body EHF energy, which can be represented by the following three-body distributed-polynomial[46] form

$$V_{\rm EHF}^{(3)} = \sum_{j=1}^{4} P^j(Q_1, Q_2, Q_3) \times \prod_{i=1}^{3} \{1 - \tanh[\gamma_i^j (R_i - R_i^{j,\rm ref})]\} \tag{20}$$

where $P^j(Q_1, Q_2, Q_3)$ is the j-th polynomial up to six-order in the symmetry coordinates which are defined as

$$\begin{pmatrix} Q_1 \\ Q_2 \\ Q_3 \end{pmatrix} = \begin{pmatrix} \sqrt{1/3} & \sqrt{1/3} & \sqrt{1/3} \\ 0 & \sqrt{1/2} & -\sqrt{1/2} \\ \sqrt{2/3} & -\sqrt{1/6} & -\sqrt{1/6} \end{pmatrix} \begin{pmatrix} R_1 - R_1^{j,\mathrm{ref}} \\ R_2 - R_2^{j,\mathrm{ref}} \\ R_3 - R_3^{j,\mathrm{ref}} \end{pmatrix} \tag{21}$$

To obtain the reference geometries $R_i^{j,\mathrm{ref}}$, we have first assuming their values to coincide with bond distances of the associated stationary points. Subsequently, we have relaxed this condition via a trial-and-error procedure such as to reduce the root-mean-square-deviation (rmsd) of the final least square fit. Similarly, the nonlinear range-determining parameters γ_i^j have been optimized in this way. The complete set of parameters amounts to a total of 200 coefficients c_i, 12 nonlinear coefficients γ_i^j, and 12 reference geometries $R_i^{j,\mathrm{ref}}$. A total of 836 points covering a range of energy up to $\sim 500\,\mathrm{kcal\,mol^{-1}}$ above the N_2O global minimum, have been used for the calibration procedure. The resulting numerical values of all least-squares parameters are gathered in Tables 4 and 5 of the SI. The stratified rmsd of the final PES with respect to the fitted *ab initio* energies are gathered in Table 1. As shown, the fit shows a maximum rmsd of $0.88\,\mathrm{kcal\,mol^{-1}}$ up to the highest repulsive energy stratum.

4 Features of the DMBE PES

Table 2 compares the attributes of the stationary points of the DMBE PES with those of other theoretical potentials for N_2O ($2^1A'$): minima (labelled M1 to M6) and saddle points (labelled SP1 to SP9, with SP8 and SP9 being second-order saddle points and hence of little relevance in kinetics). Most notable is that a shallow minimum (M1) located at $R_1 = 2.257\,a_0$, $R_2 = 2.501\,a_0$ and $R_3 = 3.941\,a_0$, with a well depth of -0.3592 E_h relative to the $O(^1D) + N(^4S) + N(^4S)$ asymptote, lying 3.995 eV above the N_2O ground state global minimum (with geometry $R_1 = 2.155\,a_0$, $R_2 = 2.255\,a_0$ and $R_3 = 4.410\,a_0$, as reported in Ref. 24). The predicted geometry and well depth of M1

are seen to be good coincident with those reported by Schinke,[11] who have based their function on MRCI calculations using a more expensive aug-cc-pVQZ (AVQZ) basis set: the bond length differences are 0.054, 0.007 and 0.008 a_0, with a ∠ONN difference of 2.4° and 0.041 eV difference for the well depth. However, the harmonic frequencies of M1 are 1408.0, 1114.9 and 2415.3 cm^{-1}, thus showing deviations of 724.0, 199.1 and 787.0 cm^{-1}, respectively. The bent minimum also exists on the PES of Daud *et al.*[10] and on the 3D PES of Nanbu and Johnson.[9] Furthermore, We have found a linear saddle point (SP7) with a height of -0.2636 E_h, thus lying 6.596 eV above the the N_2O ground state global minimum, and located at $R_1 = 2.332\,a_0$, $R_2 = 2.364\,a_0$ and $R_3 = 4.696\,a_0$, while being in fairly good agreement with the theoretical prediction of linear equilibrium of 6.492 eV.[11]

Figures 5-8 illustrate the major topographical features of the N_2O DMBE PES reported in the present work. The salient features from these plots are some of the most relevant stationary points for the title system. Clearly, visible is a smooth and correct behaviour over the whole configuration space. Figure 5 shows that the oxygen atom approaches N_2 from large atom-diatom separations along T-shaped geometries via overcoming the barriers. In this case, keeping C_{2v} symmetry, M5 precedes a transition state SP1 with a barrier of about -0.2443 E_h with respect to $O(^1D) + N(^4S) + N(^4S)$ asymptote, connecting with M6, and evolving through another transition state SP2 evolving to a second-order saddle point SP8. Also visible is that when the O atom inserts into N_2, the ∠NON opens progressively, while the distance of O to the center of N-N shortens, and the bond length of N-N increases. The vertical dashed line indicates the cut of the fitted PES shown in the insert for $R_{N_2} = 2.13\,a_0$, which shows that the somewhat wiggly behaviour occurring in the region close to $R_{N_2} = 2.0\,a_0$ is also present in the fitted *ab initio* data. In turn, Figure 6 shows a contour plot for the insertion of

N(^2D) into the mass center of NO. The notable feature in this plot is that a van der Waals bent minimum M2 evolves through a serials of C_s symmetry minima (i.e., M3 and M1) and transition states (i.e., SP3 and SP4), until it reaches the $C_{\infty v}$ transition state SP7.

Figure 7 shows energy contours for the O atom moving around the N_2 ground-state diatom whose energy has been optimized within the range $1.8 \leq R_{N_2}/a_0 \leq 2.5$. The corresponding plot for the N atom moving around the NO diatom with its energy optimized over the range $1.9 \leq R_{NO}/a_0 \leq 2.6$ is displayed in Figure 8. The two plots clearly show a smooth behaviour both at short and long range regions. From Figure 7, we can see the presence of M1, with Jacobi coordinates: $R_{N_2} = 2.257\,a_0$, $r_{O-N_2} = 3.101\,a_0$ and $\gamma = 48.6°$. In turn, Figure 2 (b) shows that the intermediate well of the N_2O ($2^1A'$) PES is the counterpart of the barrier of the X^1A' state PES around the same bending angle (near 50°). In other words, it is the result of the avoiding crossing at bent geometries between the two lowest $^1A'$ states. Also visible is that in Figure 2 (c) the sharp dip in the magnitude of the $2^1A' \rightarrow 1^1A'$ transition dipole at around 50° coincides with the region of the conical intersection between the two lowest $^1A'$ states. The present results display therefore trends similar to other preceding works.[9–11] Moreover, the PES also predicts the existence of C_{2v} minima M5 and M6.

Figure 8 illustrates the minima (i.e., M1, M3) and transition states (i.e., SP1, SP4, SP7). Specially, SP7 is a linear barrier with Jacobi coordinates: $R_{N_2} = 2.332\,a_0$, $r_{O-N_2} = 3.593\,a_0$ and $\gamma = 0°$, in good agreement with the value reported by Schinke,[11] who has predicted the linear equilibrium in the $2^1A'$ PES to occur at $R_{N_2} = 2.339\,a_0$, $r_{O-N_2} = 3.565\,a_0$ and $\gamma = 0°$. Between M1 and M3 is a transition state (SP4), that is a basically a stretched NNO structure which is located at $R_1 = 2.720\,a_0$, $R_2 = 2.223\,a_0$,

$R_3 = 3.400\,a_0$ and $\angle \mathrm{ONN} = 86.3\,^\circ$, with an energy of $0.0931\,\mathrm{E_h}$ higher than M1, and $0.0026\,\mathrm{E_h}$ above M3. Figure 7 and Figure 8 illustrate also the long range part of the potential energy surface which was fitted such as to provide a reliable description of the van der Waals minima and transition states.

Cuts of DMBE PES along the atom-diatom radial coordinate are shown in Figure 9 for a fixed diatomic bond length of $R_{\mathrm{N_2}} = 2.132,\ 2.5,\ 3.5\,a_0$ in $\mathrm{O} - \mathrm{N_2}$ channel, and $R_{\mathrm{NO}} = 2.237,\ 2.5,\ 3.5\,a_0$ in N-NO channel, respectively. Clearly, the PES mimics accurately the calculated *ab initio* energies. Finally, Figure 10 shows a relaxed triangular plot[47] utilizing scaled hyperspherical coordinates ($\beta^\star = \beta/Q$ and $\gamma^\star = \gamma/Q$):

$$\begin{pmatrix} Q \\ \beta \\ \gamma \end{pmatrix} = \begin{pmatrix} 1 & 1 & 1 \\ 0 & \sqrt{3} & -\sqrt{3} \\ 2 & -1 & -1 \end{pmatrix} \begin{pmatrix} {R_1}^2 \\ {R_2}^2 \\ {R_3}^2 \end{pmatrix} \tag{22}$$

That is most useful plot not only because it illustrates in a single view all important topographical features of the PES but also because it can be utilized to visualize their connectivity in a more physical and multidimensional way.

5 Exploratory dynamics studies

Although we plan to run detailed calculations on the dynamics and kinetics of the title species, we have run here for testing purposes some batches of 10000 trajectories with a view to compute the thermal rate constant for the $\mathrm{N}(^2D) + \mathrm{NO}(X\,^2\Pi)$ reaction at $T = 300\,\mathrm{K}$, using current DMBE/SEC PES for the $2^1A'$ state of $\mathrm{N_2O}$. All calculations have been carried out using the VENUS96[48] computer code. An integration step size of 0.2 fs has been chosen such as to warrant conservation of the total energy within $0.01\,\mathrm{kcal\,mol^{-1}}$ or smaller. As usual, all trajectories started at a distance between the incoming atom and the center-of-mass of the diatom of 19 Å, a value sufficiently large to make the interaction energy essentially negligible. The results are collected in Table 3 along with the results from our previous work.[25] Also gathered is the available

experimental information concerning the total $N(^2D) + NO(X\,^2\Pi)$ rate constant. Note that, to a first approximation, the first singlet excited state ($2^1A'$) will contribute a value of $k = (7.2 \pm 0.3) \times 10^{-12}\,cm^3\,s^{-1}$ to the total reactivity of the system at room temperature, thence a quite significant contribution ($\sim 30\%$) to reaction (1). A sum of the rate constants of the two lowest $^1A'$ is $(27.5 \pm 0.2) \times 10^{-12}\,cm^3\,s^{-1}$, a result that falls within the error bas of one experimental estimated and is about a half of the more consensual rate constant value, $k = 60 \times 10^{-12}\,cm^3\,s^{-1}$ for the total reaction in $N(^2D) + NO(X\,^2\Pi)$. An improved agreement with the experimental results has therefore been obtained, even though there are large experimental uncertainties amony the existing experimental estimates. As stated in Introduction, there are 5 PESs which adiabatically correlate with reactants in C_s symmetry, as well as with products for reaction (1). Thus, an additional study on the other correlating PES is required, a task that is currently in progress.

6 Concluding remarks

A wealth of accurate MRCI/VQZ energies has been calculated in the present work to map the PES of the first singlet excited state of N_2O. Such raw energies have then been suitably corrected using the DMBE-SEC method to approximate the exact nonrelativistic energy and fitted to a single-sheeted DMBE form, which is expected to be realistic over the entire configuration space. Several minima and transition states have been characterized on the current DMBE PES for the $2^1A'$state of N_2O, which were then compared with the topographical predictions of other forms as well as experimental data available in the literature. Based on such features, it is concluded that the DMBE PES here reported is globally valid while accurately fitting the *ab initio* points used for its calibration. Finally, the novel DMBE PES has been used for exploratory quasiclassical

trajectory calculations of the thermal rate constant at room temperature. The results show good agreement with previous high quality theoretical studies and the available experimental data.

Acknowledgments

This work was financed by FEDER through Programa Operacional Factores de Competitividade-COMPETE and national funds under the auspices of Fundação para a Ciência e a Tecnologia, Portugal (projects PTDC/QUI-QUI/099744/2008, PTDC/AAC-AMB/-099737/2008 and SFRH/BD/66471/2009).

References

[1] G. S. Selwyn and H. S. Johnston, J. Chem. Phys. **74**, 3791 (1981).

[2] T. F. Hanisco and A. C. Kummel, J. Phys. Chem. **97**, 7242 (1993).

[3] D. W. Neyer, A. J. R. Heck, and D. W. Chandler, J. Chem. Phys. **110**, 3411 (1999).

[4] M. Brouard, P. O'Keeffe, M. D. Joseph, and D. Minayev, Phys. Rev. Lett. **86**, 2249 (2001).

[5] M. Brouard, A. P. Clark, C. Vallance, and O. S. Vasyutinskii, J. Chem. Phys. **114**, 6690 (2001).

[6] D. G. Hopper, J. Chem. Phys. **80**, 4290 (1984).

[7] A. Brown, P. Jimeno, and G. G. Balint-Kurti, J. Phys. Chem. A **103**, 11089 (1999).

[8] M. S. Johnson, G. D. Billing, A. Gruodis, and M. H. M. Janssen, J. Phys. Chem. A **105**, 8672 (2001).

[9] S. Nanbu and M. S. Johnson, J. Phys. Chem. A **108**, 8905 (2004).

[10] M. N. Daud, G. G. Balint-Kurti, and A. Brown, J. Chem. Phys. **122**, 054305 (2005).

[11] R. Schinke, J. Chem. Phys **134**, 064313 (2011).

[12] M. Brouard, S. P. Duxon, P. A. Enriquez, R. Sayós, and J. P. Simons, J. Phys. Chem. **95**, 8169 (1991).

[13] A. J. Alexander, F. J. Aoiz, M. Brouard, I. Burak, Y. Fujimura, J. Short, and J. P. Simons, Chem. Phys. Lett. **262**, 589 (1996).

[14] Y. Hsu, J. Wang, and K. Liu, J. Chem. Phys. **107**, 2351 (1997).

[15] A. R. Ravishankara, J. S. Daniel, and R. W. Portmann, Science **326**, 123 (2009).

[16] G. Black, T. G. Slanger, G. A. S. John, and R. A. Young, J. Chem. Phys. **51**, 116 (1969).

[17] C. Lin and F. Kaufman, J. Chem. Phys. **55**, 3760 (1971).

[18] D. Husain, L. J. Kirsch, and J. R. Wiesenfeld, Faraday Discuss. Chem. Soc **53**, 201 (1972).

[19] D. Husain, S. K. Mitra, and A. N. Young, J. Chem. Soc. Faraday Trans. 2 **70**, 1721 (1974).

[20] K. Sugawara, Y. Ishikawa, and S. Sato, Bull. Chem. Soc. Jpn. **53**, 3159 (1980).

[21] H. Umemoto, N. Hachiya, E. Matsunaga, A. Suda, and M. Kawasaki, Chem. Phys. Lett. **296**, 203 (1998).

[22] R. J. Donovan and D. Husain, Chem. Rev. **70**, 489 (1970).

[23] M. González, R. Valero, and R. Sayós, J. Chem. Phys **113**, 10983 (2000).

[24] J. Li and A. J. C. Varandas, J. Phys. Chem. A **116**, 4646 (2012).

[25] J. Li, P. J. S. B. Caridade, and A. J. C. Varandas, J. Phys. Chem. A **118**, 1277 (2014).

[26] A. J. C. Varandas, *Conical Intersections: Electronic Structure, Spectroscopy and Dynamics* (World Scientific Publishing, 2004), chap. 5, p. 205, Advanced Series in Physical Chemistry.

[27] A. J. C. Varandas, Adv. Chem. Phys. **74**, 255 (1988).

[28] A. J. C. Varandas, in *Lecture Notes in Chemistry*, edited by A. Laganá and A. Riganelli (Springer, Berlin, 2000), vol. 75, pp. 33–56.

[29] A. J. C. Varandas, J. Chem. Phys. **138**, 054120 (2013).

[30] H.-J. Werner and P. J. Knowles, J. Chem. Phys. **89**, 5803 (1988).

[31] P. J. Knowles and H.-J. Werner, Chem. Phys. Lett. **115**, 259 (1985).

[32] R. A. Kendall, T. H. Dunning Jr., and R. J. Harrison, J. Chem. Phys. **96**, 6769 (1992).

[33] T. H. Dunning Jr., J. Chem. Phys. **90**, 1007 (1989).

[34] A. J. C. Varandas, J. Chem. Phys. **90**, 4379 (1989).

[35] H.-J. Werner, P. J. Knowles, R. Lindh, M. Schütz, P. Celani, T. Korona, F. R. Manby, G. Rauhut, R. D. Amos, A. Bernhardsson, A. Berning, D. L. Cooper, M. J. O. Deegan, A. J. Dobbyn, F. Eckert, C. Hampel, G. Hetzer, A. W. Lloyd, S. J. McNicholas, W. Meyer, M. E. Mura, A. Nicklass, P. Palmieri, R. Pitzer,

U. Schumann, H. Stoll, A. J. Stone, R. Tarroni, and T. Thorsteinsson, MOLPRO, version 2002.6, a package of ab initio programs (2003), see http://www.molpro.net.

[36] A. J. C. Varandas and L. A. Poveda, Theor. Chem. Acc. **116**, 404 (2006).

[37] A. J. C. Varandas, J. Chem. Phys. **105**, 3524 (1996).

[38] A. J. C. Varandas and J. D. Silva, J. Chem. Soc. Faraday Trans. **88**, 941 (1992).

[39] A. J. C. Varandas, Mol. Phys. **60**, 527 (1987).

[40] K. P. Huber and G. Herzberg, Molecular Spectra and Molecular Structure Constants of Diatomic Molecules (van Nostrand Reinhold, New York, 1979).

[41] K. Lodders, J. Phys. Chem. Ref. Data. **33**, 357 (2004).

[42] F. B. Brown and D. G. Truhlar, Chem. Phys. Lett. **117**, 307 (1985).

[43] A. J. C. Varandas, Chem. Phys. Lett. **194**, 333 (1992).

[44] M. A. Matías and A. J. C. Varandas, Mol. Phys. **70**, 623 (1990).

[45] A. J. C. Varandas and S. P. J. Rodrigues, J. Phys. Chem A **110**, 485 (2006).

[46] E. Martínez-Núñez and A. J. C. Varandas, J. Phys. Chem. A **105**, 5923 (2001).

[47] A. J. C. Varandas, Chem. Phys. Lett. **138**, 455 (1987).

[48] W. L. Hase, R. J. Duchovic, X. Hu, A. Komornicki, K. F. Lim, D. Lu, G. H. Peslherbe, K. N. Swamy, S. R. V. Linde, A. J. C. Varandas, H. Wang, and R. J. Wolf, QCPE Bull. **16**, 43 (1996).

Table 1: Stratified root-mean-square deviations (in kcal mol^{-1}) of the DMBE PES.

Energy[a)]	$N^{b)}$	max.dev[c)]	rmsd	$N^{d)}_{>\mathrm{rmsd}}$
10	99	1.586	0.415	20
20	128	1.586	0.426	30
30	151	2.055	0.505	35
40	172	2.324	0.572	41
50	210	2.324	0.587	47
60	287	2.324	0.629	74
70	344	2.324	0.650	95
80	399	2.324	0.702	118
90	507	3.282	0.736	133
100	557	4.608	0.756	140
150	741	4.608	0.847	163
200	817	4.608	0.864	185
250	835	4.608	0.880	188
300	836	4.608	0.880	188
400	836	4.608	0.880	188
500	836	4.608	0.880	188

[a)] The units of energy and rmsd are kcal mol^{-1}.
[b)] Number of points in the indicated energy range.
[c)] Maximum deviation up to the indicated energy range.
[d)] Number of points with an energy deviation larger than the RMSD.

Table 2: Properties of stationary points on the N_2O $2^1A'$ DMBE-SEC PES [b)]

Feature	R_1/a_0	R_2/a_0	R_3/a_0	θ_{ONN}	V/E_h [a)]	ω_1	ω_2	ω_3
				Minima				
M1(C_s)	2.257	2.501	3.941	111.8	-0.3592(3.995[c])	1408.0	1114.9	2415.3
Schinke[11]	2.311	2.508	3.933	109.4	3.954	684	1314	1628
M2(C_s)	7.248	6.503	2.178	17.1	-0.2254	62.1	28.2	1918.7
M3(C_s)	2.835	2.250	3.213	77.4	-0.2687	1803.7	1292.6	768.2
M4(C_s)	5.511	2.042	4.026	36.5	-0.2314	1882.1	311.6	559.4
M5(C_{2v})	2.078	6.280	6.280	80.5	-0.3641	2373.5	32.3	68.4
M6(C_{2v})	2.638	2.732	2.732	61.2	-0.2608	1259.6	859.8	835.6
				Transition states				
SP1(C_{2v})	2.335	3.064	3.064	67.6	-0.2443	1835.5	1056.5i	395.6
SP2(C_{2v})	4.483	2.429	2.429	22.7	-0.1907	1068.1	392.9	1225.7i
SP3(C_s)	4.303	3.849	2.161	30.1	-0.2146	497.1i	1576.5	363.2
SP4(C_s)	2.720	2.223	3.400	86.3	-0.2661	864.4i	1855.5	1144.2
SP5(C_s)	2.757	2.926	2.554	66.7	-0.2571	806.0i	1411.7	912.8
SP6(C_s)	2.136	3.058	4.422	115.6	-0.3413	454.2i	1722.6	490.2
SP7($C_{\infty v}$)	2.332	2.364	4.696	180.0	-0.2636(6.596[c])	1565.0	861.5i	1224.0
Schinke[11]	2.329	2.401	4.730	180.0	6.492			
				Second-order saddle points				
SP8($D_{\infty h}$)	4.868	2.434	2.434	0.0	-0.1683	898.6	585.9i	1409.5i
SP9(C_{2v})	3.798	2.513	2.513	40.9	-0.1820	1168.8i	477.4i	731.9

[a)] This work. Relative to the $O(^1D) + N(^4S) + N(^4S)$ asymptote.

[b)] This work. Fitted to DMBE-SEC of MRCI(Q)/VQZ poins.

[c)] This work. Enery is in ev defined relative to N_2O ground state X^1A' global minimum: $R_1 = 2.155\,a_0$, $R_2 = 2.255\,a_0$, $R_3 = 4.410\,a_0$ and $\theta_{ONN} = 180°$.

Table 3: QCT rate constants for the $N(^2D) + NO(X\,^2\Pi)$ at room temperature ($T \approx 300$ K).

Method	surface	$k/10^{-12}\,\mathrm{cm^3\,s^{-1}}$
QCT[a]	X^1A'	20.3±0.1
QCT[b]	$2^1A'$	7.2± 0.3
QCT[c]	X^1A'+$2^1A'$	27.5±0.2
Exp.[d]	...	70± 25,[17] 61±37[18]
		59±4.0,[19] 82.7±2.9[21]

[a] Previous work from Ref 24.
[b] This work.
[c] The sum of the rate constants for X^1A' and $2^1A'$ states.
[d] Experimental results for the total removal of $N(^2D)$ by NO.

Figure 1: Partial adiabatic correlation diagram for N_2O molecules (near 130°) in C_s symmetry. Data taken from Ref 6. The cutoff for singlet and triplet states is relative to the N_2O ($X^1\Sigma^+$, 0,0,0). The symbol B indicates a relative barrier in the dissociation pathway. The red line corresponds to present work for $2^1A'$ state of N_2O.

Figure 2: Potential energy curves in ground state and low-lying singlet excited states, and transition dipole moments between ground state and first singlet excited state. (a) potential as a function of intermolecular distance r_{O-N_2} at a fixed N_2 bond distance $R_{N_2} = 2.13\,a_0$ and Jacobi angle $\gamma = 0°$. (b) potential as a function of γ for $R_{N_2} = 2.13\,a_0$ and $r_{O-N_2} = 3.3\,a_0$. (c) transition dipole moments as a function of γ at $R_{N_2} = 2.13\,a_0$ and $r_{O-N_2} = 3.3\,a_0$.

Figure 3: Switching function used to model the single-sheeted N_2O DMBE PES. The black solid line and open circles shown in (a) correspond to the fit of the $h(R_1)$ switching form to the *ab initio* points calculated for $O + N_2$ configuration as a function of the N-N distance (R_1), while red solid line and closed circles are the fit of the $h'(R_1)$ to the calculated energy deference between two lowest $^1A'$ states. The black solid line and open circles shown in (b) correspond to the fit of the $h(R_3)$ switching form to the *ab initio* points calculated for $N + NO$ configuration as a function of the N-O distance (R_3), while red solid line and closed circles are the fit of the $h'(R_3)$ to the calculated energy deference between two lowest $^1A'$ states. Shown in (c) is a perspective view of the global switching function $f_1(\mathbf{R})$ for oxygen.

Figure 4: Potential energy curve for $N_2(X^1\Sigma_g^+)$ and $NO(X^2\Pi)$, and the differences between the fit and the *ab initio* points.

Figure 5: Contour plot for a C_{2v} insertion of the O atom into the N_2 fragment. Contours equally spaced by $0.01\,E_h$, starting at $-0.368\,E_h$. The vertical dashed line indicates the region corresponding to insert cuts of $R_{N_2} = 2.13\,a_0$.

Figure 6: Contour plot for a insertion of the N atom into the mass center of NO fragment. Contours equally spaced by $0.01\,E_h$, starting at $-0.346\,E_h$.

Figure 7: Contour plot for the O atom moving around N_2 diatom within the range $1.8 \leq R_{N_2}/a_0 \leq 2.5$, which lies along the X-axis with the center of the bond fixed at the origin. Contours are equally spaced by $0.005\,E_h$, starting at $-0.351\,E_h$. The dashed and dotted area are contours equally spaced by $-0.00015\,E_h$ starting at $-0.362\,E_h$.

Figure 8: Contour plot for the N atom moving around NO diatom within the range $1.9 \leq R_{NO}/a_0 \leq 2.6$, which lies along the X axis with the center of the bond fixed at the origin. Contours are equally spaced by $0.006\,E_h$, starting at $-0.35\,E_h$. The dashed and dotted lines are contours equally spaced by $-0.0002\,E_h$ starting at $-0.222\,E_h$.

Figure 9: Cuts of DMBE PES along the atom-diatom radial coordinates for fixed diatomic bond distance. Panels a, b and c refers to the $O - N_2$ channel for $\gamma = 0°$, $15°$, $30°$, $45°$, $60°$, $75°$ and $90°$, while c, d and e to N-NO for $\gamma = 0°$, $30°$, $60°$, $90°$, $120°$, $150°$ and $180°$. The fixed diatomic bond distance are as follows: (a) $R_{N_2} = 2.132\,a_0$; (b) R_{N_2}=2.5 a_0; (c) $R_{N_2} = 3.5\,a_0$; (d) $R_{NO} = 2.237\,a_0$; (e) $R_{NO} = 2.5\,a_0$; (f) $R_{NO} = 3.5\,a_0$. The open circles indicate the actually calculated MRCI/VQZ energies.

Figure 10: Relaxed triangular plot in hyperspherical coordinates illustrating the location and symmetry of all stationary points discussed in present work for $2^1A'$ state of N_2O.

Figure 1

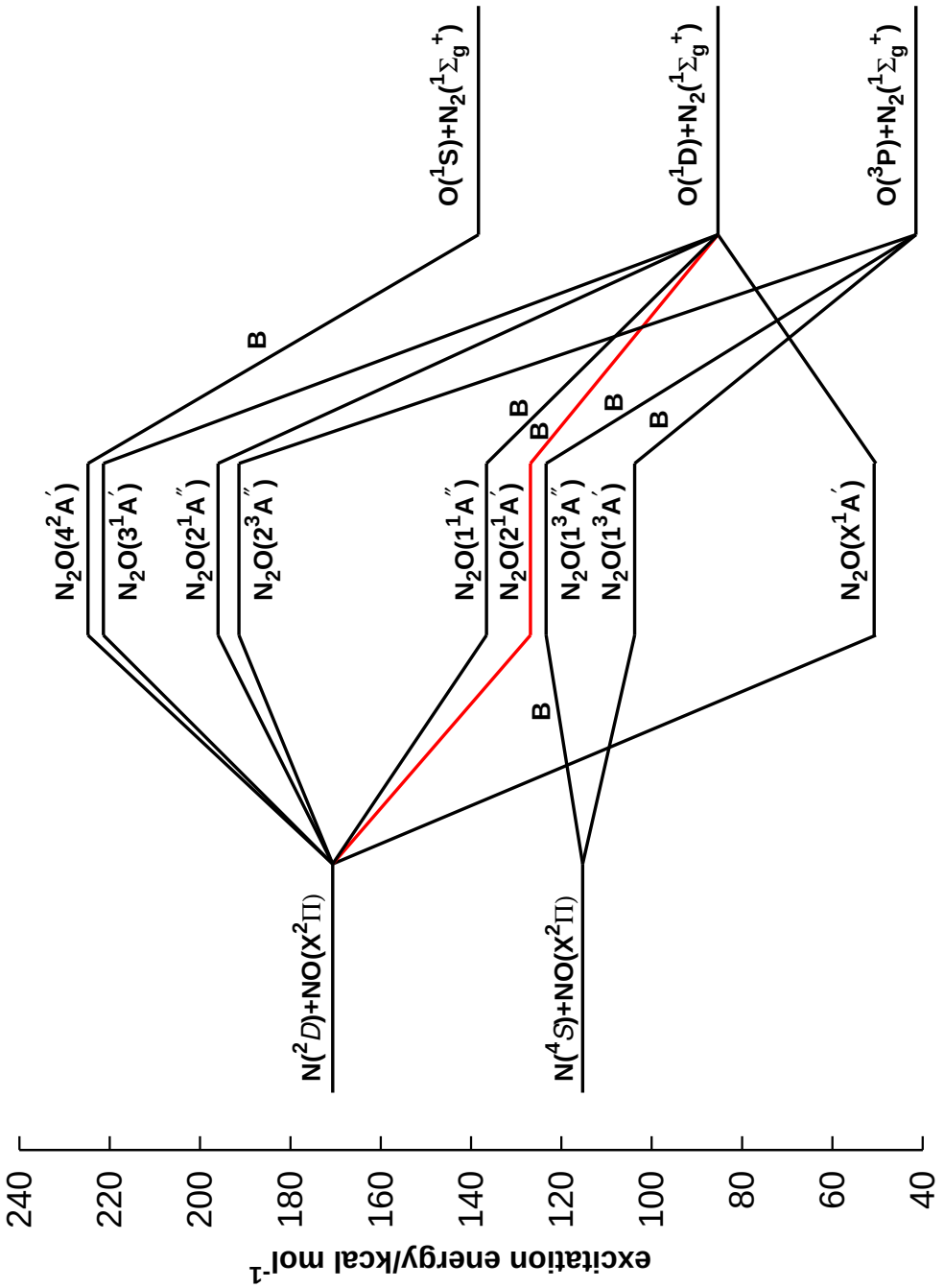
excitation energy/kcal mol-1
240
220
200
180
160
140
120
100
80
60
40
N(2D)+NO(X2Π)
N(4S)+NO(X2Π)
O(1S)+N2(1Σg+)
O(1D)+N2(1Σg+)
O(3P)+N2(1Σg+)
N2O(4 2A′)
N2O(3 1A′)
N2O(2 1A″)
N2O(2 3A″)
N2O(1 1A″)
N2O(2 1A′)
N2O(1 3A″)
N2O(1 3A′)
N2O(X 1A′)
B
B
B
B
B
B

Figure 2

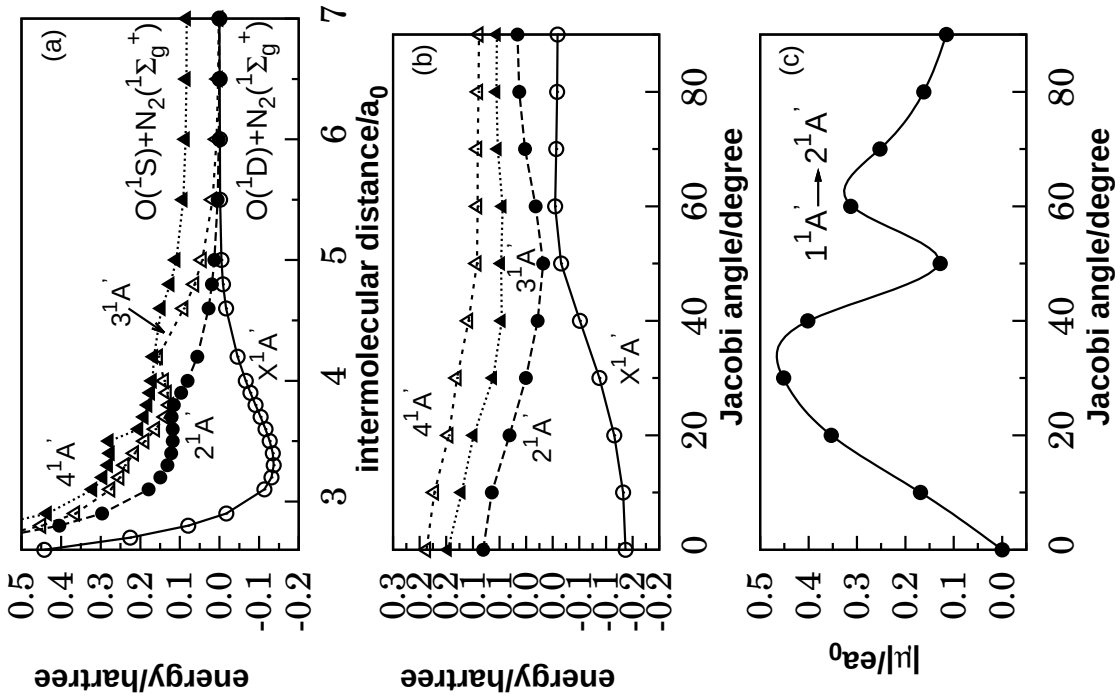
(a)
(b)
(c)
energy/hartree
intermolecular distance/a0
Jacobi angle/degree
|μ|/ea0
O(1S)+N2(1Σg+)
O(1D)+N2(1Σg+)
4 1A'
3 1A'
2 1A'
X 1A'
1 1A'→2 1A'

Figure 3

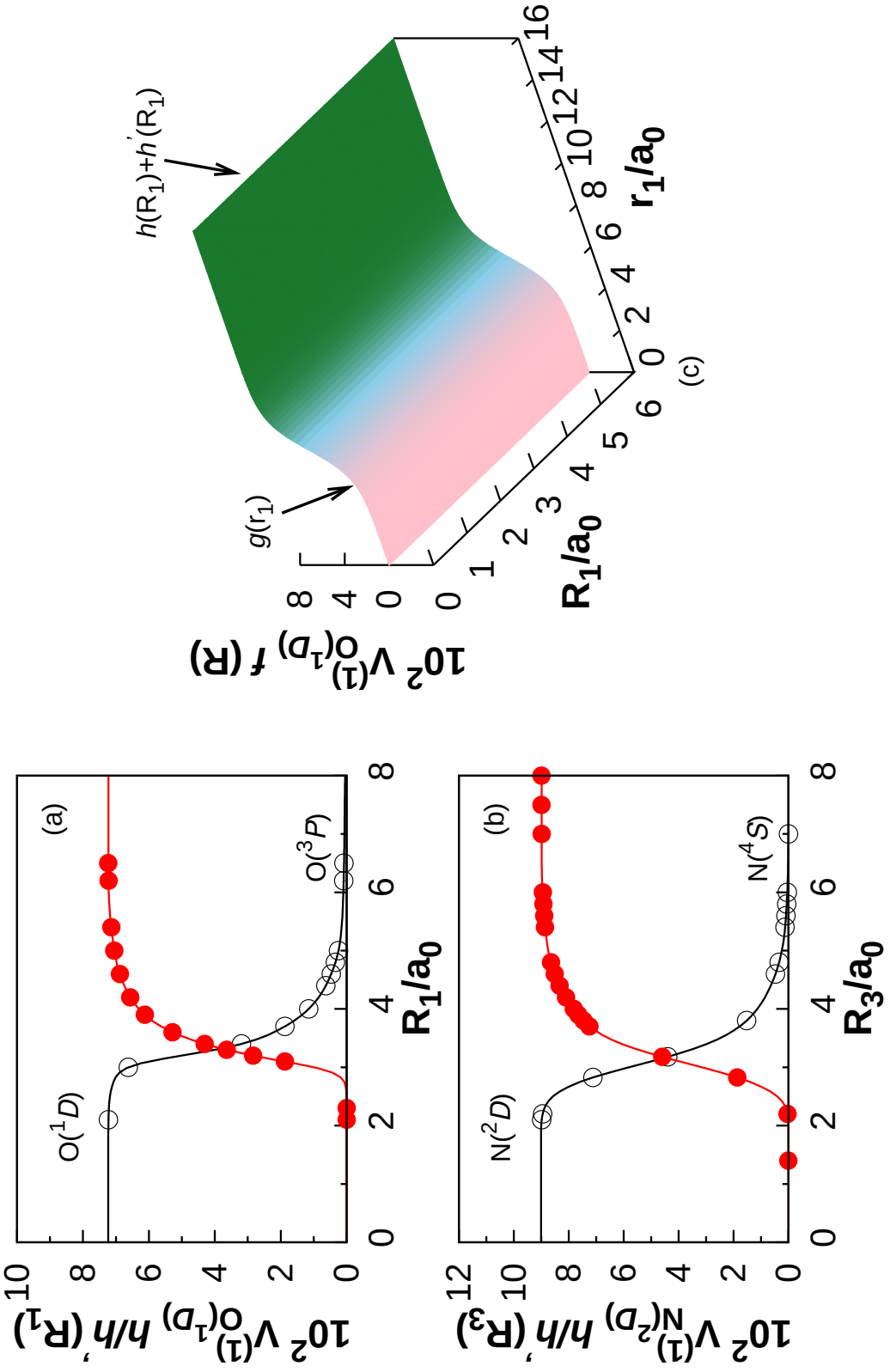

Figure 4

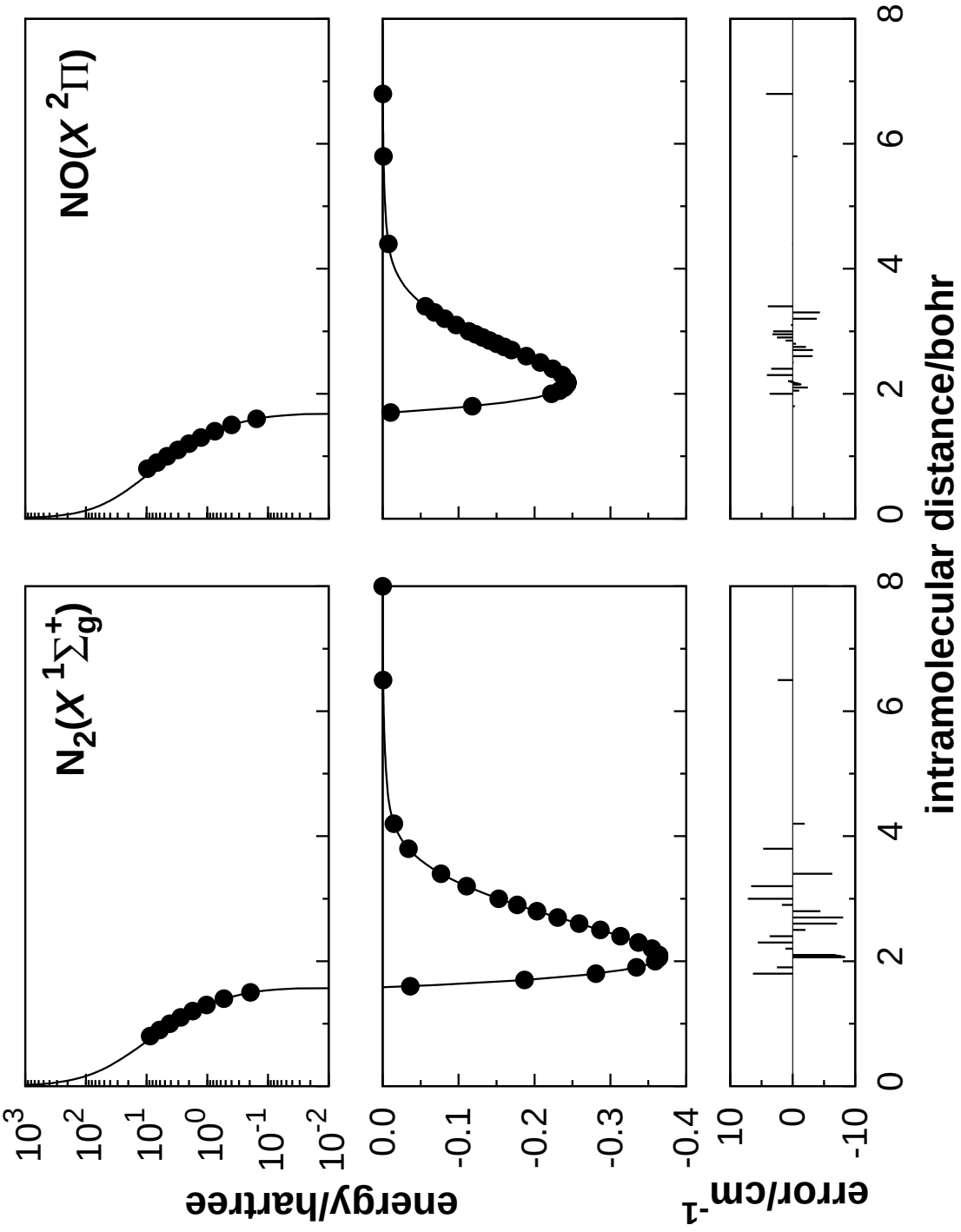
NO($X\ ^2\Pi$)
$N_2(X\ ^1\Sigma_g^+)$
energy/hartree
error/cm^{-1}
intramolecular distance/bohr

Figure 5

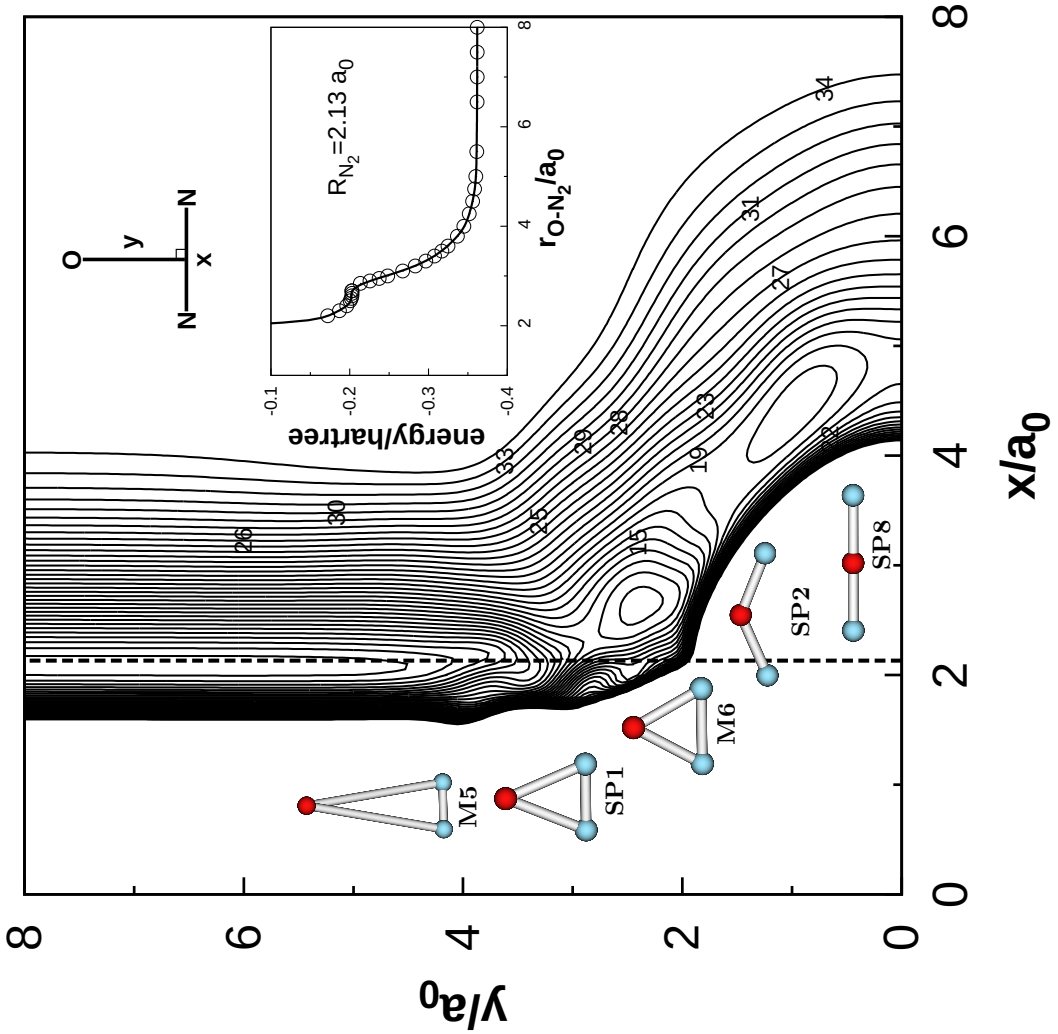
y/a0
x/a0
0
2
4
6
8
M5
SP1
M6
SP2
SP8
26
30
25
33
15
29
28
19
23
31
27
34
O
N
N
y
x
R_N2=2.13 a0
r_O-N2/a0
energy/hartree
-0.1
-0.2
-0.3
-0.4

Figure 6

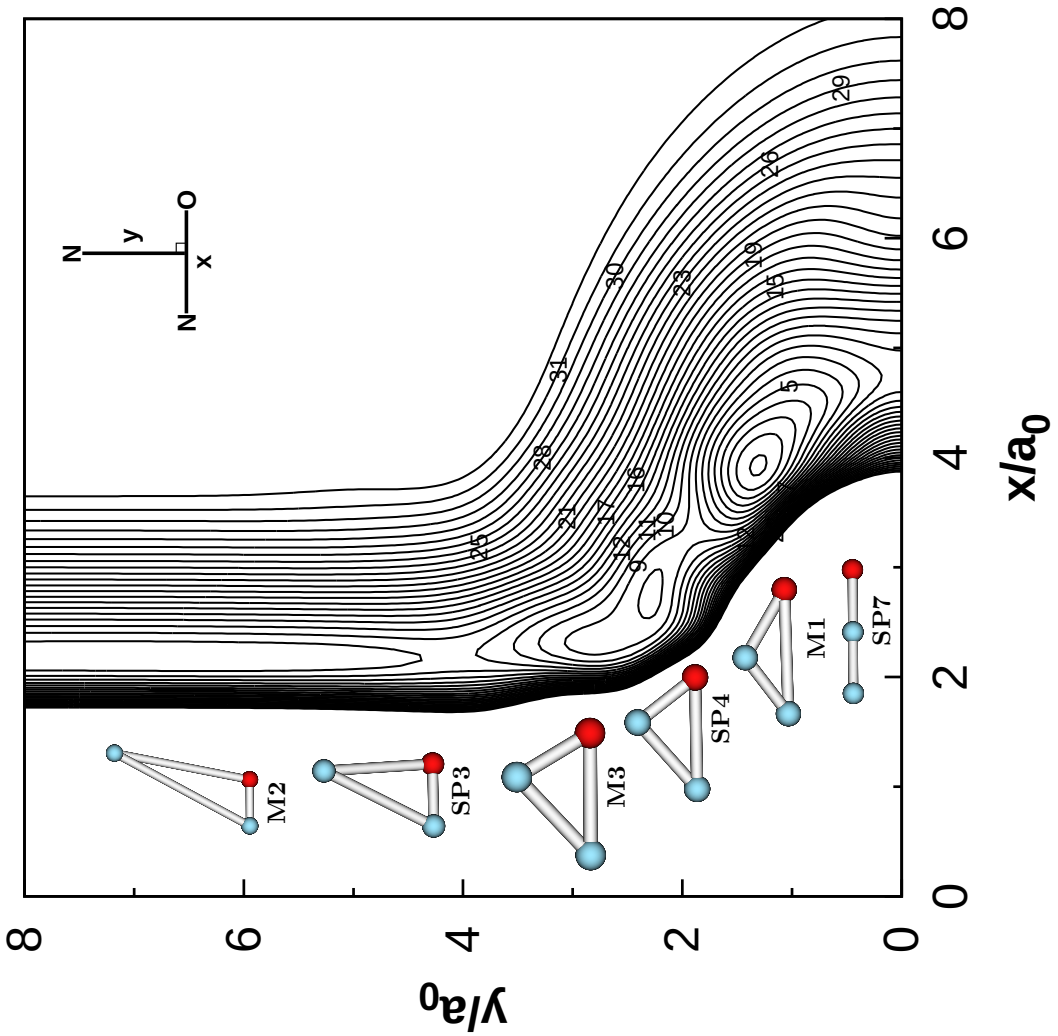
y/a0
x/a0
0
2
4
6
8
N
y
x
O
M2
SP3
M3
SP4
M1
SP7
5
9
10
11
12
16
17
21
25
28
31
30
23
19
15
26
29

Figure 7

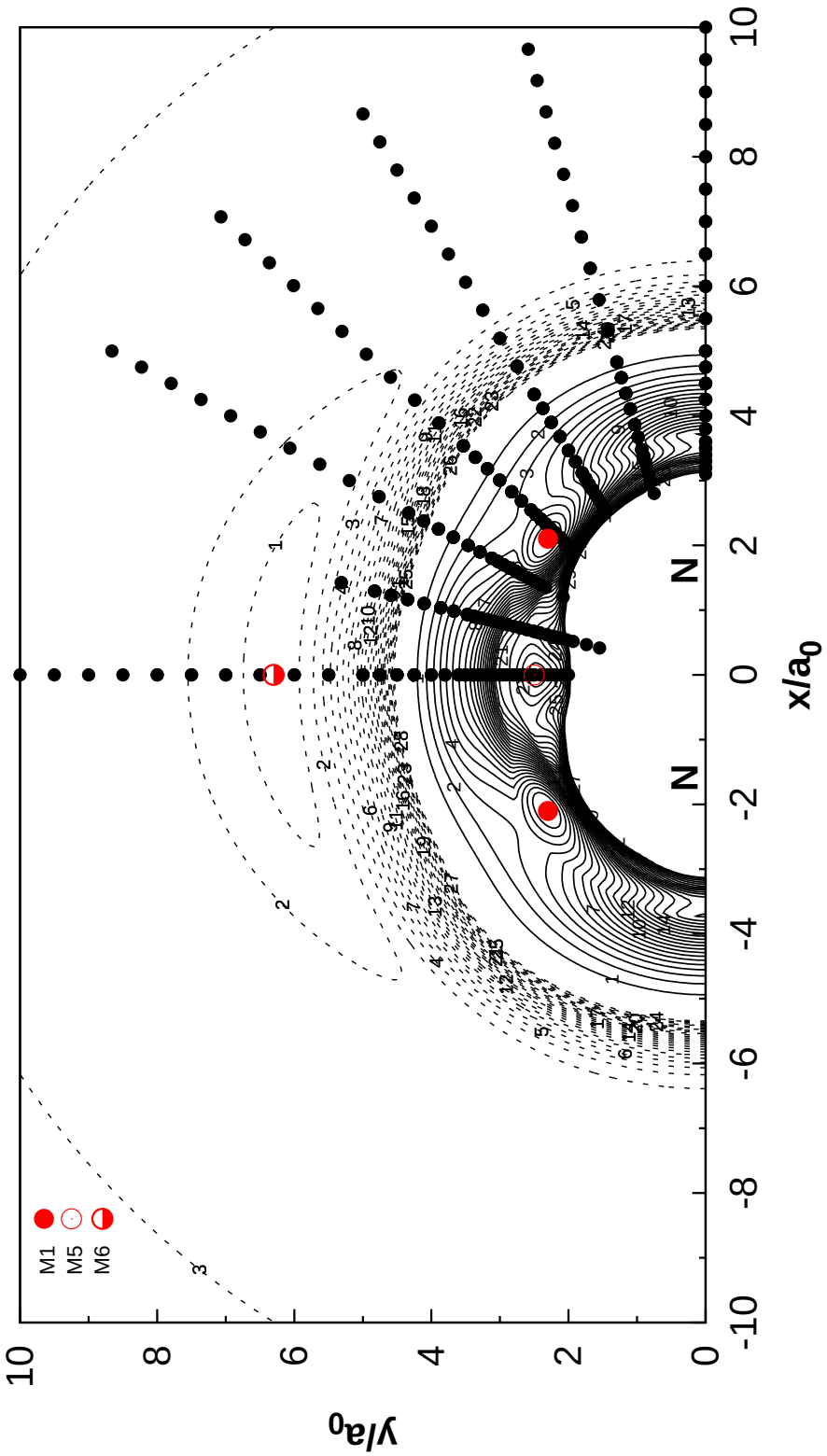

Figure 8

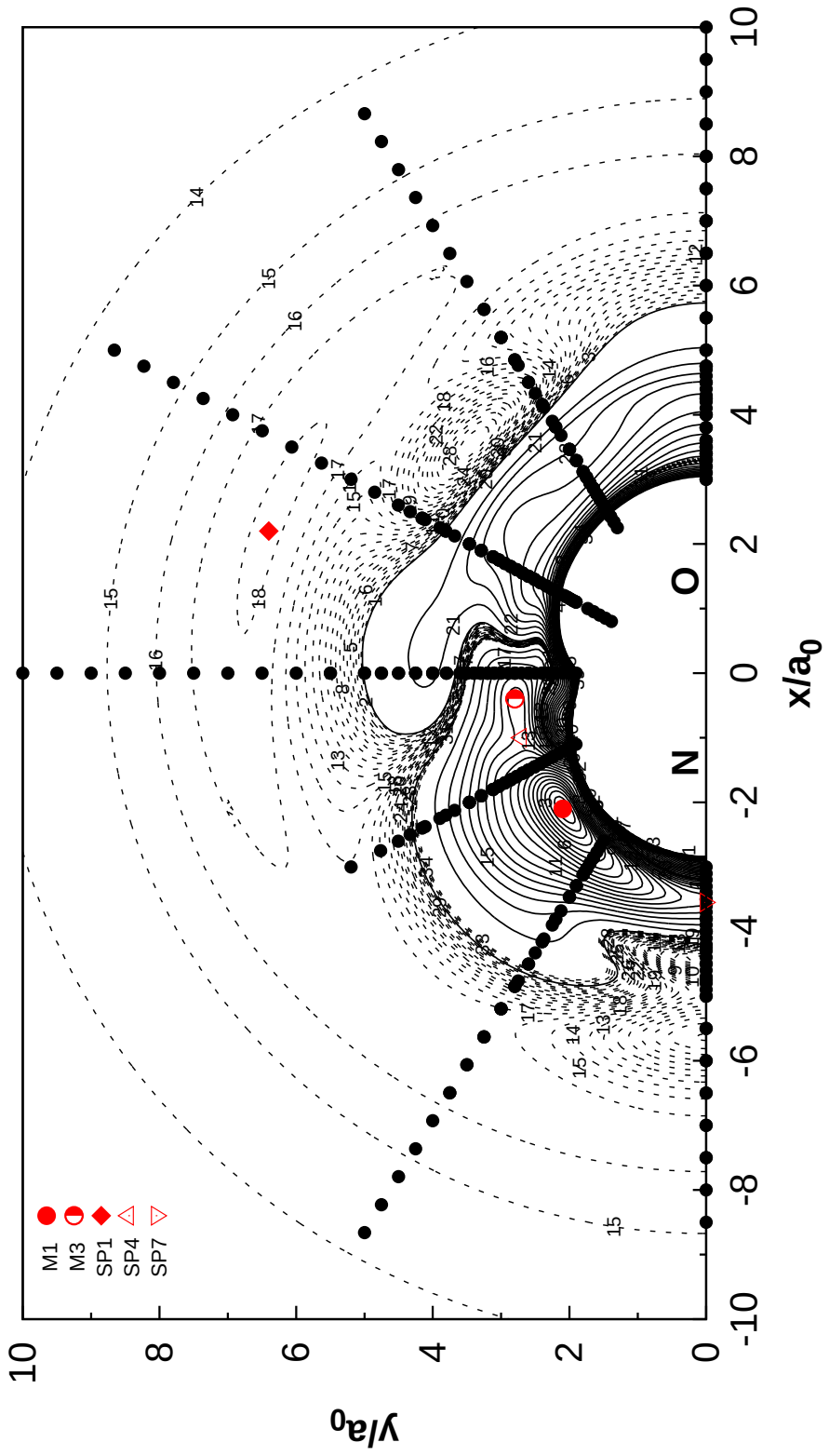

Figure 9

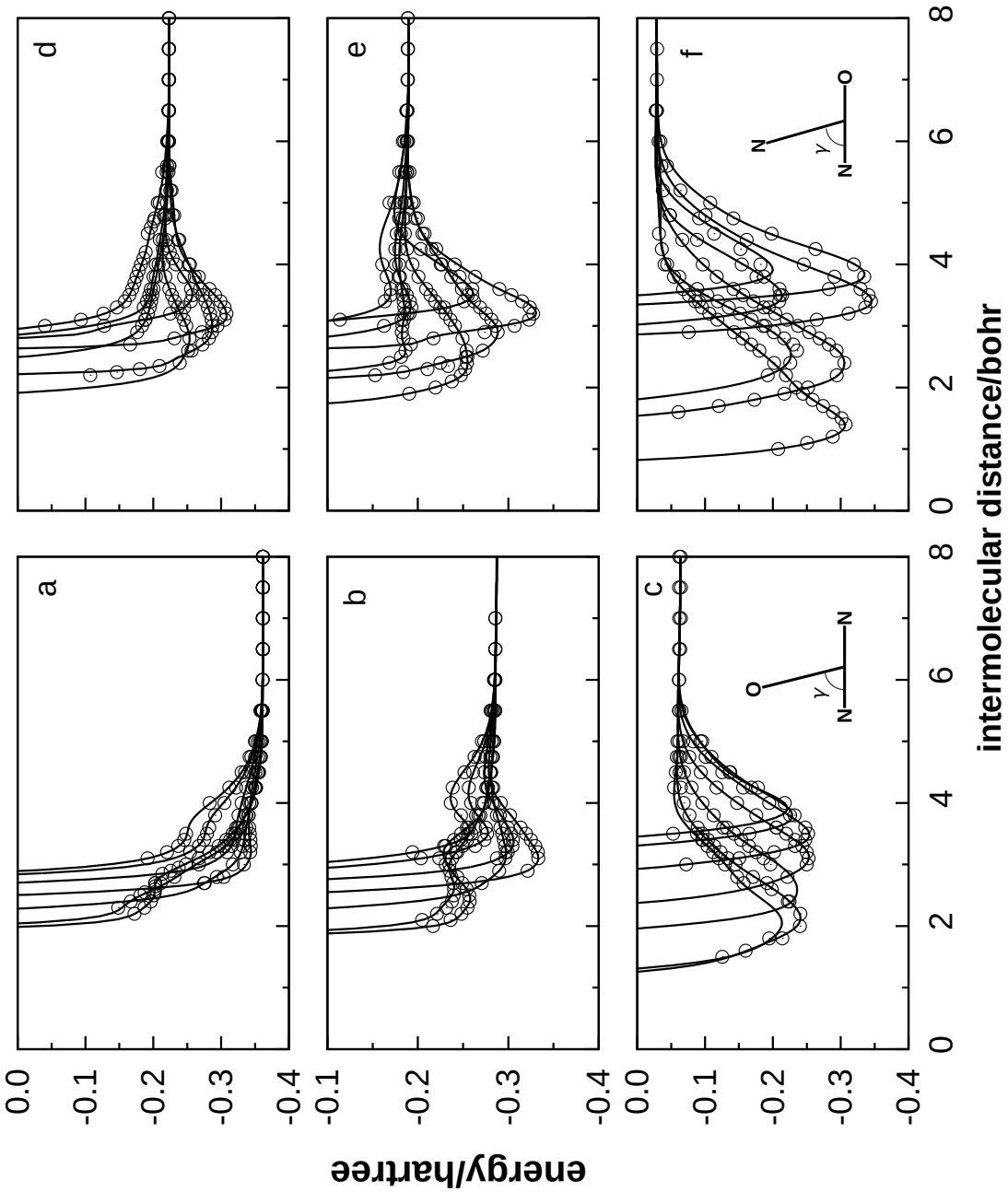
a
b
c
d
e
f
energy/hartree
intermolecular distance/bohr
0.0
-0.1
-0.2
-0.3
-0.4
0
2
4
6
8
N
O
γ

Figure 10

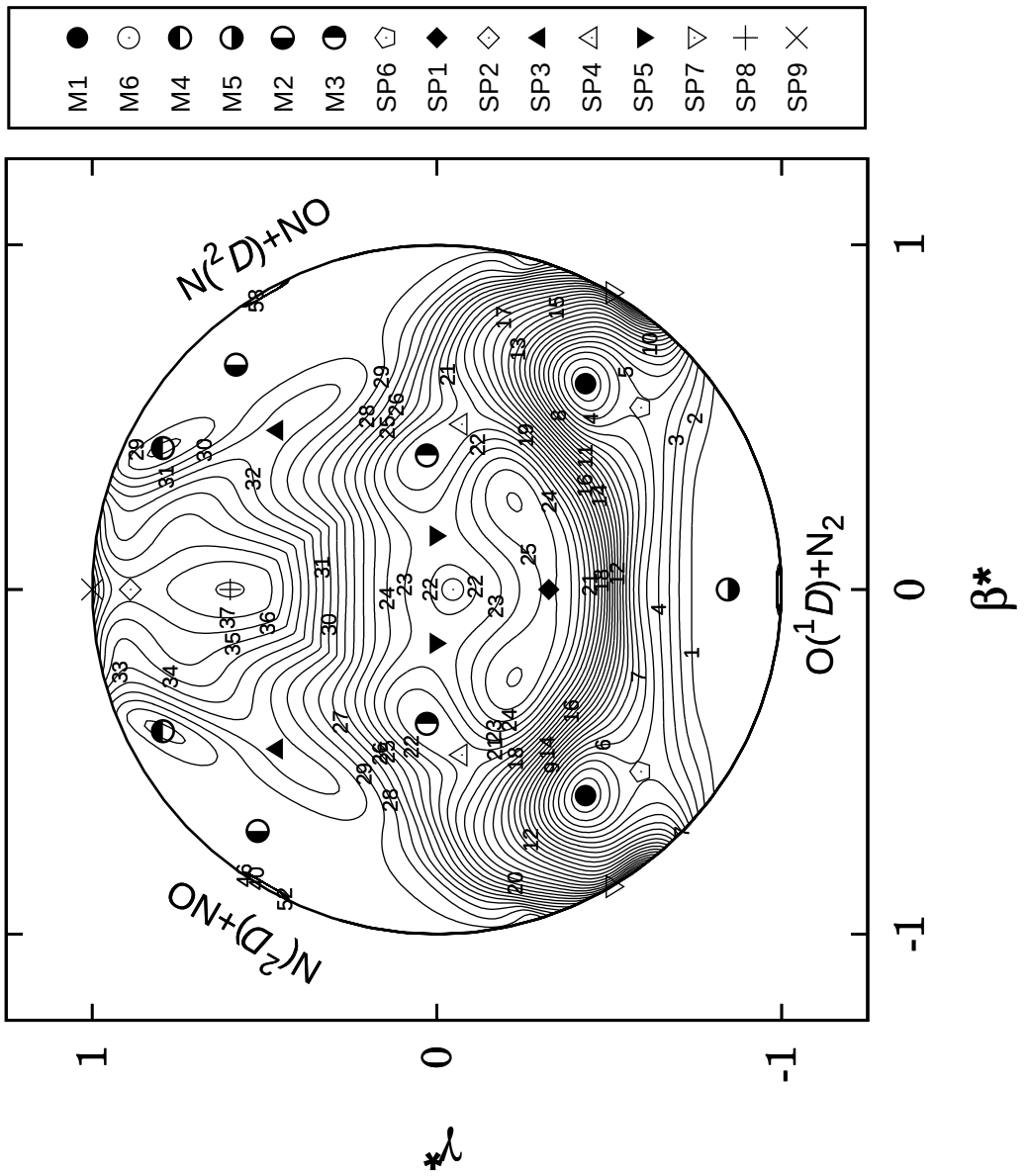
M1
M6
M4
M5
M2
M3
SP6
SP1
SP2
SP3
SP4
SP5
SP7
SP8
SP9
N(2D)+NO
ON+(2D)N
O(1D)+N2
γ*
β*
1
0
-1

(Submitted to *J. Chem. Phys.* SI)

Accurate Double Many-Body Expansion Potential Energy Surface for the $2^1A'$ state of N_2O

Jing Li and António J. C. Varandas*[1]
Departamento de Química, Universidade de Coimbra

3004-535 Coimbra, Portugal

[1]Corresponding author: varandas@uc.pt

Table 1: Parameters in switching functions.

Parameters	$h_1(\mathbf{R})$	$h_1'(\mathbf{R})$	Parameters	$h_{2,3}(\mathbf{R})$	$h_{2,3}'(\mathbf{R})$	Parameters	$g_{1,2,3}(\mathbf{r})$
α_1	0.632144	0.67073	α_1	0.627059	0.626781	α	0.75
α_2	0.685171	0.698921	α_2	0.355785	0.354896	$r^0_{1,2,3}$	5.5
β_1	1.59035	1.64403	β_1	0.521073	0.520105		
β_2	0.268852	0.289585	β_2	0.278026	0.276755		
R_1^{10}	1.65274	1.77341	$R_{2,3}^{10}$	2.63604	2.63622		
R_1^{11}	3.98608	3.96808	$R_{2,3}^{11}$	3.78884	3.78975		
R_1^{20}	2.8661	2.90613	$R_{2,3}^{20}$	0.70132	0.68949		
R_1^{21}	4.74015	4.69477	$R_{2,3}^{21}$	4.74172	4.74486		

Table 2: Parameters for two-body potential energy curves.

Parameter	$N_2(X^1\Sigma_g^+)$	$NO(X^2\Pi)$
R_e/a_0	2.078589	2.177509
$D/\mathrm{E_h}$	0.699842	0.478285
$\alpha_1/\mathrm{a_0^{-1}}$	1.29099	1.36879
$\alpha_2/\mathrm{a_0^{-2}}$	−1.13654	−1.0914
$\alpha_3/\mathrm{a_0^{-3}}$	0.897313	1.08947
$\alpha_4/\mathrm{a_0^{-3}}$	−0.514463	−0.74479
$\alpha_5/\mathrm{a_0^{-3}}$	0.113097	0.187319
$\gamma_0/\mathrm{a_0^{-1}}$	0.739658	0.817881
$\gamma_1/\mathrm{a_0^{-1}}$	12.1757	5.36031
$\gamma_2/\mathrm{a_0^{-1}}$	0.04123	0.106657
R_0/a_0	6.5780	6.1160
$C_6/\mathrm{E_h a_0^{-6}}$	24.10	18.78
$C_8/\mathrm{E_h a_0^{-8}}$	438.4155	305.3882
$C_{10}/\mathrm{E_h a_0^{-10}}$	10447.8275	6505.4914

Table 3: Numerical values (in atomic unit) of the parameters in Eq. (18).

	$C_6^0(R)$	$C_6^2(R)$	$C_8^0(R)$	$C_8^2(R)$	$C_8^4(R)$	$C_{10}^0(R)$
$O-N_2$						
R_M/a_0	3.5420	3.4783	3.5483	3.4879	3.4765	3.5522
D_M/E_h	44.363	5.7508	1684.5394	805.7889	63.0748	83794.8807
a_1/a_0^{-1}	1.19418998	−0.872172953	0.531898763	1.45365474	1.5986895	1.23751524
a_2/a_0^{-2}	0.204898558	0.238686556	−0.0004061	0.784568952	0.702606311	0.228397612
a_3/a_0^{-3}	0.00074840	0.00864448	−0.0223353	0.147548894	0.129022906	0.0016833
b_2/a_0^{-2}	0.435614640	0.512820625	0.334567520	0.871286483	0.512538430	0.491703448
b_3/a_0^{-3}	5.8×10^{-2}	3.1×10^{-9}	3.8×10^{-9}	3.7×10^{-9}	2.6×10^{-2}	7.3×10^{-2}
$N-NO$						
R_M/a_0	3.4000	3.3437	3.2932	3.3017	3.3074	4.2247
D_M/E_h	53.0984	7.4737	1827.0389	1176.5849	105.1093	192939.9868
a_1/a_0^{-1}	0.811851550	0.878344815	0.764321651	1.15666958	0.970437546	1.04109955
a_2/a_0^{-2}	−0.353046402	0.233889325	0.15085383	0.52621789	0.260198976	0.28356877
a_3/a_0^{-3}	−0.205365383	0.00098762	−0.01364140	0.02152999	−0.00166280	0.00010487
b_2/a_0^{-2}	0.359021660	0.585315550	0.557005836	1.16884594	0.08573123	0.16127091
b_3/a_0^{-3}	5.5×10^{-2}	2.3×10^{-9}	1.5×10^{-8}	1.5×10^{-8}	8.5×10^{-9}	9.5×10^{-3}

Table 4: Parameters and reference geometries of DMBE PES in the extended Hartree-Fock energy of Eq. (22).

Coefficients	$P^{(1)}$	$P^{(2)}$	$P^{(3)}$	$P^{(4)}$	$P^{(5)}$
$\gamma_1^{(j)}/\mathrm{a}_0^{-1}$	2.4	2.4	3.3	1.0	0.3
$\gamma_2^{(j)}/\mathrm{a}_0^{-1}$	-1.6	2.7	2.2	0.8	1.6
$\gamma_3^{(j)}/\mathrm{a}_0^{-1}$	2.7	-1.6	2.2	0.8	1.6
$R_1^{(j),\mathrm{ref}}/\mathrm{a}_0$	2.35	2.35	2.0	3.0	3.5
$R_2^{(j),\mathrm{ref}}/\mathrm{a}_0$	4.75	2.40	3.795	3.5	2.95
$R_3^{(j),\mathrm{ref}}/\mathrm{a}_0$	2.40	4.75	3.795	3.5	2.95

Table 5: Numerical values of DMBE PES in the extended Hartree-Fock energy of Eq.(22).

Coefficients	$P^{(1)}+P^{(2)}$	$P^{(3)}$	$P^{(4)}$	$P^{(5)}$
c_1/a_0^0	−0.0723579738	0.0872736198	−1.8266351948	3.4368794382
c_2/a_0^{-1}	−0.1709193163	0.0282545624	0.3322765868	3.7277483119
c_3/a_0^{-1}	−0.5150708167	0.1734470360	−1.5694380411	−4.9659022015
c_4/a_0^{-2}	0.1001382712	−0.2180998232	−0.4398031291	4.0647171725
c_5/a_0^{-2}	0.8600602743	−0.0557184503	−0.1020559564	2.1035006800
c_6/a_0^{-2}	0.7315906299	−0.4568543868	−1.1522597722	−6.4731480711
c_7/a_0^{-2}	0.2399978792	−0.0653072668	0.6273871462	−0.7051286284
c_8/a_0^{-3}	−0.5735174251	−1.4487071416	0.2034150621	2.8932130485
c_9/a_0^{-3}	−1.0993466512	0.8927674427	−0.8483440246	4.4993252408
c_{10}/a_0^{-3}	1.0189304495	0.7247717825	−0.1781212274	0.5223564834
c_{11}/a_0^{-3}	−0.8361518979	−1.4201801584	0.1236905376	−8.1550352273
c_{12}/a_0^{-3}	−0.8605622685	−1.1433489752	0.2825137763	−1.2422171192
c_{13}/a_0^{-3}	−1.7966744520	2.4870856020	0.0716021837	−1.7590937481
c_{14}/a_0^{-4}	0.2196863748	0.0853084620	−0.0432895509	1.3496929999
c_{15}/a_0^{-4}	1.6094643818	8.6388242554	0.1790859008	2.0751676859
c_{16}/a_0^{-4}	1.1520790616	0.3658006873	0.0622275888	−0.1694841007
c_{17}/a_0^{-4}	0.0255908343	2.4878353913	−0.0069211813	−0.6642084685
c_{18}/a_0^{-4}	0.3748053362	6.6536171456	−0.1551889741	−4.7107817323
c_{19}/a_0^{-4}	1.4164893844	−8.0915556561	0.1800247417	−3.3264624921
c_{20}/a_0^{-4}	0.4942850061	11.5192670563	−0.3554476409	−1.3329404084
c_{21}/a_0^{-4}	−1.3384085109	0.1518311855	−0.0693831584	−0.2075729713

Table 6: Numerical values of DMBE PES in the extended Hartree-Fock energy of Eq.(22).

Coefficients	$P^{(1)}+P^{(2)}$	$P^{(3)}$	$P^{(4)}$	$P^{(5)}$
c_{22}/a_0^{-4}	−0.3896922361	−1.2471375361	−0.1093699600	−0.6347573438
c_{23}/a_0^{-5}	−0.1858271272	2.0000619961	0.0018084154	0.6281009644
c_{24}/a_0^{-5}	−2.5530152953	6.9076094181	−0.0552333358	1.2648099733
c_{25}/a_0^{-5}	0.3997108580	−3.0877939839	0.0110747922	0.0029486170
c_{26}/a_0^{-5}	−4.1135919568	−3.1641307220	0.0216292178	−1.2159553471
c_{27}/a_0^{-5}	4.2282830121	−0.3022750435	0.0338138840	−0.0730566552
c_{28}/a_0^{-5}	−1.0756980061	9.2474675438	0.2011117604	−2.5084663910
c_{29}/a_0^{-5}	1.4639381654	−3.4700812724	−0.1776952736	−2.2108270664
c_{30}/a_0^{-5}	0.0091731009	0.5112948889	−0.0728630459	−0.4312164567
c_{31}/a_0^{-5}	−6.3667272881	−3.5952853241	0.0382237349	1.2629056851
c_{32}/a_0^{-5}	−6.6036710623	1.7606872069	0.0425556419	1.1263590392
c_{33}/a_0^{-5}	−1.5520366283	−0.5555739326	0.0924175883	0.1685898173
c_{34}/a_0^{-5}	2.4234741721	−0.0930261758	0.0285841527	0.1318520198
c_{35}/a_0^{-6}	0.0423169655	1.4459716612	0.0253438670	0.1261439459
c_{36}/a_0^{-6}	2.4883406582	3.9311509580	−0.0033095788	0.2983399214
c_{37}/a_0^{-6}	−0.8280182030	2.3328307291	−0.0392755000	0.2019287880
c_{38}/a_0^{-6}	3.0194239982	−1.1786583419	−0.0268354516	−0.6261632454
c_{39}/a_0^{-6}	1.5388489842	2.2623929068	0.0066931717	0.2388391268
c_{40}/a_0^{-6}	2.5295453432	0.5463542030	0.0178800352	−0.1341726757
c_{41}/a_0^{-6}	1.1551095851	0.1207909330	0.0036433440	0.0791033702
c_{42}/a_0^{-6}	0.3446748590	5.2280908938	−0.0152194446	−0.6008532349
c_{43}/a_0^{-6}	0.1204357675	−1.5116782318	0.0670531856	−0.8422346405
c_{44}/a_0^{-6}	1.2915752450	3.4105889366	−0.0686472474	−0.2933556063
c_{45}/a_0^{-6}	1.5486770323	−0.2083423908	−0.0015029785	0.8245889157
c_{46}/a_0^{-6}	0.5046012142	−2.8735613915	0.0060639770	0.8700192104
c_{47}/a_0^{-6}	−4.7589877249	4.2305766719	0.0149242952	0.2150179786
c_{48}/a_0^{-6}	−1.7027644138	−0.8318540895	−0.0226445837	0.4027893494
c_{49}/a_0^{-6}	0.1932134151	0.7362791823	0.0063466250	−0.1572530501
c_{50}/a_0^{-6}	4.7087244227	−0.6912265529	−0.0064441566	−0.2306992517

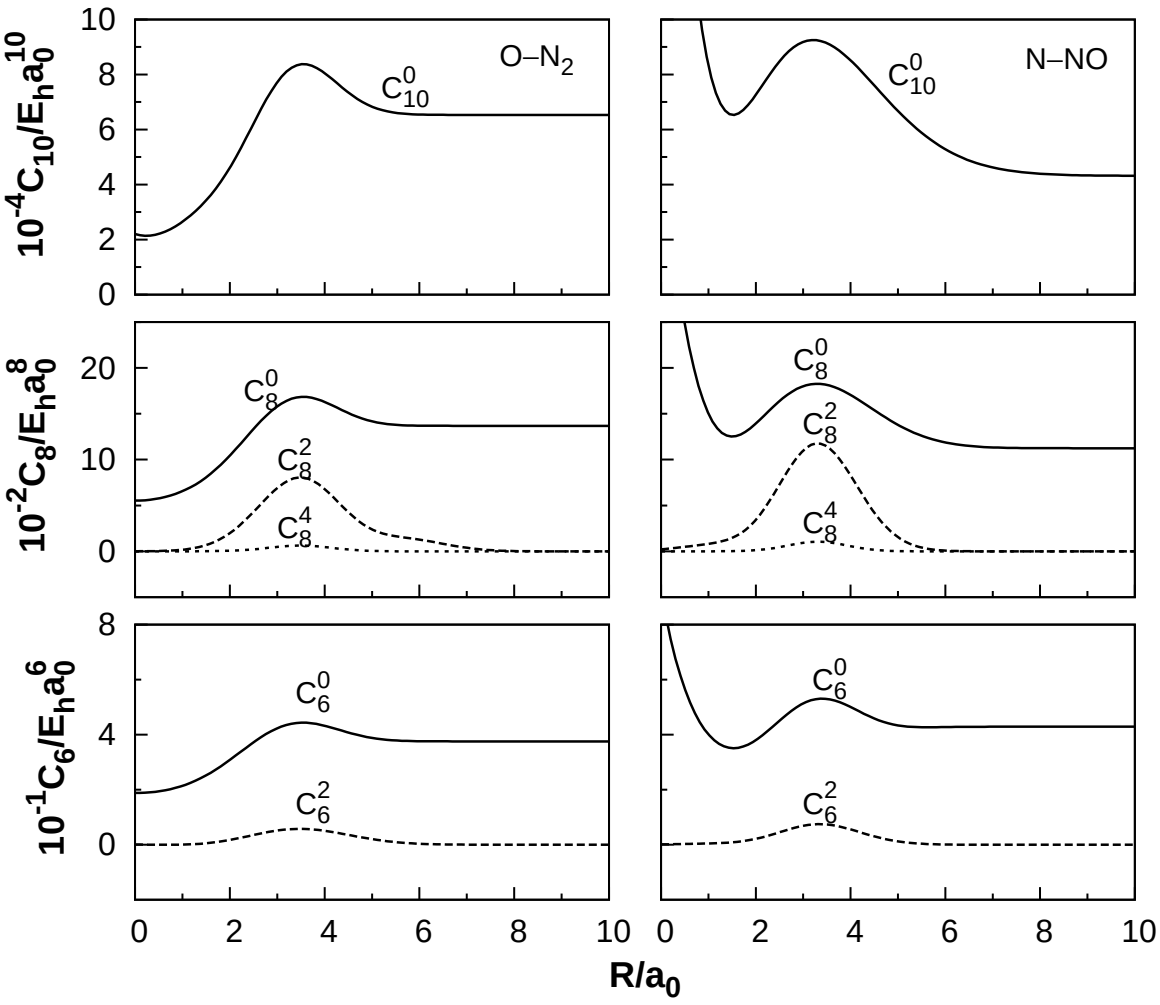

Figure 1: Dispersion coefficients for the atom-diatom asymptotic channels of N_2O as a function of this corresponding internuclear distance of diatom.

Part III

Conclusions

Conclusions

In the present thesis we reported a series of published results, mainly focused on the *ab initio* calculation and modelling of double many-body expansion potential energy surfaces for nitrous oxide molecular systems. A global single-sheeted DMBE PES has been reported for the ground state of N_2O, on the basis of a least-squares fit to a set of high level AV*T*Z *ab initio* energies, which have been suitably corrected using the DMBE-SEC method. The various topographical features of the novel PES have been carefully examined and compared with the previous PES, as well as with experimental results available in the literature. Based on these features, it is concluded that the DMBE PES reported here is globally valid and accurately fits our *ab initio* points.

Using a DMBE PES for the ground state of N_2O that we have recently proposed, we have carried out a QCT study of the rate constant for the $N(^2D) + NO(X\,^2\Pi)$ reaction, with the prediction that only a relatively small variation is expected over a wide temperature range $(50 - 3000K)$. The analysis for reaction probabilities shows most of the trajectories pass only through the NNO minimum, at higher temperature there is a significant argument of the other 2 reaction routes. It is well stated that our DMBE PESs accurately describe the NNO C_s region and the the NON C_{2v} and C_s region, which make them valuable for use in theoretical studies of all three reaction processes. We have reported cross sections as a function of the translation energy, which depicted the following behaviour: the cross section increases with decreasing translation energy at low collision energies while for higher ones σ becomes essentially constant or just slightly increases with E_{tr}. Extensive comparisons with previous experimental and theoretical predictions have also been performed, with the results showing a higher reactivity than others available in

the literature. An improved agreement with the experimental results has therefore been obtained, even though there are large experimental uncertainties.

To map the PES of the first singlet excited state of N_2O, we have calculated a wealth of accurate MRCI energies based on accurate MRCI/VQZ energies, which have been suitably corrected using the DMBE-SEC method. The global DMBE PES so obtained is expected to show good behaviour over the entire configuration space. The various topographical features of the novel PES have been carefully examined and compared with previous forms, as well as with experimental data available in the literature. Based on such features, it is concluded that the DMBE PES here reported is globally valid while accurately fitting the *ab initio* points used for its calibration. Several minima and transition states have been characterized on the $2^1A'$ state of N_2O. The novel DMBE PES has used for exploratory quasiclassical trajectory calculations of the thermal rate constant at room temperature. A comparison with other available potential energy surfaces as well as experimental data is also provided. They show good agreement both with previous high quality theoretical studies and experimental data.

The PESs reported in the present thesis provides an excellent start towards an understanding of the electronic structure, potential scheme and reactivity of the nitrous oxide system. They can be further used to study other reactive processes. Finally, they may enable the construction of larger polyatomic DMBE PES in which N_2O is contained, such as N_3O and N_2O_2.

Appendix

Linear least-squares

Linear least-squares [1, 2] is one of the most commonly used methods in numerical computation, which is to fit a set of data points $(\mathbf{x}_i, y_i)$ to a linear combination of any M specified functions of $\mathbf{x}$

$$y(\mathbf{x}) = \sum_{k=1}^{M} a_k X_k(\mathbf{x}) \tag{49}$$

where $X_1(\mathbf{x}), \ldots, X_M(\mathbf{x})$ are arbitrary fixed functions of $\mathbf{x}$, called the basis functions. A set of best-fit parameters correspond to a minimum of the merit function

$$\chi^2 = \sum_{i=1}^{N} \left[\frac{y_i - \sum_{k=1}^{M} a_k X_k(\mathbf{x}_i)}{\sigma_i} \right]^2 \tag{50}$$

where σ_i is the measurement error (standard deviation) of the ith data point,

The minimum of (50) occurs when the derivative of χ^2 with respect to all the M parameters a_k vanishes, *i.e.*

$$0 = \sum_{i=1}^{N} \frac{1}{\sigma_i^2} \left[y_i - \sum_{j=1}^{M} a_j X_j(\mathbf{x}_i) \right] X_k(\mathbf{x}_i) \qquad k = 1, \ldots, M \tag{51}$$

Interchanging the order of summations, we can write (51) as the matrix equation

$$\mathbf{\Lambda} \cdot \mathbf{a} = \boldsymbol{\beta} \tag{52}$$

where

$$\Lambda_{kj} = \sum_{i=1}^{N} \frac{X_j(\mathbf{x}_i) X_k(\mathbf{x}_i)}{\sigma_i^2}, \qquad \beta_k = \sum_{i=1}^{N} \frac{y_i X_k(\mathbf{x}_i)}{\sigma_i^2} \tag{53}$$

and $\mathbf{a}$ is the column vector of the adjustable parameters.

(51) and (52) are called the *normal equations* of the least squares problem. Their solutions can be obtained by using the Gauss-Jordan elimination method, which consists in looking for the column vector $\mathbf{a}$ by applying row operations on the augmented matrix $\mathbf{\Lambda}|\mathbf{c}$ to transform the matrix $\mathbf{\Lambda}$ into diagonal form.

A more general procedure to minimize (49), preventing no solution of (52) due to singularity in $\mathbf{\Lambda}$, is to use the *singular value decomposition* (SVD) technique. Such a method is based on a theorem which states that any $N \times M$ matrix $\mathbf{A}$, no matter how singular the matrix is, can be factorized in the form

$$\mathbf{A} = \mathbf{U} \cdot \mathbf{W} \cdot \mathbf{V}^T \tag{54}$$

where $\mathbf{U}$ is an $N \times M$ orthogonal matrix, $\mathbf{W}$ is a $M \times M$ diagonal matrix with positive or zero elements (the *singular values* of $\mathbf{A}$) and $\mathbf{V}^T$ is the transpose of the $M \times M$ orthogonal matrix $\mathbf{V}$.

Defining the following matrix and column vector

$$A_{ij} = \frac{X_j\left(\mathbf{x}_i\right)}{\sigma_i} \qquad \text{and} \qquad \mathbf{b}_i = \frac{y_i}{\sigma_i} \tag{55}$$

(49) can be written as

$$\chi^2 = |\mathbf{A} \cdot \mathbf{a} - \mathbf{b}|^2 \tag{56}$$

Then, the solution of the least-squares problem in (56) can be written as

$$\mathbf{a} = \sum_{i=1}^{M} \left(\frac{\mathbf{U}_{(i)} \cdot b}{\omega_i} \right) \mathbf{V}_{(i)} \tag{57}$$

with the variance in the estimate of a parameter a_j is given by

$$\sigma_j^2(a_j) = \sum_{i=1}^{M} \left(\frac{V_{ji}}{\omega_i} \right)^2 \tag{58}$$

Bibliography

[1] W. H. Press, S. A. Teukolsky, W. T. Vetterling, and B. P. Flannery, *Numerical Recipes in Fortran: the Art of Scientific Computing* (Cambridge University Press, New York, 1992).

[2] R. A. Horn, and Ch. R. Johnson, *Matrix Analysis* (Cambridge University Press, Cambridge, 1999)

Gamma Function

The **Gamma function** is defined* by the integral

$$\Gamma(z) \equiv \int_0^\infty t^{z-1} e^{-t} dt \tag{59}$$

When the argument z is an integer, the Gamma function can be written in the form of a factorial function:

$$\Gamma(n+1) = n! \tag{60}$$

Gamma function satisfies recurrence relation:

$$\Gamma(z+1) = z\Gamma(z) \tag{61}$$

The natural logarithm of the Gamma function is implemented in the *gammln* function from Numerical recipes.

The **Incomplete Gamma Function**is defined by:

$$P(a,x) \equiv \frac{\gamma(a,x)}{\Gamma(a)} \equiv \frac{1}{\Gamma(a)} \int_0^x t^{a-1} e^{-t} dt, \ (a>0) \tag{62}$$

It has the limiting values

$$P(a,0) = 0 \quad \text{and} \quad P(a,\infty) = 1 \tag{63}$$

The complement $Q(a,x)$ is:

$$Q(a,x) \equiv 1 - P(a,x) \equiv \frac{1}{\Gamma(a)} \int_x^\infty t^{a-1} e^{-t} dt, \ (a>0) \tag{64}$$

Functions *gammp* and *gammq* from Numerical recipes provides P and Q functions respectively.

*All definitions and properties from "Numerical Recipes in Fortran '77"